



Michael C. Gruber, Dipl.-Ing.

Hydrodynamics, Mass Transfer and Chemical Reactions in Bubble Columns

DOCTORAL THESIS

to achieve the university degree of

„Doktor der technischen Wissenschaften“

submitted to

Graz University of Technology

Supervisor

Univ.-Prof. Dipl.-Ing. Dr.techn. Johannes G. Khinast

Institute for Process and Particle Engineering

and Research Center Pharmaceutical Engineering GmbH

Graz, March 2015

Michael C. Gruber

Hydrodynamics, Mass Transfer and Chemical Reactions in Bubble Columns

Doctoral thesis

First Assessor and Supervisor

Univ.-Prof. Dipl.-Ing. Dr.techn. Johannes G. Khinast

Institute for Process and Particle Engineering

and Research Center Pharmaceutical Engineering GmbH

Graz University of Technology

Second Assessor

Univ.-Prof. Dipl.-Ing. Dr.techn. Matthäus Siebenhofer

Institute of Chemical Engineering and Environmental Technology

Graz University of Technology

Copyright© 2015 by Michael C. Gruber

All rights reserved. No part of the material protected by this copyright notice may be reproduced or utilized in any form or by any means, electronically or mechanically, including photocopying, recording or by any information storage and retrieval system with written permission from the author.

AFFIDAVIT

I declare that I have authored this thesis independently, that I have not used other than the declared sources/resources, and that I have explicitly indicated all material which has been quoted either literally or by content from the sources used. The text document uploaded to TUGRAZonline is identical to the present doctoral thesis.

Pace and Date

Signature

EIDESSTATTLICHE ERKLÄRUNG

Ich erkläre an Eides statt, dass ich die vorliegende Arbeit selbstständig verfasst, andere als die angegebenen Quellen/Hilfsmittel nicht benutzt, und die den benutzten Quellen wörtlich und inhaltlich entnommenen Stellen als solche kenntlich gemacht habe. Das in TUGRAZonline hochgeladene Textdokument ist mit der vorliegenden Dissertation identisch.

Ort und Datum

Unterschrift

For Sylvie

*“Double, double toil and trouble;
Fire burn, and cauldron bubble.”*

– William Shakespeare (1564-1616)

Contents

Abstract	viii
Kurzfassung	x
Acknowledgements	xii
1 Introduction	1
1.1 Multiphase Flow Theory	1
1.2 Bubble Column Reactors	3
1.3 Gas-Liquid Two-Phase Flows	6
1.4 Computational Methods for Multiphase Flows	9
1.5 Objective and Outline	15
Notation	16
References	17
2 Bubble Breakage and Coalescence in Euler-Lagrange Simulations	19
2.1 Introduction	20
2.2 Modeling	23
2.3 Results and Discussion	35
2.4 Summary and Conclusions	43
Notation	44
References	46
3 Impact of Bubble Breakage and Coalescence on Absorption and Chemisorption	49
3.1 Introduction	50
3.2 Modeling	54
3.3 Results and Discussion	65
3.4 Summary and Conclusions	83
3.5 Appendix	85
Notation	88
References	90

4	Euler-Lagrange Modeling of Gas-Liquid-Solid Flows	93
4.1	Introduction	94
4.2	Modeling	98
4.3	Results and Discussion	107
4.4	Summary and Conclusions	116
	Notation	118
	References	120
5	Conclusions and Outlook	123
5.1	Summary and Conclusions	123
5.2	Outlook	126
	References	128
	List of Publications	129
	About the Author	130

Abstract

Bubble columns (BCs) are simple constructed and economically operated apparatus that are utilized in manifold industrial processes. This reactor type is used to bring a gas and a liquid or suspension into contact, in which generally interphase mass transfers with subsequently proceeding chemical reactions take place. Due to their great importance for chemical, pharmaceutical, biochemical and petrochemical industries, engineers have always sought to increase the performance of BCs, whereat in recent decades computational fluid dynamics (CFD) has been increasingly utilized for this purpose. Although, many literature studies respective (slurry) BCs have been published, unresolved issues are still left. Latter can be explained by the complexity of the interrelations of the phenomena, which take place during the operation time of BCs. Additionally, the phenomena spread over several magnitudes in both, length as well as time scale.

In the course of this doctoral thesis, a CFD algorithm is developed for the numerical modeling of three-dimensional (slurry) bubble columns reactors, which are operated at the homogeneous or heterogeneous flow regime. Thereby, the algorithm is based on the open-source software package OpenFOAM® and pursues a four-way coupled event-driven Euler-Lagrange (EL) approach. The EL approach is chosen, because it is well suited to examine interactions of the dispersed phases, e.g. bubble-bubble interactions in bubble swarms, and their impact on other process parameters. In order to accelerate the handling of swarms, algorithm-based speed-up techniques are developed, which are described in detail within this thesis.

The first part of this thesis deals with the impact of bubble break-up and coalescence (B&C), caused by turbulent flow in a square cross-sectioned labor-scale BC, on the hydrodynamics, on the mass transfer and on the temporal development of chemical reactions. A comparison of the results for two-phase gas-liquid flows, which are obtained with both monodisperse and polydisperse bubble swarms, reveals that B&C has an impact on the mass transfer and on the progression of chemical reactions, while the liquid hydrodynamics remains nearly unaffected.

The second part of this thesis focuses on the modeling of three-phase gas-liquid-solid flows, wherefore an EL approach is utilized as simulation technique. A labor-scale cylindrical BC is used as setup for this basic research, which contains a solid hold-up of *1.6 vol-%* of neutrally

buoyant solid particles. In doing so, the emphasis is put on the verification of several models, which describe the interactions between the gaseous and the solid phase. The results indicate a vertical transport of solid particles and a significant impact on the local gas hold-up distribution, due to the effect of the particles on the suspension's viscosity. While the drag force modification model leads to uniform solid hold-ups and lower bubble velocities, the elastic collision model and the multistage collision model reveal similar flow predictions.

Kurzfassung

Blasensäulenreaktoren (BSR) sind einfach konstruierte und ökonomisch betreibbare verfahrenstechnische Apparaturen. Sie finden in einer Vielzahl von industriellen Prozessen ihre Anwendung, bei denen es gilt einen Phasenkontakt zwischen einem Gas und einer Flüssigkeit oder Suspension herzustellen, damit Stoffübertragungen oder chemische Reaktionen vonstattengehen. Während des Betriebes eines mit Flüssigkeit gefüllten BSR wird in dessen unterem Bereich ein Gas dispergiert, welches anschließend in der Flüssigkeit in Form von Gasblasen aufsteigt und dabei eine zirkulierende turbulente Strömung induziert, bis es im oberen Bereich des BSR aus der Flüssigkeit austritt und den Reaktor verlässt. Aufgrund ihrer großen Bedeutung für die chemische, pharmazeutische, biochemische und petrochemische Industrie verfolgen Ingenieure seit jeher das Ziel, die Leistungsfähigkeit von BSR zu verbessern, wobei man sich für diesen Zweck in den letzten Jahrzehnten vermehrt der numerischen Strömungssimulation (CFD) bedient. Obgleich bereits viele Studien zu BSR publiziert wurden, gibt es nach wie vor noch offene Fragen bezüglich der genauen Abläufe während des Betriebes, die vor allem auf die zahlreichen Wechselwirkungen der in BSR stattfindenden Vorgänge zurückzuführen sind. Zusätzlich erstrecken sich die auftretenden Vorgänge auch noch über mehrere Größenordnungen, sowohl auf der Zeitskala als auch auf der Längenskala.

Im Zuge dieser Doktorarbeit wird ein CFD Algorithmus entwickelt, mit dem sich dreidimensionale (Suspensions-) Blasensäulenreaktoren numerisch modellieren lassen, die im homogenen oder im heterogenen Strömungsregime betrieben werden. Dieser Algorithmus baut auf OpenFOAM®, einer quelloffenen Programmbibliothek, auf und verfolgt im Speziellen den Ansatz eines vierfach gekoppelten ereignisgesteuerten Euler-Lagrange (EL) Verfahrens. Der EL Ansatz bietet die Möglichkeit, die Interaktionen der Gasblasen in Blasenschwärmen, als auch deren Auswirkungen auf andere Prozessparameter und -vorgänge, zu studieren. Um dem höheren Ressourcenaufwand des EL Verfahrens entgegenzuwirken, werden in dieser Studie zudem auf dem Algorithmus basierende Ablaufbeschleunigungen für die Handhabung der Gasblasenschwärme präsentiert.

Der erste Teil dieser Arbeit beschäftigt sich mit den Auswirkungen von Gasblasenzerfall und -koaleszenz (Z&K) in einem quaderförmigen Labor-BSR, auf die Hydrodynamik, den

Massentransfer und den zeitlichen Ablauf von chemischen Reaktionen. Ein Vergleich der Simulationsergebnisse von monodispersen und polydispersen Blasenschwärmen zeigt, dass Z&K zwar sehr wohl einen Einfluss auf den Massentransfer und den zeitlichen Ablauf von Reaktionen hat, die Hydrodynamik im BSR hingegen kaum beeinflusst wird.

Der zweite Teil dieser Arbeit befasst sich mit der Modellierung von Dreiphasenströmungen mittels EL Ansatzes, wobei der Schwerpunkt auf der Modellierung der Wechselwirkungen zwischen Gasblasen und Feststoffteilchen liegt. Letztere sind auftriebsneutrale Feststoffkugeln, die in einem zylindrischen Labor-BSR einen Volumenanteil von *1.6 vol-%* einnehmen. Die Ergebnisse zeigen einen vertikalen Transport der Feststoffteilchen, als auch einen signifikanten Einfluss der Suspensionsviskosität auf den lokalen Gasanteil. Von allen getesteten Wechselwirkungsmodellen sagt das Widerstandskraftmodifikationsmodell die gleichmäßigste Feststoffverteilung und die niedrigsten Gasgeschwindigkeiten voraus, während das elastische Kollisionsmodell und das Mehrstufenkollisionsmodell ähnliche Strömungseigenschaften kalkulieren.

Acknowledgements

First of all, I want to thank my supervisor *Johannes Khinast* for giving me the opportunity to do this research and for his dedication in guiding me during the doctoral program. Also, I want to express my thanks to *Stefan Radl*, on whose preliminary work these studies build on. Further, I want to thank *all my (current and former) colleagues* at the Institute for Process and Particle Engineering, with whom I spent a lot of time at and after work. I hope that the friendships, which have been founded during this time, will continue and that we will meet again from time to time. Special thanks also go to *Michaela Cibulka, Lydia Fraidl, Silvia Houben, Christoph Kutschera, Alexander Muhr, Adela Roller* and *Siegfried Wolf* for their assistance with administrative matters.

Moreover, I want to thank the *Austrian Science Fund (FWF)* for supporting the project “Bubble swarms and reactive mass transfer at dynamic interfaces” through the grant P19639.

Furthermore, I would like to mention that the algorithms used in these studies are based on the open-source software OpenFOAM®. OpenFOAM® is a registered trademark of OpenCFD Limited, a wholly owned subsidiary of ESI Group.

I also want to thank *Stefan Enzinger*, who helped me with the C++ coding.

My deepest gratitude goes to my love *Sylvie*. I cannot overemphasize my gratefulness for your patience, your support and your encouragement during the whole time of this stage of life project doctorate. The past thirteen years have been wonderful and I am looking forward to the common happy years lying ahead of us.

Further, I want to thank my grandparents *Johann* and *Rosina* as well as my beloved *aunt Maria*, who became inspiring role models for me. I would not be where I am today, without your support.

In conclusion, I want to thank my family: *Stefan, Rosi, Gerald, Kerstin, Bernhard, Kristina, Nella, Josef* and *Tina*. Vielen Dank für Eure Unterstützung.

Graz, March 18th 2015

CHAPTER

I

“Science is organized knowledge.”

– Herbert Spencer (1820-1903)

Introduction

1.1 Multiphase Flow Theory

A thermodynamic *phase* refers to a solid, a liquid or a gaseous state of matter. *Multiphase flows* are thus defined as simultaneous flows of materials, either with different phases (e.g. gas-liquid flows like bubbly flows or liquid-solid flows such as suspensions), or with same phases but with different physical properties (e.g. liquid-liquid flows like droplet flows). Each of the at least microscopically distinguishable phases takes thereby its own velocity field, temperature and volume. In contrast, a *multicomponent flow* is characterized as the simultaneous flow of a mixture, whereby the various components are mixed at the molecular level and have the same velocity and temperature (Gergely, 2010). Several examples for multiphase flows in technical applications are listed in Tab. 1.1.

Multiphase flows can be classified according to various criteria:

- The simplest classification is based on to the *presence of the phases*, e.g. gas-liquid flows, liquid-liquid flows or gas-liquid-solid flows.

Table 1.1: Examples of multiphase flows in technical applications.

Continuous phase	Dispersed phase(s)	Technical applications
gas	liquid	spray (e.g. cooling), atomizer, combustor
gas	solid	coal dust combustion, fluidized bed, pneumatic conveying (e.g. of flour), cyclone separator
liquid	gas	bubble column, absorption, stripping
liquid	liquid	extraction, mixing (e.g. emulsion polymerization)
liquid	solid	continuous plug flow crystallization, hydraulic conveying, sedimentation
liquid	gas-solid	flotation, slurry bubble column, aerated stirred biochemical reactor (e.g. fermentation)

- The flows can also be characterized by the *shape of the interface* as dispersed flows, separated flows or mixed flows. A phase is called *continuous*, if it is continuously connected throughout the regions of space (carrier phase) and is called *dispersed*, if it occupies only disconnected regions of space (e.g. bubbles, droplets or particles). In *dispersed flows*, one or more dispersed phases are distributed within a continuous phase, as illustrated in Fig. 1.1. In *separated flows*, all phases exist in semi-continuous forms that are separated by interfaces. Hybrid forms of dispersed and continuous flows are called *mixed flows* (Ranade, 2002).

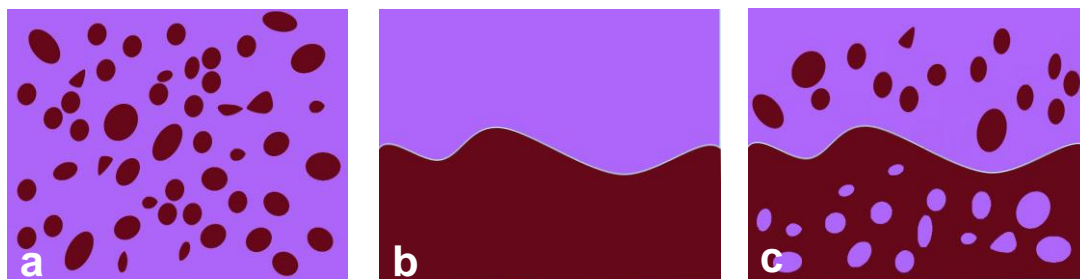


Figure 1.1: Multiphase flows with (a) dispersed, (b) separated and (c) mixed interfaces.

- Regarding the dispersed phase, flows can additionally be classified into dilute or dense flows. In *dilute flows*, the motion of the dispersed phase is governed by fluid forces, while in *dense flows*, the motions of the dispersed particles mainly result from interactions among themselves (Crowe et al., 2011).

1.2 Bubble Column Reactors

Bubble columns (BCs) are simply constructed and economically operated apparatus which are applied in manifold industrial processes for the purpose of bringing two (gas-liquid) or three phases (gas-liquid-solid) into contact. During operation time, a gas/gas mixture rises in form of distributed bubbles (dispersed phase) through a liquid/liquid mixture (continuous phase) or a suspension (slurry), whereupon interphase mass transfers occur and chemical reactions take place. If the column contains a suspension, it is often called slurry BC.

Basically, industrial BCs are stainless steel vessels of vertical cylindrical shape that are filled with liquid, as shown in Fig. 1.2. They are usually designed with a length-to-diameter ratio of at least 5. Especially, in biochemical applications this ratio varies between 2 and 5 (Kantarci et al., 2005). BCs for the mass production of chemicals have capacities between 30 m^3 and 300 m^3 . The volumes of fermenters, utilized for protein production from methanol, reach up to $3,000\text{ m}^3$. The biggest BCs are applied for wastewater treatment and have capacities of $20,000\text{ m}^3$.

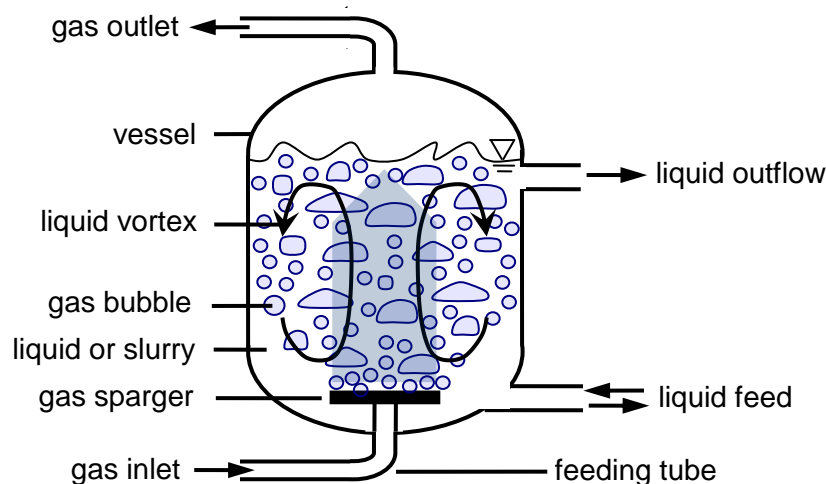


Figure 1.2: Schematic cross-sectional view through a (slurry) BC during operation.

A gas pipe leads at the column's bottom into the interior and ends in a *gas sparger* (distributor plate). During operation time, the gas sparger distributes a continuously flowing gas stream in the form of bubbles into the liquid. In most cases, the bubbles are generated by a static gas sparger (which operates without additional energy supplies from outside). Some

typical sparger forms are shown as example in Fig. 1.3. Afterwards, the bubbles ascend in the surrounding medium until they reach the top surface, whereupon they burst. Their gas is then exhausted through another pipe, mounted at the top of the BC. In some cases, heat exchanger tubes may additionally be mounted on the inside walls for cooling/heating of the liquid during exothermic/endothermic reactions. Further, baffles are used in some reactors in order to divide the BC into sections and hence, reduce the effect of liquid backmixing.

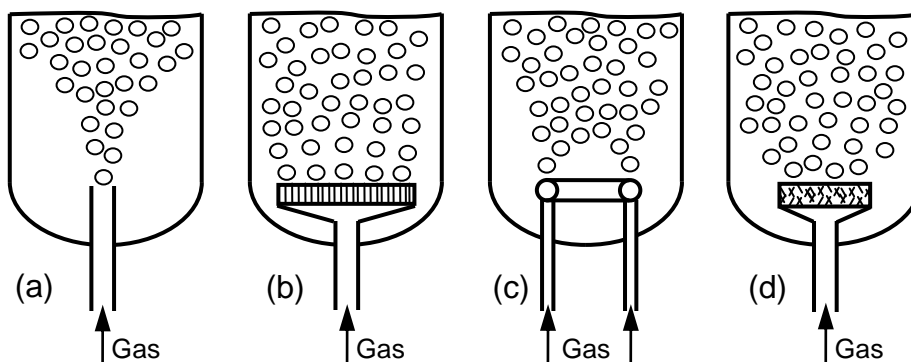


Figure 1.3: Various static sparger forms (Bauer et al., 2002): (a) dip tube, (b) perforated plate, (c) perforated ring sparger and (d) porous plate.

BCs can be operated in either *continuous* or in *semi-batch mode*, regarding the handling of the liquid phase. In semi-batch mode, the column is refilled with liquid, whereupon the liquid is aerated until a desired final state is reached. Afterwards, the aeration is stopped and the column is completely refilled again. On the contrary, in continuous mode the refilling and emptying of the column take continuously place during the operation time.

The wide-spread of (slurry) BCs is based on some *beneficial qualities* in both, construction and operation (Kantarci et al., 2005; Chilekar, 2007). The most out-standing advantages and disadvantages of BCs are listed up in Tab. 1.2.

Table 1.2: Advantages and disadvantages of (slurry) BCs compared to other reactor types.

Advantages	Disadvantages
Excellent mass transfer characteristics	High liquid backmixing
Excellent heat transfer characteristics	Low cycle conversion
Good mixing characteristics	Fouling of sparger
High gaseous hold-up	Chaotic hydrodynamics
Online catalyst addition and extraction ability	Complex modelling
Simple construction including no internal moving parts	
Low costs for operation and maintenance	

Further, a representative selection of industrial multiphase processes for (slurry) BCs is summarized in Tab. 1.3.

Table 1.3: Overview of some industrial processes performed with (slurry) BCs.

Industries	Processes	Products
chemical	alkylation, carbonylation, carbonatation, chlorination, hydroformylation, hydrogenation, oxidation, oxychlorination, polymerization	<i>bulk and fine chemicals:</i> acids, alcohols, aldehydes, amines, dyes, esters, inorganic acids, oils, polymers
biotechnological pharmaceutical	bacteria cultivation, animal cell cultivation, fermentation	antibiotics, cell reproduction, enzymes, ethanol, flavors, fragrances, proteins
petrochemical	coal liquefaction, dewaxing, Fischer-Tropsch synthesis	gases, liquid fuels, oils
environmental remediation	biological wastewater treatment, flue-gas denitrification (De-NO _x), flue-gas desulfurization (De-SO _x), hydrochlorofluorocarbons (HCFCs), wet oxidation of sludge	purified air, purified water
hydrometallurgical	refining of metallic ores	iron, ilmenite

Most of the above listed industrial processes involve an interphase mass transfer from the gas to the liquid phase. Examples include the carbonation of lime or the cultivation of cells, wherefore the gas supplies a reactant or the vitally important oxygen. In most of these processes, the volumetric mass transfer coefficient $k_L a$, which is composed of the liquid-side mass transfer coefficient k_L and the gas-liquid interfacial area a , is the limiting factor that determines the overall reaction rate and the rate of growth of the cells. As a consequence, $k_L a$ is a key parameter for design and scale-up of BCs. However, the interfacial area and thus $k_L a$ highly depend on the prevailing hydrodynamic flow regime, a BC is operated at. Therefore, the main flow regimes of gas-liquid two-phase flow will be explained in the next chapter.

1.3 Gas-Liquid Two-Phase Flows

The superficial gas velocity u_s of a column is defined as the ratio of gas volume flow rate Q to the cross-sectional area A of the column:

$$u_s = \frac{Q}{A}. \quad (1.1)$$

Depending on the operating conditions, the gas-liquid two-phase flow in a column can have different forms of appearance, which are also known as *flow regimes* or *flow patterns*. Which flow regime is going to establish under a certain operating condition in a column depends on many factors, e.g. the material properties or the pressure level. However, the two factors that have the greatest impact on the current flow regime are the superficial gas velocity and the column diameter. Fig. 1.4 illustrates the four main flow regimes for a vertical column, namely the bubbly flow regime, the churn-turbulent flow regime, the slug flow regime and the annular flow regime.

The *bubbly flow regime*, also known as *homogeneous flow regime*, appears at low u_s . Within this flow regime, the bubble flow is so dilute that almost no break-ups or coalescences (B&Cs) occur, wherefore the diameters of the bubbles are directly correlated with the opening diameters of the sparger orifices. In this flow regime, the bubbles ascend with uniform velocities and evenly distributed over the whole cross-section of the column. Further, only low turbulences appear in the liquid phase, resulting in a gentle blending of the liquid (Kantarci et al., 2005).

If the column diameter remains constant and u_s is increased, the flow regime changes into the *churn-turbulent*, which is also called *heterogeneous flow regime*. This flow regime is characterized by dense bubble flow and increased liquid turbulence and recirculation, causing bubble B&C. Additionally, broad bubble size distributions, bubble cluster formations and intense mixing are also reported in literature as typical properties for churn-turbulent flow. Most of the industrial BCs are operated under heterogeneous flow conditions.

If u_s is further increased, the flow regime changes into *slug flow*, which is characterized by big bubbles that cover the entire cross-section of the column. This flow regime is only observed in BCs with small diameters. A further increase of the superficial velocity results in

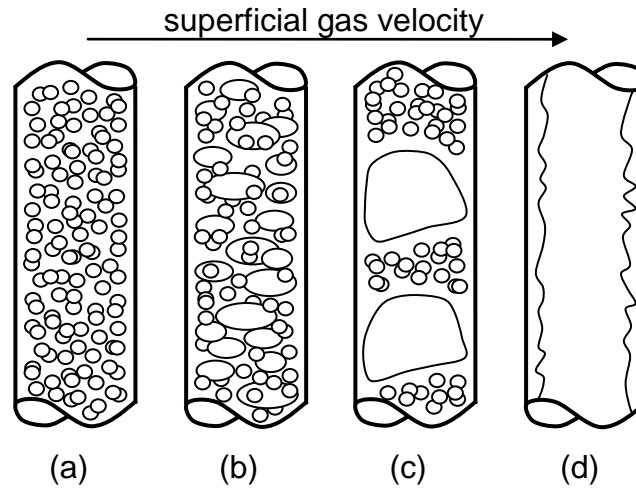


Figure 1.4: Flow patterns in a vertical column. With increasing superficial velocity, the flow regime changes from (a) homogeneous bubbly flow to (b) heterogeneous churn-turbulent flow, further to (c) slug flow and finally to (d) annular flow.

a continuous gas flow channel in the middle of the column. In this flow regime that is called *annular flow*, bubbles are no longer present and the liquid phase exists as film along the walls.

Several studies have been published in literature, in which the established flow regime was quantitatively described, in a so-called *flow regime map*, as function of the superficial gas velocity and the BC diameter, as shown in Fig. 1.5. In this figure, the red areas indicate *transition regions* between the various flow regimes. With the help of such maps, the operating conditions for a particular flow regime can be approximated. However, the exact localization of the boundary regions depends, nonetheless, on the particular operating conditions of the BC under investigation.

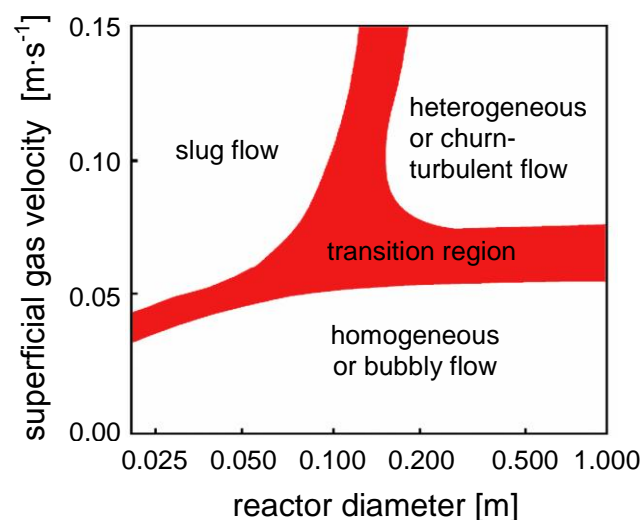


Figure 1.5: Flow regime map for an air-water system at ambient pressure (Shah et al., 1982).

As mentioned in the previous chapter, the volumetric mass transfer coefficient k_{La} strongly depends on the prevailing flow regime. Fig. 1.6 shows a typical literature study for the correlations between k_{La} and u_S : In the homogeneous flow regime, k_{La} as well as the gas volume fraction α_G increase linearly with the superficial gas velocity. Further, it can be seen in this figure that k_{La} and α_G directly correlate with the initial sizes of the bubbles and are consequently related with the diameters d_0 of the sparger orifices. At a gas velocity of $0.04 \text{ m}\cdot\text{s}^{-1}$, the homogeneous flow regime changes to the transition regime, in which the linear correlations break. At the superficial gas velocity of $0.12 \text{ m}\cdot\text{s}^{-1}$, the heterogeneous flow regime starts wherein due to B&C k_{La} and α_G become independent of the sparger geometry.

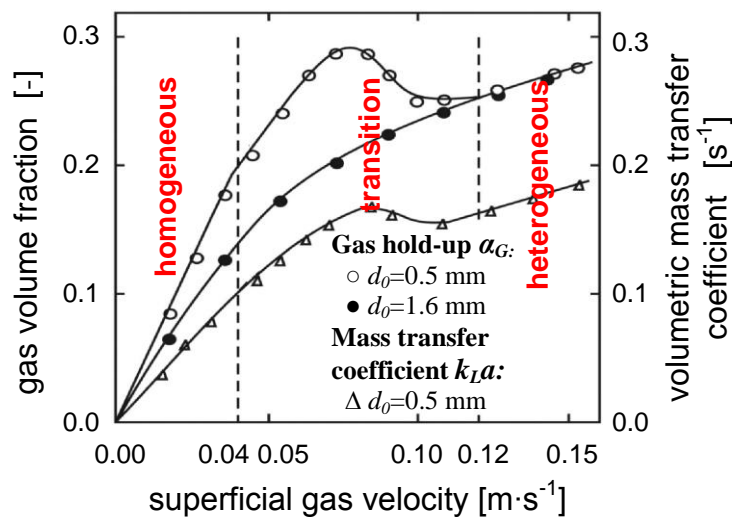


Figure 1.6: Gas volume fraction α_G and volumetric mass transfer coefficient k_{La} as function of the superficial gas velocity u_S (Zahradnik and Fialova, 1996). The initial bubble diameter is here denoted with d_0 .

1.4 Computational Methods for Multiphase Flows

Owing to their wide spread and importance in industrial processes, the improvement of (slurry) BCs has always been a goal for engineers. In the course of time, a lot of studies have been published in literature concerning the design, scale-up and performance enhancement of BCs (see e.g. [Froment and Bischoff, 1979](#); [Perry et al., 2005](#); [Fogler, 2006](#); [Lee, 2006](#); [Davis and Davis, 2012](#)). Traditionally, empirically derived correlations, which e.g. were obtained through dimensional analysis, have been applied therefore. These correlations consist of global process parameters and are usually only valid for special reactor geometries and/or operating conditions.

In the last decades, along with the progression in computer hardware and modeling software for multiphase flows, computational fluid dynamics (CFD) has become a (supplementary) powerful tool for both, engineers and scientists (see e.g. [Stewart and Wendroff, 1984](#); [Kuipers and van Swaaij, 1997](#); [Brennen, 2005](#); [Kolev, 2005](#); [Mammoli and Brebbia, 2005](#); [Prosperetti and Tryggvason, 2007](#); [Jakobsen, 2008](#); [Andersson et al., 2011](#); [Crowe, 2006](#)). Thereby, the CFD offers a number of advantages compared to a pure empirical approach: With relative few investments in terms of time and costs, CFD allows to gain *a priori* information of reactors, e.g. to determine the most limiting factor for the performance of a reactor or to calculate the optimum height-to-diameter ratio of a full-scale BC. Further, CFD is increasingly utilized for fundamental studies, in order to gain a better understanding of the underlying physics of multiphase flows. In doing so, it is possible to explore the influence of a specific phenomenon on the total performance of the reactor, e.g. the influence of bubble B&C, by switching the phenomenon off or on.

During the last decades, the following four approaches, namely the Euler-Euler, the mixture, the Euler-Lagrange and the volume-of-fluid, have become well-established for modeling of multiphase flows ([Anderson et al., 2011](#); [Rahman and Brebbia, 2012](#)).

In the *Euler-Euler* (EE) approach, which is also known as *two-fluid* or *multi-fluid* model, all phases are treated as continuous quasi-fluids, which interpenetrate each other. Due to the continuous representation of the phases, the EE approach is suitable for the modeling of separated phase flows. Additionally, if the main interest lies on the overall motion of the dispersed phases, then the individual movement of particles becomes negligibly and the EE

method can also be applied for the modeling of dispersed phase flows. The dispersed phases are then treated as continua too, which implies dense flows with high volume fractions of particles. Each phase is then represented through a set of volume-averaged or ensemble-averaged conservation equations for mass and momentum. The various phases are coupled with each other through a shared pressure and interphase exchange coefficients, whereby the latter have to be modeled. The governing equations for the EE method are described below (Ranade, 2002).

The volume fraction α_K describes the fraction of volume of phase K in a spatial volume. In order to get meaningful results, the volume fractions must complement each other to unity:

$$\sum_K \alpha_K = 1. \quad (1.2)$$

The continuity and the momentum balance equation are defined for each phase through:

$$\frac{\partial(\alpha_K \rho_K)}{\partial t} + \nabla \cdot (\alpha_K \rho_K \mathbf{u}_K) = \sum_Q S_{m,KQ}, \quad (1.3)$$

$$\frac{\partial(\alpha_K \rho_K \mathbf{u}_K)}{\partial t} + \nabla \cdot (\alpha_K \rho_K \mathbf{u}_K \mathbf{u}_K + \alpha_K \boldsymbol{\tau}_K) = \alpha_K \rho_K \mathbf{g} - \alpha_K \nabla p + \mathbf{S}_{M,K}, \quad (1.4)$$

where the phase properties \mathbf{u}_K , $\boldsymbol{\tau}_K$ and ρ_K are the velocity, the stress tensor and the density of the particular phase K, respectively. The liquid pressure, the gravitational constant and the time are termed as p , \mathbf{g} and t . Coupling between the phases K and Q (with $K \neq Q$) is considered via the source terms for momentum transfer $\mathbf{S}_{M,K}$ and mass transfer $S_{m,KQ}$:

$$\mathbf{S}_{M,K} = \sum_Q C_{KQ} (\mathbf{u}_Q - \mathbf{u}_K) + \sum_Q S_{m,KQ} \mathbf{u}_K, \quad (1.5)$$

with the interphase momentum exchange coefficients C_{KQ} .

A simplified variation of the EE approach is the so-called *mixture* method, which is also known as algebraic-slip model. Based on the assumption that the different phases strongly interact with each other, the conservation equations are calculated only once, namely for the average of the entire mixture. The flow behavior of the particular phases is thereafter determined via the introduction of relative velocities between the individual phases and the average velocity of the mixture.

In the *Euler-Lagrange* (EL) method, the dispersed phases are tracked on the level of individual particles, while the continuous phase is treated as continuum, as described above.

Thereby, the dispersed particles can be droplets, bubbles or solid particles. In order to determine the movements of the dispersed particles, a translational equation of motion has to be solved for each particle. For the modeling of the interactions of the dispersed phases among each other, the so-called *hard-sphere* and *soft-sphere* approaches are widely used. In the hard-sphere approach, the particles do not overlap and the progression of the system time is event-driven. Thus, the system time proceeds chronologically from particle interaction (i.e. collision) to particle interaction. For example, when two dispersed particles collide, their new velocities are calculated, whereupon all particles are moved forward to the next collision occurring in the system. Contrary, in the soft-sphere approach, the system time advances constantly (time-driven), what causes particle overlaps. If two particles overlap, repulsive forces begin to act upon them until the overlap is removed. In the EL method, the continuous and dispersed phases interact with each other through exchange terms for momentum and mass. The governing equations for this approach are shown below.

The volume fractions of the continuous phase and the dispersed phases, here denoted with the subscripts L and P, respectively, sum up to one:

$$\alpha_L + \sum_P \alpha_P = 1. \quad (1.6)$$

Further, the continuous phase is described through volume-averaged equations for mass and momentum conservation:

$$\frac{\partial(\alpha_L \rho_L)}{\partial t} + \nabla \cdot (\alpha_L \rho_L \mathbf{u}_L) = S_{m,L}, \quad (1.7)$$

$$\frac{\partial(\alpha_L \rho_L \mathbf{u}_L)}{\partial t} + \nabla \cdot (\alpha_L \rho_L \mathbf{u}_L \mathbf{u}_L + \alpha_L \boldsymbol{\tau}_L) = \alpha_L \rho_L \mathbf{g} - \alpha_L \nabla p + \mathbf{S}_{M,L}, \quad (1.8)$$

while the motion of the dispersed particles is described via the equations of motion:

$$\rho_P \nu_P \frac{d\mathbf{u}_P}{dt} = \sum \mathbf{F} - \rho_P \mathbf{u}_P \frac{d\nu_P}{dt}, \quad (1.9)$$

$$\frac{d\mathbf{x}_P}{dt} = \mathbf{u}_P. \quad (1.10)$$

Therein, the sum of all forces (net force), a single dispersed particle with the volume ν_P and the position \mathbf{x}_P experiences in the presence of the continuous phase, is denoted with $\sum \mathbf{F}$. Further, the source term $s_{m,P}$ for the interphase mass transfer of a single particle is calculated

by:

$$\rho_p \frac{dv_p}{dt} = s_{m,p}. \quad (1.11)$$

The *volume-of-fluid* (VOF) method is applied to resolve the continuous flow around some few dispersed particles. Thereby, the VOF approach relies on the assumption that the various phases are separated through interfaces and hence, do not interpenetrate each other. Consequently, a single set of conservation equations can be used for the time-dependent description of all phases:

$$\frac{\partial \rho}{\partial t} + \nabla \cdot (\rho \mathbf{u}) = S_m, \quad (1.12)$$

$$\frac{\partial (\rho \mathbf{u})}{\partial t} + \nabla \cdot (\rho \mathbf{u} \mathbf{u} + \boldsymbol{\pi}) = \rho \mathbf{g} + \mathbf{S}_M, \quad (1.13)$$

where $\boldsymbol{\pi}$ is the momentum flux. If a particular control volume contains more than one phase, averages have to be used for the quantities in Eqs. (1.12) and (1.13) that are determined with the help of the phases' volume fractions α_K :

$$\rho = \sum_K \alpha_K \rho_K, \quad (1.14)$$

$$\xi = \frac{\sum_K \alpha_K \rho_K \xi_K}{\sum_K \alpha_K \rho_K}, \quad (1.15)$$

whereby ξ_K represents any quantity in the above equations. The interfaces between the various phases are obtained by solving the following continuity equations for the volume fractions α_K :

$$\frac{\partial \alpha_K}{\partial t} + (\mathbf{u}_K \cdot \nabla) \alpha_K = S_{\alpha,K}. \quad (1.16)$$

Fig. 1.7 illustrates the main advantages and disadvantages of the aforementioned modeling methods, especially for two-phase bubbly flows: The EE method enables the modeling of industrial full-scale BCs, but cannot resolve information on the bubble level, wherefore additional closure terms are needed. Contrary, only the motion of a few bubbles can be modeled with the VOF approach. However, the VOF approach allows e.g. the direct simulation of bubble B&C.

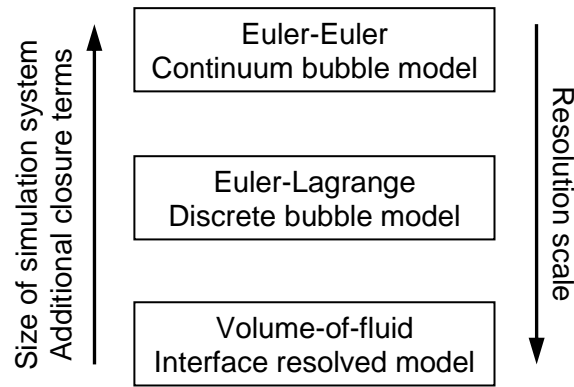


Figure 1.7: Advantages and disadvantages of the multiphase flow modeling methods (adopted from [Rahman and Brebbia, 2012](#)).

The two approaches, the EE and the EL, are widely used for the modeling of chemical reactors such as BCs. However, both methods have their advantages and disadvantages: As mentioned above, the EE approach is the state-of-the-art method for the modeling of full-scale reactors, since this method requires only low computational costs, while the system sizes, simulated with the EL method, are restricted to laboratory-scale or small pilot-scale BCs ([Garcia et al., 2005](#)). Additionally, the EL method is not well-suited for parallel computing. A drawback of the EE method is that due to the averaging procedure in this method, information like the number of bubbles in each grid cell, gets lost and has to be modeled additionally, e.g. via empirical closure terms. Thereby, the empirical closure terms commonly rely on the local gas fraction and account for phenomena such as bubble B&C. In contrast, the EL method does not need to model bubble properties, since they are already part of the solution. Hence, the EL approach gives a physically more realistic view on phenomena occurring at the bubble scale and enables the direct observation of e.g. the shrinkage of individual bubbles due to dissolution in the liquid.

Finally, regarding the coupling of the phases in simulations, gas-liquid flow modeling can be classified as shown in Tab. 1.4. *One-way* coupling is used for sufficiently dilute flows, in which the liquid remains unaffected by the presence of the particles, while the *two-way* coupling is applied for systems, in which the number of particles is sufficiently high, in order to disturb the motion of the liquid. In both coupling techniques, bubbles can interact with the reactor too, e.g. through collisions with reactor walls. If the number of bubbles increases and the bubble flow becomes dense enough (heterogeneous regime), interactions between the bubbles, e.g. collisions and coalescences, have to be considered additionally. For such dense flows, the *four-way* coupling technique has to be used.

Table 1.4: Classification of phase coupling in bubbly flows according to [Elghobashi \(1991\)](#).

Coupling	Suspension	Interactions
one-way	dilute	Liquid \longrightarrow Bubble \longleftrightarrow Reactor
two-way	dilute	Liquid \longleftrightarrow Bubble \longleftrightarrow Reactor
four-way	dense	Liquid \longleftrightarrow Bubble \longleftrightarrow Bubble \longleftrightarrow Reactor

1.5 Objective and Outline

The objective of this thesis is to (further) develop a transient four-way coupled three-dimensional Euler-Lagrange algorithm which enables the simulation of dispersed flows by using the hard-sphere model approach. In doing so, the algorithm correctly resolves all the phenomena that spread over several magnitudes in length and time scale. Additionally, the algorithm accounts for liquid-bubble, bubble-liquid, bubble-bubble, bubble-reactor, liquid-reactor and liquid-liquid interactions. The algorithm is then used for the simulation of well-investigated bubble column reactor experiments reported in literature, in order to study the phenomena occurring during the operation time and hence, to obtain a better insight into those. Thereby, special focus is put on the impact of bubble B&C in bubbly flows on the hydrodynamics, the mass transfer and the temporal progression of chemical reactions.

In chapter 2, two in literature well-known models for B&C are incorporated in a stochastic manner in order to generate polydisperse bubble swarms, whose diameter distributions are affected by the intensity of the liquid turbulences. Thereafter, the impact of these polydisperse swarms on the hydrodynamics of gas-liquid flows, the gas hold-up and the interfacial area is investigated and the results are compared with the outcome of simulations with monodisperse bubble swarms. As setup for the simulations serves the in literature well-know “Deen case” (see [Deen et al., 2001](#)).

In chapter 3, the investigations concerning bubble B&C are continued. Especially, the impacts of B&C on the absorption of carbon dioxide in water and on the chemisorption of carbon dioxide in sodium hydroxide solutions of pH between *12.0* and *14.0* are investigated. Again, the “Deen case” is chosen as setup case for the simulations.

Finally in chapter 4, an algorithm is presented for the modeling of gas-liquid-solid flows in bubble columns. Thereby, the gaseous phase and the solid phase are handled via the Lagrangian approach, while the Eulerian approach is used for the liquid phase. The experiments of [Gan \(2013\)](#) are chosen as setup for the simulations. The main focus in these examinations is put on the interactions between the two dispersed phases, wherefore various interaction models are verified. Additionally, algorithm-based speed-up techniques are presented, which are necessary for an efficient handling of the enormous number of bubbles and solid particles during the simulations.

Notation

Latin Letters

a	volume specific gas-liquid interfacial area, (m^{-1})
A	cross-sectional area, (m^2)
C	interphase momentum exchange coefficients, ($\text{kg}\cdot\text{m}^{-3}\cdot\text{s}^{-1}$)
\mathbf{F}	force, (N)
\mathbf{g}	gravitational acceleration vector, ($\text{m}\cdot\text{s}^{-2}$)
k_L	liquid-side mass transfer coefficient, ($\text{m}\cdot\text{s}^{-1}$)
$k_L a$	volumetric mass transfer coefficient, (s^{-1})
p	pressure, (Pa)
Q	volume flow rate, ($\text{m}^3\cdot\text{s}^{-1}$)
s_m	source term of mass transfer for a dispersed particle, ($\text{kg}\cdot\text{s}^{-1}$)
S_m	source terms of mass transfer, ($\text{kg}\cdot\text{m}^{-3}$)
\mathbf{S}_M	source terms of momentum transfer, ($\text{N}\cdot\text{m}^{-3}$)
t	time, (s)
u_S	superficial gas velocity, ($\text{m}\cdot\text{s}^{-1}$)
\mathbf{u}	velocity, ($\text{m}\cdot\text{s}^{-1}$)
\mathbf{x}	position, (m)

Greek Letters

α	hold-up or volume fraction, (-)
π	momentum flux, ($\text{kg}\cdot\text{m}^{-1}\cdot\text{s}^{-2}$)
ρ	density, ($\text{kg}\cdot\text{m}^{-3}$)
τ	stress tensor, ($\text{N}\cdot\text{m}^{-2}$)
ν	volume, (m^3)

Subscripts

K, Q	continuous or dispersed phase
L	continuous phase, liquid
P	dispersed phase
G	gaseous

References

- Andersson, B., Andersson, R., Hakansson, L., Mortensen, M., Sudiyo, R., van Wachem, B., 2011. *Computational fluid dynamics for engineers*. Cambridge University Press, United Kingdom.
- Bauer, K., Garbe, D., Surburg, H., (Eds.), 2002. *Ullmann's Encyclopedia of Industrial Chemistry*. John Wiley & Sons Ltd, New York, USA.
- Brennen, C.E., (Ed.), 2005. *Fundamentals of multiphase flow*. Cambridge University Press, United Kingdom.
- Chilekar, V.P., 2007. *Hydrodynamics and mass transfer in slurry bubble columns: scale and pressure effects*. PhD Thesis, Technische Universiteit Eindhoven, Eindhoven, The Netherlands.
- Crowe, C.T., Schwarzkopf, J.D., Sommerfeld, M., Tsuji, Y., 2011. *Multiphase flows with droplets and particles*. CRC press, Boca Raton, Florida, USA.
- Crowe, C.T., (Ed.), 2006. *Multiphase flow handbook*. CRC press, Boca Raton, Florida, USA.
- Davis, M.E., Davis, R.J., (Eds.), 2012. *Fundamentals of chemical reaction engineering*. McGraw-Hill, New York, USA.
- Deckwer, W.D., 1992. *Bubble column reactors*. John Wiley&Sons, Chichester, United Kingdom.
- Deen, N.G, Solberg, T., Hjertager, B.H., 2001. *Large eddy simulation of the Gas-Liquid flow in a square cross-sectioned bubble column*. Chem. Eng. Sci. 56(21), 6341–6349.
- Elghobashi S., 1991. *Particle-laden turbulent flows: direct simulation and closure models*. Appl. Sci. Res. 48(3–4), 301–314.
- Fogler, H.S., 2006. *Elements of chemical reaction engineering*. Pearson Education, Westford, Massachusetts, USA.
- Froment, G.F., Bischoff, K.B., 1979. *Chemical Reactor Analysis and Design*. John Wiley & Sons, New York, USA.
- Gan, Z.W., 2013. *Hold-up and velocity profiles of monosized spherical solids in a three-phase bubble column*. Chem. Eng. Sci. 94, 291–301.
- Garcia, M., Sommerer, Y., Schönfeld, T., Poinso, T., 2005. *Evaluation of Euler/Euler and Euler/Lagrange Strategies for Large Eddy Simulations of Turbulent Reacting Flows*. ECCOMAS Thematic Conference on Computational Combustion.
- Gergely, K, 2010. *Multiphase flow modeling*. Ara.bme.hu. Last downloaded on March 6th, 2015 from https://www.ara.bme.hu/oktatas/tantargy/NEPTUN/BMEGEATMW02/2010-2011-I/9_MultiphaseFlows.pdf

- Wörner, M., 2003. *A compact introduction to the numerical modeling of multiphase flows*. bibliothek.fzk.de. Report Forschungszentrum Karlsruhe, FZKA 6932. Last downloaded on March 6th from <http://bibliothek.fzk.de/zb/berichte/FZKA6932.pdf>
- Jakobsen, H.A., (Ed.), 2008. *Chemical reactor modeling*. Multiphase Reactive Flows, Springer-Verlag, Berlin, Germany.
- Kantarci, N., Borak, F., Ulgen, K.O., 2005. *Bubble column reactors*. Process Biochem. 40(7), 2263–2283.
- Kolev, N.I., (Ed.), 2005. *Multiphase flow dynamics*. Springer-Verlag, Berlin, Germany.
- Kuipers, J.A.M., van Swaaij, W.P.M., 1997. *Application of computational fluid dynamics to chemical reaction engineering*. Rev. Chem. Eng. 13(3), 1–118.
- Lee, S., (Ed.), 2006. *Encyclopedia of Chemical Processing-Volume 1*. Taylor & Francis, New York, USA.
- Mammoli, A.A., Brebbia, C.A., (Eds.), 2005. *Computational Methods in Multiphase Flow VI*. WIT Press, Southampton, United Kingdom.
- Perry, R.G., Chilton, C.H., Kirkpatrick, S.D., (Eds.), 2005. *Perry's chemical engineers' handbook*. McGraw-Hill, New York, USA.
- Prosperetti, A., Tryggvason, G., (Eds.), 2007. *Computational methods for multiphase flow*. Cambridge University Press, United Kingdom.
- Rahman, M., Brebbia, C.A., (Eds.), 2012. *Advances in Fluid Mechanics IX*. WIT Press, Southampton, United Kingdom.
- Ranade, V.V., 2002. *Computational Flow Modeling for Chemical Reactor Engineering*. Academic Press, London, United Kingdom.
- Shah, Y.T., Kelkar, B.G., Godbole, S.P., Deckwer, W.D., 1982. *Design parameters estimations for bubble column reactors*. AIChE J. 28(3), 353–379.
- Stewart, H.B., Wendroff, B., 1984. Two-phase flow: models and methods. J. Comput. Phys. 56(3), 363–409.
- Zahradnik, J., Fialova, M., 1996. *The effect of bubbling regime on gas and liquid phase mixing in bubble column reactors*. Chem. Eng. Sci. 51(10), 2491–2500.

CHAPTER

2

“Engineering is the professional art of applying science to the optimum conversion of natural resources to the benefit of man.”
– Ralph J. Smith (1917-1997)

Bubble Breakage and Coalescence in Euler–Lagrange Simulations¹

Abstract

A systematic study of the impact of break-up and coalescence on the hydrodynamics in a bubble column is presented. A stochastic approach was chosen for the integration of various break-up and coalescence kernels into a four-way coupled Euler-Lagrange model. The model is benchmarked against the “Deen case” (Deen et al., 2001) and good agreements were found for the gas hold-up and the bubble size distribution. While the results indicate that

¹ This chapter is based on: Gruber, M.C., Radl, S., Khinast, J.G., 2013. *Coalescence and Break-Up in Bubble Columns: Euler-Lagrange Simulations Using a Stochastic Approach*. Chem. Ing. Tech. 85(7), 1118–1130.

monodisperse bubbles suffice to correctly forecast the flow features, break-up and coalescence models are the key to predict the specific interfacial area, especially in the lower half of the bubble column.

2.1 Introduction

Bubble columns (BCs) are commonly used as multiphase reactors and contactors in the chemical, biochemical, mineral and petrochemical industries. Typical application areas are chemical processes like oxidation, carbonation and hydrogenation, biochemical processes such as fermentation and wastewater treatment, flotation processes in the mineral industry and petrochemical processes including gas conversion for synthetic fuels. The wide spread of BCs in industrial processes is based on a number of advantages compared to other reactor types: BCs have no moving parts, as the rising gas bubbles themselves induce a recirculating flow into the liquid and ensure mixing, leading to low operating and maintenance costs. Furthermore, this reactor type demonstrates very good heat and mass transfer characteristics ([Kantarci et al., 2005](#)).

The gas-liquid mass transfer is a key parameter for design, scale-up and performance enhancement of chemical reactors. The goal of most industrial processes is to realize high mass transfer rates from the gaseous to the liquid phase, in order to supply the gaseous reactant for a liquid phase reaction. In addition to the local flow conditions, the mass transfer especially depends on the gas-liquid interfacial area, which in turn is directly related to the gas volume fraction α_G and the bubble size distribution (BSD). Clearly, the generation of small bubbles is desired, while the presence of large bubbles in BCs should be avoided ([Akita and Yoshida, 1974](#); [Bouaifi et al., 2001](#)). Usually, the BSDs in BCs follow non-uniform distributions and result, apart from the gas-sparger design, from break-up and coalescence events ([Luo, 1993](#); [Lage and Esposito, 1999](#)).

Many studies concerning the mechanism of break-up and coalescence (B&C) have been performed, leading to a variety of models published in literature (e.g. [Lasheras et al., 2002](#); [Liao and Lucas, 2009, 2010](#); [Martinez-Bazan et al., 2010](#)). These models differ in their assumptions regarding the coalescence efficiency, the break-up frequency and the BSD of the so-called “daughter bubbles” – the bubbles which are generated through break-up. However, these studies are mostly dealing with the derivation of B&C models (kernel functions) for population balance equations (PBEs), while the impact of the B&C models on the hydrodynamics of bubbly flows has rarely been investigated. Nevertheless, the liquid flow

field and the BSD interdepend on each other: the local flow field is influenced by the α_G and the interphase momentum transfer rate Φ of the bubbles in this area. Moreover, B&C depends on the local flow conditions, causing a complex coupling of both, the gaseous and the liquid phase.

Over the past decades, in parallel with the progress in computer technology, the development of computational fluid dynamics (CFD) models for BCs was driven by the goal to obtain a better understanding of the hydrodynamics of bubbly flows. For the modeling of large-scale industrial reactors, which may contain hundreds of millions of bubbles, the Euler-Euler (EE) approach is typically used, due to its relatively low computational costs. This approach treats both phases as interacting continua, which are coupled through pressure and interphase exchange coefficients. However, the EE approach suffers from its lack of detail at the bubble level, which makes a direct modeling of processes occurring at this level, such as B&C, impossible.

In contrast, the Euler-Lagrange (EL) approach handles each bubble individually as a point volume: only the center of the bubble is tracked, whereas its volume is taken into account through the displacement of the surrounding liquid volume fraction $\alpha_L=(1-\alpha_G)$. The motions of the bubbles are calculated based on Newton's equation of motion, while the liquid is represented through modified Navier-Stokes equations. Typically, the EL approach offers a more detailed view on multiphase flow processes and is therefore widely used (Lain et al., 2002; Göz et al., 2006). Additionally, several studies showed that the EL approach is physically more realistic than the EE approach and hence, the former was preferred for studies concerning bubble coalescences (Lapin et al., 1994; Delnoij et al., 1997). However, the EL approach is limited due to its high computational costs of tracking a sufficiently large number of bubbles.

In literature, B&C was often neglected in the simulation of bubbly flows (e.g. Lapin et al., 1994; Delnoij et al., 1997; Deen et al., 2001a, 2001b; Darmana et al., 2005; Hu, 2005; Radl et al., 2010a, 2010b) while other studies were only concerned with bubble coalescence and have neglected bubble break-up (e.g. Sommerfeld et al., 2003; Darmana et al., 2006). In the last decade, B&C have increasingly been considered in EE simulations coupled with PBE-based models (e.g. Olmos et al., 2001; Lehr et al., 2002; Chen et al., 2005a, 2005b; Hansen, 2009). For example, Chen et al. used two-dimensional EE simulations and compared different B&C models by using the concept of small and big bubble classes. They achieved good agreements between their measured and simulated liquid velocity profiles, but obtained unrealistically

high gas volume fractions. Thus, they concluded that three-dimensional simulations have to be used for B&C simulations. Three-dimensional EL simulations including B&C for BCs were performed by [van den Hengel et al. \(2005\)](#) and [Lau et al. \(2010\)](#). The former group used the break-up model from Luo and Svendsen which was developed for energy-dissipation rates equal or higher than $0.5 \text{ m}^2 \cdot \text{s}^{-3}$. Since the average dissipation rate of their simulated BC was in the order of $0.01 \text{ m}^2 \cdot \text{s}^{-3}$, nearly no break-up occurred during their simulations. Lau et al. used a deterministic break-up criterion proposed by Hinze, which is based on the critical Weber number. Furthermore, they combined this criterion with a stochastic sampling of a U-shaped daughter BSD. Lau et al. reported a good agreement between their experimental and simulated liquid velocity profiles for a superficial gas velocity of $5 \text{ mm} \cdot \text{s}^{-1}$. Although their simulated BSD showed the same qualitative trend as in the reference case, detailed results regarding their obtained BSD, like the Sauter mean diameter, have not been reported.

Based on the recent work of Lau et al., a fully stochastic approach for B&C in EL simulations is proposed here. Thus, based on a random process it is decided, whether a bubble breaks up or not, and in case of break-up, again a random process is used to generate the daughter bubble sizes. The ultimate goal is to mimic the probabilistic nature of bubble break-up. Further, an attempt is made to answer the important question whether the inclusion of B&C provides more accurate predictions of bubbly flows compared to simulations with constant bubble diameters. For this purpose, two well-established models for binary B&C proposed by [Coulaloglou and Tavlarides \(1977\)](#) (C&T) and [Lee et al. \(1987a, 1987b\)](#) (LEE) are used. These models were originally developed for PBEs as kernel functions and are based on different assumptions regarding the break-up frequency, the daughter BSD and the coalescence efficiency. However, since a four-way coupled (see [Crowe, 2006](#)) three-dimensional EL approach is used here, the concept of a PBE is not needed *a priori*. Here, the well-studied Deen case (see [Deen et al., 2001a, 2001b](#)) is chosen as setup for the EL simulation of a BC to investigate the implementation of the fully stochastic approach for B&C.

2.2 Modeling

2.2.1 Liquid Hydrodynamics

The liquid is assumed to be incompressible, and hence its motion can be calculated through the solution of the volume-specific equations for mass and momentum conservation (the Navier-Stokes equations), which are given by:

$$\frac{\partial(\alpha_L \rho_L)}{\partial t} + \nabla \cdot (\alpha_L \rho_L \mathbf{u}_L) = 0, \quad (2.1)$$

$$\frac{\partial(\alpha_L \rho_L \mathbf{u}_L)}{\partial t} + \nabla \cdot (\alpha_L \rho_L \mathbf{u}_L \mathbf{u}_L) = -\alpha_L \nabla p - \nabla \cdot (\alpha_L \boldsymbol{\tau}_L) + \alpha_L \rho_L \mathbf{g} + \Phi, \quad (2.2)$$

where the liquid properties \mathbf{u}_L , $\boldsymbol{\tau}_L$, ρ_L and p are the velocity, the stress tensor, the density and the pressure, respectively. The direct numerical solution of Eqs. (2.1) and (2.2) is computationally expensive, wherefore the concept of large eddy simulations (LES) is used here and a filtered version of the two equations is solved. The velocity \mathbf{u}_L is then composed of the filtered grid-scale velocity $\bar{\mathbf{u}}_L$ and the unresolved sub-grid scale (SGS) velocity \mathbf{u}'_L :

$$\mathbf{u}_L = \bar{\mathbf{u}}_L + \mathbf{u}'_L. \quad (2.3)$$

After the filter operation, the unresolved liquid needs to be modeled in order to reflect its effect on the momentum balance equation. This is typically done via an effective viscosity yielding the following stress tensor $\bar{\boldsymbol{\tau}}_L$ in the filtered equations:

$$\bar{\boldsymbol{\tau}}_L = -\mu_{L,EFF} \left[2\bar{\mathbf{S}} - \frac{2}{3} \mathbf{I}(\nabla \cdot \bar{\mathbf{u}}_L) \right], \quad (2.4)$$

$$\bar{\mathbf{S}} = \frac{1}{2} \left[\nabla \bar{\mathbf{u}}_L + (\nabla \bar{\mathbf{u}}_L)^T \right], \quad (2.5)$$

with the unit tensor \mathbf{I} and the filtered rate of strain tensor $\bar{\mathbf{S}}$. The effective viscosity $\mu_{L,EFF}$ is given by the sum of the molecular viscosity μ_L and the SGS viscosity $\mu_{L,SGS}$:

$$\mu_{L,EFF} = \mu_L + \mu_{L,SGS}. \quad (2.6)$$

The SGS model from [Smagorinsky \(1963\)](#) is applied here for the modeling of the SGS viscosity:

$$\mu_{L,SGS} = \rho_L C_K \Delta \sqrt{k_{SGS}}. \quad (2.7)$$

Thereby, C_K is a model constant and the filter length $\Delta = (\Delta_x \Delta_y \Delta_z)^{1/3}$ is given through the cubic root of the grid cell lengths Δ_x , Δ_y and Δ_z . In order to circumvent the resolution of the thin boundary layer near walls via fine grid cells, a wall function approach is used in this study. Specifically, the expression proposed by [Spalding \(1961\)](#) is incorporated:

$$y^+ = u^+ + \frac{1}{E} \left(\exp[\kappa u^+] - 1 - \kappa u^+ - \frac{1}{2} (\kappa u^+)^2 - \frac{1}{6} (\kappa u^+)^3 \right). \quad (2.8)$$

Here y^+ , u^+ , E and κ represent the dimensionless distance normal to the wall, the dimensionless velocity parallel to the wall, the damping factor and a model constant, respectively. Using a wall function also implies that bubbles are unaffected by the viscous boundary layer near the walls, since the velocities therein cannot be calculated. This has some implications for coalescence and break-up models as well, which are discussed below.

The SGS kinetic energy k_{SGS} due to velocity fluctuations is calculated as follows:

$$k_{SGS} = 2 \frac{C_K}{C_E} \Delta^2 \bar{\mathbf{S}}^2, \quad (2.9)$$

with the model constants C_K and C_E , where the latter has the fixed value of 1.05. This approach enables a separate calculation of $\mu_{L,SGS}$ and k_{SGS} which may be beneficial for comparison purposes ([Radl et al., 2010a](#)). Inserting Eq. (2.9) into Eq. (2.7) yields:

$$\mu_{L,SGS} = \rho_L (C_S \Delta)^2 |\bar{\mathbf{S}}|, \quad (2.10)$$

where the Smagorinsky constant is given by $C_S = (2C_K^3/C_E)^{1/4}$. Finally, the turbulent energy-dissipation rate ϵ is defined as:

$$\epsilon = \frac{C_E k_{SGS}^{3/2}}{\Delta}. \quad (2.11)$$

2.2.2 Bubble Dynamics

In the Lagrangian tracking part, each individual gas bubble is handled as a rigid sphere. It is assumed that a bubble has a constant mass which only changes due to bubble break-up and coalescence (B&C) processes. Furthermore, it is presumed that the mass is concentrated at the bubble's center, located at the position \mathbf{x}_B . The trajectory and the velocity \mathbf{u}_B of a bubble are calculated based on Newton's equation of motion:

$$\Delta \mathbf{x}_B = \mathbf{u}_B \Delta t, \quad (2.12)$$

$$\rho_G \nu_B \Delta \mathbf{u}_B = \Delta t \Sigma \mathbf{F}, \quad (2.13)$$

with the gas density ρ_G , the bubble volume $\nu_B = \pi/6 d_B^3$ and the sub-time step Δt . The net force $\Sigma \mathbf{F}$, experienced by each individual bubble in the liquid, is composed of the buoyancy force \mathbf{F}_B , the lift force \mathbf{F}_L , the drag force \mathbf{F}_D and the virtual mass force \mathbf{F}_{VM} :

$$\Sigma \mathbf{F} = \mathbf{F}_B + \mathbf{F}_L + \mathbf{F}_D + \mathbf{F}_{VM}. \quad (2.14)$$

The definitions of the forces and of the respective related closure terms are summarized in Tab. 2.1. Therein, the buoyancy force is given as sum of the pressure gradient force and the gravity force. The lift force acts perpendicular to the approaching flow direction, experienced by each bubble. For small, spherical bubbles Tomiyama (2004) suggested to use the constant value 0.5 for the lift coefficient C_L . The drag force represents the resistance, when the bubble moves relative to the liquid. Here, the model proposed by Ishii and Zuber (1979) is used for the modeling of the drag force coefficient C_D . Thereby, C_D is described through a relative simple function of the Eötvös number $E\ddot{o}$. This simple drag model restricts the simulations in this study to relatively dilute bubble swarms. However, since no alternative systematic studies

Table 2.1: Overview of the forces acting on a bubble.

Force	Closure
$\mathbf{F}_B = \nu_B (-\nabla p + \rho_G \mathbf{g})$	$C_L = 0.5$
$\mathbf{F}_L = -C_L \rho_L \nu_B (\mathbf{u}_B - \mathbf{u}_L) \times \nabla \times \mathbf{u}_L$	$C_{VM} = 0.5$
$\mathbf{F}_D = -\frac{C_D}{2} A_B \rho_L \mathbf{u}_B - \mathbf{u}_L (\mathbf{u}_B - \mathbf{u}_L)$	$C_D = \frac{2}{3} E\ddot{o}^{1/2}$
$\mathbf{F}_{VM} = -C_{VM} \rho_L \nu_B \left(\frac{D_B \mathbf{u}_B}{D_B t} - \frac{D_L \mathbf{u}_L}{D_L t} \right)$	$E\ddot{o} = \frac{(\rho_L - \rho_G) g d_B^2}{\sigma}$

on the effect of alternative drag models were found, there is no reason for picking more sophisticated models (e.g. that of [Gillissen et al., 2011](#)) instead the one used in the present work. Finally, the virtual mass force expresses the acceleration resistance due to a thin liquid layer moving in front of the bubbles. For low gas volume fractions, the virtual mass coefficient C_{VM} has the constant value 0.5 ([Delnoij et al., 1997](#)).

2.2.3 Interphase Coupling

[Deen et al. \(2004\)](#) found that the liquid properties can be calculated grid independently at the bubble position \mathbf{x}_B by using the fourth-order polynomial clipping function ω :

$$\omega = \frac{15}{16} \left[\frac{(\mathbf{x} - \mathbf{x}_B)^4}{n^5} - 2 \frac{(\mathbf{x} - \mathbf{x}_B)^2}{n^3} + \frac{1}{n} \right] \quad \text{with } |\mathbf{x} - \mathbf{x}_B| \leq n, \quad (2.15)$$

where $2n$ is the width of the mapping window and \mathbf{x} is the position of the neighboring grid node. The influence of the bubble b on a certain cell j is then given through the integral $\int_{\Omega_j} \omega d\Omega$ (see [Darmana et al., 2006](#)). The gas volume fraction for a cell of volume v_{cell} is calculated through:

$$\alpha_G = \frac{1}{v_{cell}} \sum_{\forall \text{ bubbles}} v_{B,b} \int_{\Omega_j} \omega d\Omega. \quad (2.16)$$

The Euler-to-Lagrange interpolation is necessary for the calculation of the forces acting on a bubble. Therefore, the liquid quantities Ψ , e.g. the liquid velocity, have to be known at the bubble's position. Then, a liquid quantity ψ at the bubble position is calculated as follows:

$$\psi = \sum_{\forall \text{ cells}} \Psi \int_{\Omega_j} \omega d\Omega. \quad (2.17)$$

Finally, the volume-specific interphase momentum transfer rate Φ , the liquid of a grid cell experiences in the presence of the bubbles, is given for the Lagrange-to-Euler coupling as:

$$\Phi = -\frac{1}{v_{cell}} \sum_{\forall \text{ bubbles}} \phi_b \int_{\Omega_j} \omega d\Omega, \quad (2.18)$$

where $\phi_b = -\Sigma \mathbf{F}$ is the force acting on the liquid due to the presence of a bubble b in the respective computational cell.

2.2.4 Break-up and Coalescence Models

The population balance equations (PBE) for bubbly flow describes the spatial and temporal evolution of the bubble population in a system. Thereby, the break-up kernel function $r^B(\nu, \nu')$ determines the number fraction of daughter bubbles of volume ν' which are formed through break-up of bubbles of volume ν per time and per volume. The kernel function is given by the product of the break-up frequency $\varpi^B(\nu)$ and the corresponding daughter bubble size distribution (BSD) $\beta^B(\nu, \nu')$:

$$r^B(\nu, \nu') = \varpi^B(\nu) \beta^B(\nu, \nu'). \quad (2.19)$$

In the literature, the dimensionless daughter BSD $\beta^B(I, f_\nu)$ is often used instead of $\beta^B(\nu, \nu')$. Both distributions are related to each other through $\beta^B(I, f_\nu) = \nu \beta^B(\nu, \nu')$ with $f_\nu = \nu'/\nu$. Similarly, the coalescence kernel function $r^C(\nu, \nu')$ predicts the number fraction of bubbles of volume ν which coalesce with bubbles of volume ν' per time and per volume. Furthermore, this kernel function is the product of the coalescence rate $r^{C*}(\nu, \nu')$ and the coalescence efficiency $P^C(\nu, \nu')$:

$$r^C(\nu, \nu') = r^{C*}(\nu, \nu') P^C(\nu, \nu'). \quad (2.20)$$

In this work, the models derived from [Coulaloglou and Tavlarides \(1977\)](#) and from [Lee et al. \(1987a, 1987b\)](#) are investigated, which are presented in the next two sections. Fig. 2.1 shows the characteristics of these models regarding $\varpi^B(\nu)$, $\beta^B(I, f_\nu)$ and $P^C(\nu, \nu')$: Both models have significant quantitative, and in case of $P^C(\nu, \nu')$ even qualitative, different features.

Model Proposed by Coulaloglou and Tavlarides (C&T)

C&T derived a film drainage model, assuming that two colliding bubbles are going to coalesce if their contact time $\bar{t}_{contact}$ exceeds the drainage time $t_{drainage}$ of the liquid film between them. Specifically, they proposed the following exponential relation for the coalescence probability:

$$P^C(\nu, \nu') = \exp\left[-\frac{t_{drainage}}{\bar{t}_{contact}}\right]. \quad (2.21)$$

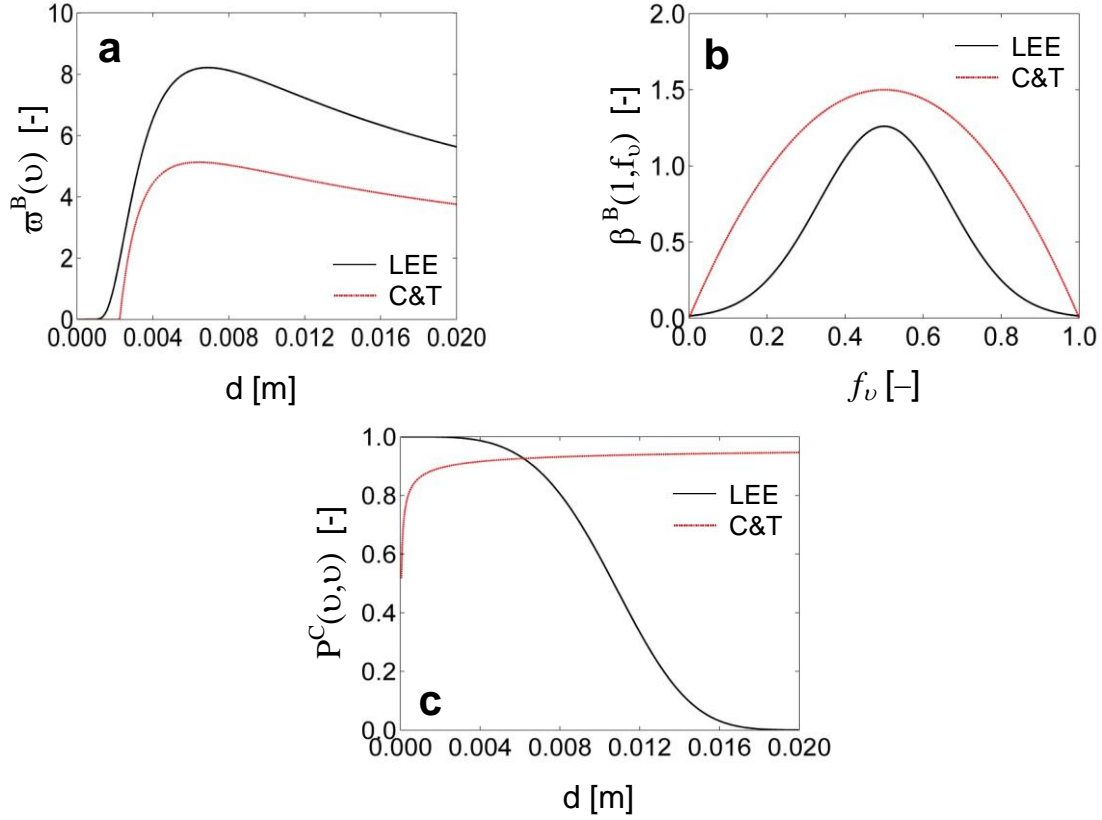


Figure 2.1: Characteristics of (a) the break-up frequency $\varpi^B(\nu)$, (b) the dimensionless daughter BSD $\beta^B(1, f_b)$ and (c) the coalescence efficiency $P^C(\nu, \nu)$ for two equal-sized bubbles ($\epsilon = 0.1 \text{ m}^2 \cdot \text{s}^{-3}$).

For two bubbles of diameters d_1 and d_2 , they assumed that t_{drainage} is equal to the time for viscous thinning (Chappellear, 1961):

$$t_{\text{drainage}} = C_{\text{COU.C}} \frac{\mu_L \rho_L d_{\text{eq}}^4}{16\sigma^2} \left(\frac{1}{h_f^2} - \frac{1}{h_i^2} \right) \epsilon^{2/3} (d_1 + d_2)^{2/3}, \quad (2.22)$$

with the surface tension σ , the equivalent bubble diameter $d_{\text{eq}} = 2/(1/d_1 + 1/d_2)^{-1}$, the initial h_i and the critical h_f film thickness before rupture. Experimental investigations of air-water systems suggest the values $h_i = 10^{-4} \text{ m}$ (Kirkpatrick and Locket, 1974) and $h_f = 10^{-8} \text{ m}$ (Kim and Lee, 1987). For \bar{t}_{contact} , C&T used the dimensional analysis from Levich (1962): Based on the theory of isotropic turbulence, two bubbles will stay together in a turbulent flow, as long as they are not hit by an eddy of size $\lambda = d_1 + d_2$:

$$\bar{t}_{\text{contact}} = \epsilon^{-1/3} (d_1 + d_2)^{2/3}. \quad (2.23)$$

Furthermore, they derived a break-up frequency $\varpi^B(\nu)$, assuming that an eddy transmits its

entire energy to a bubble during an eddy-bubble collision, which stimulates the bubble to oscillate. A bubble is going to break up into two daughter bubbles if the transmitted energy exceeds its critical surface energy. Supposing that the energy distribution of eddies follows a normal distribution, $\varpi^B(\nu)$ is given by:

$$\varpi^B(\nu) = C_{COU,B1} \left(\frac{\epsilon}{d^2} \right)^{1/3} \exp \left[-\frac{C_{COU,B2} \sigma}{\rho_G \epsilon^{2/3} d^{5/3}} \right]. \quad (2.24)$$

For the daughter BSD $\beta^B(1, f_\nu)$, they assumed a normal distribution around $\nu/2$ and determined the values for the mean and the variance experimentally, so that 99.6 % of the investigated daughter bubbles lie within the distribution:

$$\beta^B(1, f_\nu) = 1.26 \exp[-4.5(2f_\nu - 1)^2]. \quad (2.25)$$

Model Proposed by Lee et al. (LEE)

LEE used the film drainage model as described in Eqs. (2.21) and (2.23). In their model, $t_{drainage}$ is given as the sum of the time for viscous thinning and the time for film rupture:

$$t_{drainage} = C_{LEE,C} \left(\frac{R_d}{4} \left(\frac{\rho_L d_{eq}}{2\sigma} \right)^{1/2} \ln \left[\frac{h_i}{h_f} \right] + \frac{24\pi^2 M \sigma \mu_L h_f^5}{A_h^2} \right), \quad (2.26)$$

with the liquid film radius R_d , the surface immobility parameter M and the Hamaker constant A_h . As value for M , they suggested 0.034 and reported the following literature values for $R_d = 10^{-4}$ m and $A_h = 10^{-20}$ J. The film rupture term in Eq. (2.26) does not depend on the bubble radii and thus, an opposite characteristic of $P^C(\nu, \nu')$ is obtained compared with the model from C&T, as can be seen in Fig. 2.1(c).

Regarding the break-up frequency $\varpi^B(\nu)$, their model is based on the same considerations as the one from C&T. The difference here is that the energy distribution of the arriving eddies follows a Maxwell distribution:

$$\varpi^B(\nu) = C_{LEE,B1} \left(\frac{\epsilon}{d^2} \right)^{1/3} \left(1 - \frac{1}{d} \int_0^d D_3 \left[\frac{C_{LEE,B2} \sigma d^2}{\rho_L \epsilon^{2/3} \lambda^{1/3}} \right] d\lambda \right), \quad (2.27)$$

where $D_3(x) = 1 - \Gamma(3/2, x/2) / \Gamma(3/2)$ is the cumulative chi-square distribution with three degrees

of freedom, and $\Gamma(a,x)$ and $\Gamma(a)$ are the incomplete and complete gamma functions, respectively. Further, LEE presumed that $\beta^B(I,f_v)$ has the shape of a beta distribution:

$$\beta^B(1, f_v) = \frac{\Gamma(4)}{\Gamma(2)\Gamma(2)} f_v (1-f_v). \quad (2.28)$$

2.2.5 Numerical Implementation

At the beginning of the Lagrangian tracking, bubbles with fixed uniform sizes are injected into the domain and the bubble properties are updated. Afterwards, all bubbles are checked for break-up, where a uniformly distributed random number ξ with $0 \leq \xi \leq 1$ is generated for each bubble. A bubble with volume v breaks up during the fluid time step Δt_{fluid} if the condition $\xi < \varpi^B(v)\Delta t_{fluid}$ is satisfied. If the break-up condition is true, the daughter bubble volumes $v f_v$ and $v(1-f_v)$ are calculated next. The inverse transform method $[\beta^B(I, f_v)]^{-1}$ is used to obtain samples for f_v that follow the desired $\beta^B(I, f_v)$ -distribution (Gentle, 2003). Thereafter, the daughter bubbles are positioned randomly around the mass center of the mother bubble. The detailed calculation parameters of the daughter bubble generation algorithm are summarized in Tab. 2.2.

Table 2.2: Bubble parameters after coalescence of two colliding bubbles (a, b) to form a merged bubble (c) or after break-up to form the daughter bubbles (a, b) from the mother bubble (c). Here, ξ_1, ξ_2, ξ_3 are uniformly distributed random numbers with $0 \leq \xi_1, \xi_2, \xi_3 \leq 1$ and ε is a small quantity.

Parameter	Coalescence	Break-up	Closure
Diameter d	$d_c = (d_a^3 + d_b^3)^{1/3}$	$d_a = d_c f_v^{1/3}$ $d_b = d_c (1-f_v)^{1/3}$	$m_{ab} = m_a + m_b$ $\delta = ((d_a + d_b)/2 + \varepsilon) \mathbf{n}$
Mass m	$m_c = m_a + m_b$	$m_a = m_c f_v$ $m_b = m_c (1-f_v)$	$\mathbf{n} = \frac{(\xi_1, \xi_2, \xi_3)}{[(\xi_1, \xi_2, \xi_3)]}$
Position \mathbf{p}	$\mathbf{p}_c = (m_a \mathbf{p}_a + m_b \mathbf{p}_b) / m_{ab}$	$\mathbf{p}_a = \mathbf{p}_c + m_b / m_{ab} \delta$ $\mathbf{p}_b = \mathbf{p}_c - m_a / m_{ab} \delta$	
Velocity \mathbf{u}	$\mathbf{u}_c = (m_a \mathbf{u}_a + m_b \mathbf{u}_b) / m_{ab}$	$\mathbf{u}_a = \mathbf{u}_c + \varepsilon \mathbf{n}$ $\mathbf{u}_b = \mathbf{u}_c - \varepsilon \mathbf{n}$	

Due to the effect of walls on the turbulent flow field of the liquid phase (i.e. the formation of a boundary layer where velocity fluctuations become anisotropic), the sub-models for coalescence and break-up are expected to give unrealistic results. However, no suitable model was found in literature that was validated for the prediction of near-wall coalescence and break-up. Therefore, break-up is restricted to appear only in computational cells that are not adjacent to walls, by assuming that bubbles are unaffected by the viscous boundary layer. Consequently, this fact limits the relevance of this study to flows in which the bubble concentration near walls is small and bubble-wall interactions are unimportant. Both limitations are unproblematic for the simulation setup which is described in the next chapter. $P^C(\nu, \nu')$ determines if two colliding bubbles coalesce or bounce: Two colliding bubbles coalesce if $P^C(\nu, \nu') < \xi$, otherwise they will bounce off each other. The changes of the bubble properties due to coalescence and bouncing are listed in Tabs. 2.2 and 2.3.

Table 2.3: The tangential velocity components \mathbf{u}^{\parallel} , normal velocity components \mathbf{u}^{\perp} and the positions \mathbf{p} for two bubbles (a, b) before and after ($*$) bouncing or overlap handling. Here, \mathcal{O} is the overlap of the bubbles, \mathbf{n} is the unit vector of the bubble's mass center connection line and ε is a small quantity.

	Bouncing	Overlap handling	Closure
Before	$\mathbf{u}_a^{\parallel}, \mathbf{u}_b^{\parallel}$ $\mathbf{u}_a^{\perp}, \mathbf{u}_b^{\perp}$	$\mathbf{p}_a, \mathbf{p}_b$	$\mathcal{O} = (d_a + d_b)/2 - \mathbf{p}_a - \mathbf{p}_b $
After	$\mathbf{u}_a^{\parallel*} = \mathbf{u}_a^{\parallel}$ $\mathbf{u}_b^{\parallel*} = \mathbf{u}_b^{\parallel}$	$\mathbf{p}_a^* = \mathbf{p}_a + m_a/m_{ab}(\mathcal{O} + \varepsilon) \mathbf{n}$ $\mathbf{p}_b^* = \mathbf{p}_b - m_b/m_{ab}(\mathcal{O} + \varepsilon) \mathbf{n}$	$\mathbf{n} = \frac{\mathbf{p}_a - \mathbf{p}_b}{ \mathbf{p}_a - \mathbf{p}_b }$
	$\mathbf{u}_a^{\perp*} = 2(m_a \mathbf{u}_a^{\perp} + m_b \mathbf{u}_b^{\perp})/m_{ab} - \mathbf{u}_a^{\perp}$ $\mathbf{u}_b^{\perp*} = 2(m_a \mathbf{u}_a^{\perp} + m_b \mathbf{u}_b^{\perp})/m_{ab} - \mathbf{u}_b^{\perp}$		$m_{ab} = m_a + m_b$ $\mathbf{u} = \mathbf{u}^{\perp} + \mathbf{u}^{\parallel}$

Coalescence and break-up inevitably leads to a polydisperse bubble ensemble, and this has some important consequences:

- (i) Models for drag and lift have been developed for monodisperse, relatively dilute systems. Their use in polydisperse bubble flows has not been rigorously validated, and dedicated models for polydisperse systems are in the early stages of development. As already discussed, a rather simple model for drag and lift is used in this work, which neglects, e.g. wake effects that large bubbles have on small ones.
- (ii) The relative resolution (i.e. the spacing of the computational grid to the bubble

diameter) is different for individual bubbles. Thus, while for large bubbles the flow field might appear “well resolved”, non-resolved liquid phase velocity fluctuations might be important for small bubbles. As there is no consensus on how liquid phase velocity fluctuations affect bubble motion in polydisperse systems, no model is used for these effects.

- (iii) Some bubbles with diameters in the range of the cell lengths are formed for a short-time through coalescence. Thus, the ratio of bubble diameter to computational grid size can be larger than unity, which comes into conflict with the used modified version of the Navier-Stokes equation. Since a local adaptation of the grid size is unpractical, the local liquid volume fraction is limited via:

$$\alpha_L = \max[1 - \alpha_G, 0.05]. \quad (2.29)$$

- (iv) B&C processes lead to overlaps of the bubbles, because the latter are assumed to be spherical. In reality, bubbles would deform, repel each other, and start to move relative to each other. Here, bubble overlap is handled by displacing the bubbles around their mass centers (see Tab. 2.3). This procedure has to be repeated until all overlaps in the domain are removed.

After the Lagrangian tracking for Δt_{fluid} is completed, the values for α_L and Φ are calculated and finally, the filtered Navier-Stokes equations are solved.

2.2.6 The “Deen Case”

In this study, the bubble column (BC) experiment performed by [Deen et al. \(2001a, 2001b\)](#), and hereafter called the Deen case, is used as reference case for validating the algorithm. Their three-dimensional rectangular BC had a cross-section area of $0.15 \times 0.15 \text{ m}^2$ and was filled with water up to a height of 0.45 m , as shown in Fig. 2.2(a). Air was injected through a perforated plate with a superficial velocity of $4.9 \text{ mm} \cdot \text{s}^{-1}$, which corresponded to a gassing rate of ca. $1.1 \times 10^{-4} \text{ m}^3 \cdot \text{s}^{-1}$. The plate contained 7×7 circular shaped holes at a square pitch of 6.25 mm , as shown in Fig. 2.2(b). The resulting injected bubbles had an initial mean bubble diameter of $d_B = 4 \text{ mm}$. [Hansen \(2009\)](#) used the Deen case for his investigations of the BSD in the column. By applying the interferometric particle imaging technique (IPI) between the heights of 0.20 m and 0.30 m , he observed the BSD shown in Fig. 2.2(c) with bubble diameters between $0.5 \text{ mm} < d_B < 10.6 \text{ mm}$. Finally, [Bai \(2010\)](#) measured the overall gas volume fraction $\alpha_{G,overall}$ to be 1.6% for the Deen case.

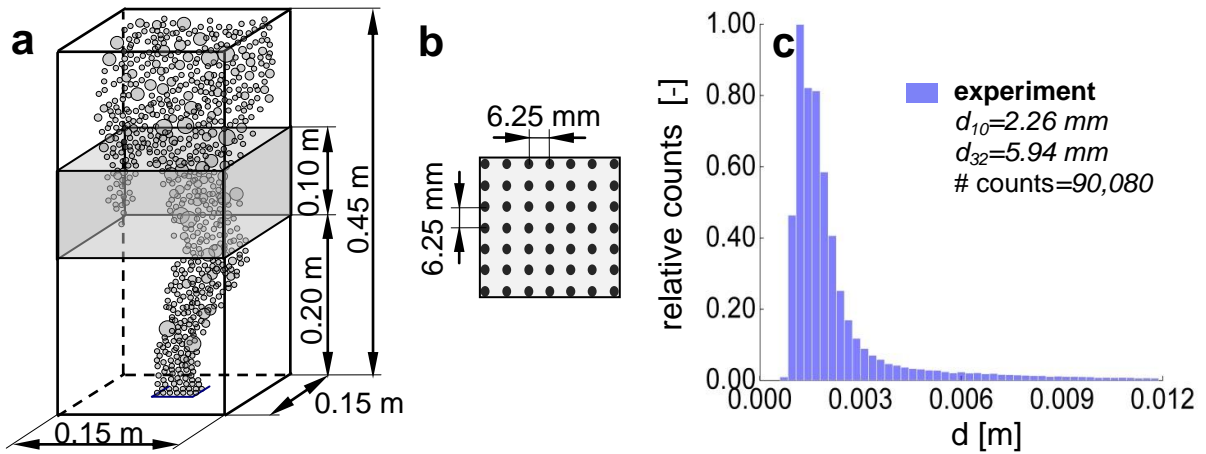


Figure 2.2: Schematic view of (a) the computational model, (b) the perforated plate and (c) the BSD observed by Hansen (2009). In (a), the grey marked volume indicates the region in which Hansen experimentally analyzed the BSD.

2.2.7 Simulation Setup

The Deen case is converted into a computational model consisting of $15 \times 15 \times 45$ cubic cells with constant cell lengths of 10 mm. Second-order accurate numerical schemes are used in space (for the convection and diffusion terms) and time to avoid excessive numerical diffusion. The no-slip condition and the ideally elastic bounce-back condition (for the bubbles) are applied to each wall for the liquid. For the top face (outlet), the free-slip condition has been used for the liquid. Air bubbles with a uniform diameter of 4 mm are injected with a speed of 0.269 $m \cdot s^{-1}$ at the bottom of the column. The bubbles rise in the liquid, and once a bubble reaches the top plane (outlet), it is removed from the domain. The continuous feeding and removal of bubbles in the BC causes a temporal variation of the liquid fill level. Due to the fact that a fixed grid is used for modeling, numerical instabilities would arise during the simulation. These instabilities are avoided by calculating the mean liquid volume fraction $\alpha_{L,mean}$ from the local α_L through volume averaging as described by Radl et al. (2010a):

$$\frac{\partial \alpha_L}{\partial t} + \nabla \cdot (\alpha_L \bar{\mathbf{u}}_L) = \frac{\partial \alpha_{L,mean}}{\partial t}. \quad (2.30)$$

This technique allows the resolution of local changes of α_L on one hand and avoids numerical problems on the other.

All simulations start with a stagnant liquid and proceed with a time step for the liquid phase

of 1 ms for 180 s , while the bubbles are tracked with a sub-time step of $\Delta t=0.1\text{ ms}$. These settings led to negligible differences compared to simulations with smaller time steps, which is also confirmed by literature data ([Darmana et al., 2005](#)).

2.3 Results and Discussion

The cases simulated in this study are summarized in Tab. 2.4. The reported results for liquid flow and bubble motion were obtained through long-term averaging (LTA) or long-term counting (LTC), starting after 20 s to allow the flow to develop. If not mentioned otherwise, both LTA and LTC ended after 180 s.

Table 2.4: Overview of the different simulation cases. Therein, C_S , C_C and C_B denote the Smagorinsky constant, as well as the model constants for bubble coalescence and break-up, respectively.

Case	C_S	Break-up and coalescence	C_C	C_{B1}	C_{B2}
0	0.10	none (monodisperse, $d_B=4$ mm)	–	–	–
1	0.11				
2	0.10	Coulaloglou and Tavlarides	3.0×10^{-8}	1.8	1.0×10^{-4}
3	0.11				
4	0.10	Lee et al.	8.0	2.0	3.0×10^{-2}
5	0.11				

Each of the simulations was performed on a single core of a QX9650 Intel processor. During the simulations approximately 4,500, 10,000 and 5,500 bubbles were moved at every time step within the cases 0, 2 and 4, respectively. A typical simulation time for one case amounted to be between 4 and 6 days.

2.3.1 Monodisperse Bubbles (Standard Case)

A series of instantaneous snapshots in Fig. 2.3(a) shows the development of the bubble plume for the standard case (case 0) at the times 0.5 s, 1 s, 20 s, 40 s and 80 s. Soon after the bubbles are injected into the quiescent liquid, the ascending bubbles form a plume with the typical mushroom-like shape. Later in time, when the flow in the BC is fully developed, the plume begins to oscillate, which was also observed by Deen et al. (2001a) in their experiments. In order to compare the simulation results with the particle image velocimetry (PIV) data of Deen, the liquid flow field is LTA at certain positions in the column. Here, the length of the averaging period needs to be chosen long enough in order to achieve statistically meaningful results, in which the convergence of the velocity profiles serves as evaluation criterion.

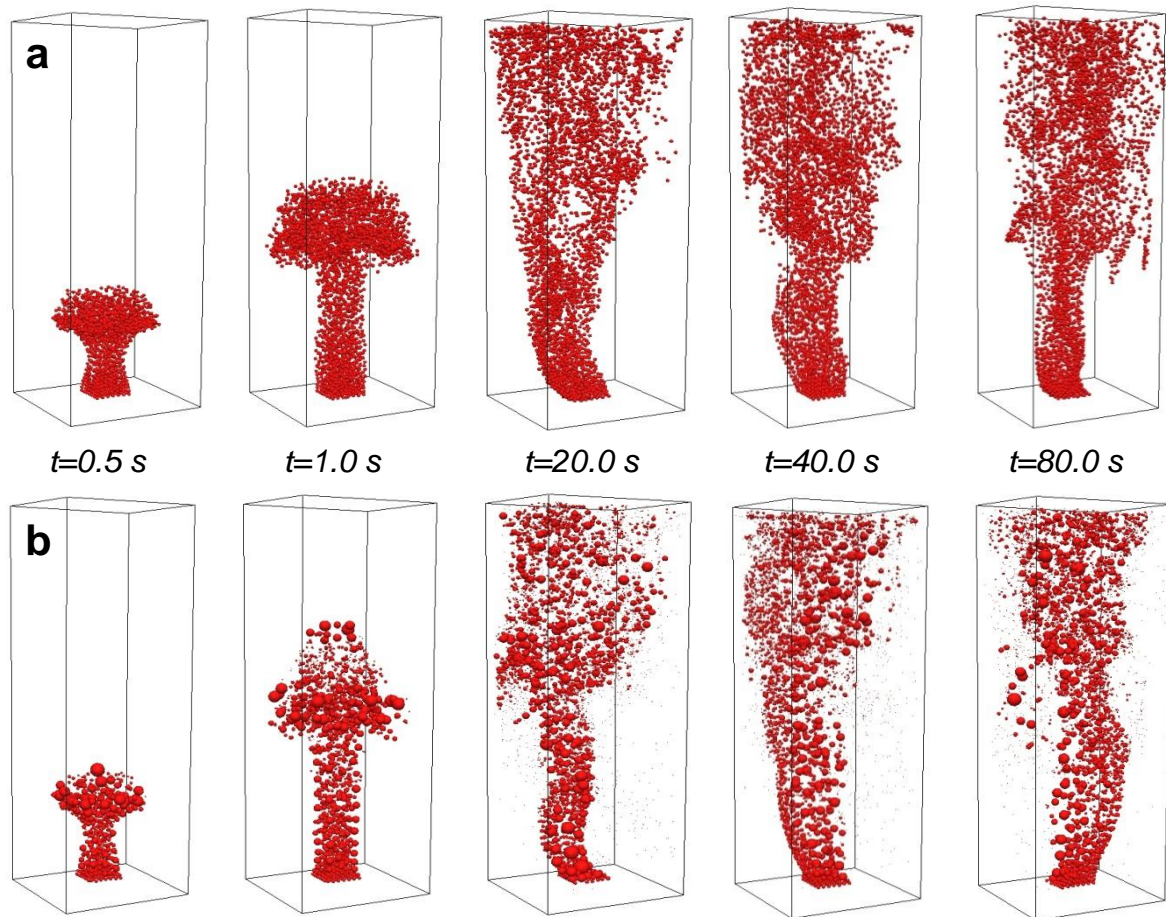


Figure 2.3: Snapshots of the evolving bubble plume with uniform bubble size (a, case 0) and with B&C using the model of Lee et al. (b, case 4).

A comparison of the velocity profiles in Fig. 2.4(a) indicates that the velocities converge after a simulation time of approximately 120 s . Furthermore, it can be seen that the average liquid velocity profile of the model and the experimental results from Deen show excellent agreement. The average liquid velocity near the center of the column is slightly under predicted. The axial and the lateral velocity fluctuation (see Figs. 2.4(b) and (c)) give some impression about the chaotic features of the flow field: As can be seen, the axial component is in the same order of magnitude as the mean velocity. A comparison with the experimental results indicates that the qualitative behavior, i.e. the twin-peaked shape, and the quantitative behavior of the flow field, are well capture with this model, even with equal sized bubbles.

2.3.2 Polydisperse Bubble Populations

By using the BSD measured by Hansen for the Deen case and shown in Fig. 2.2(c), the model parameters for the C&T and LEE model were estimated. However, a perfect match between

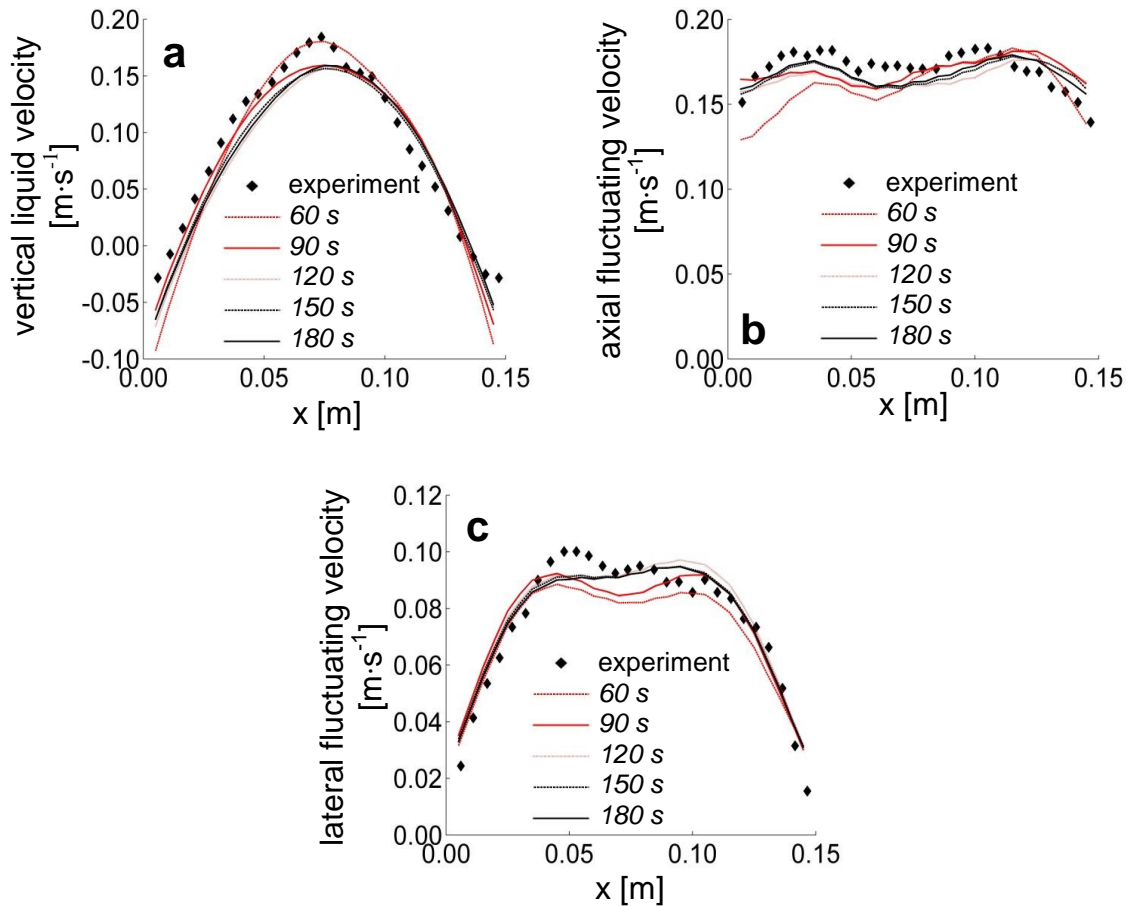


Figure 2.4: Comparison of the simulated and experimental LTA liquid velocities (a) and the fluctuating velocity components (b,c) for the standard case (case 0) at a height of 0.255 m and a depth of 0.075 m for different averaging periods.

experimental data and the results from C&T and LEE model is difficult. Therefore, a closely match of the arithmetic mean diameter d_{10} was attempted. The Sauter mean diameter d_{32} was then computed to analyze the difference between model predictions and experiments. These mean diameters are defined as $d_{10} = \sum N_i d_i / \sum N_i$ and $d_{32} = \sum N_i d_i^3 / \sum N_i d_i^2$. The model parameters, ultimately used for the simulation of the cases 2, 3, 4 and 5 (non-uniform BSDs) are summarized in Tab. 2.4.

Fig. 2.5(a) shows the BSD obtained with the model of C&T (case 2). A comparison of the LTC and Hansen's BSD points out, that both distributions possess a positive skewness and the results for d_{10} could be nicely matched (model: 2.28 mm, experiment: 2.26 mm). However, the BSD of Hansen is leptokurtic (i.e. sharp peak around the mean and broad tails) and contains a significant number of bubbles with diameters larger than 9 mm. The latter fact

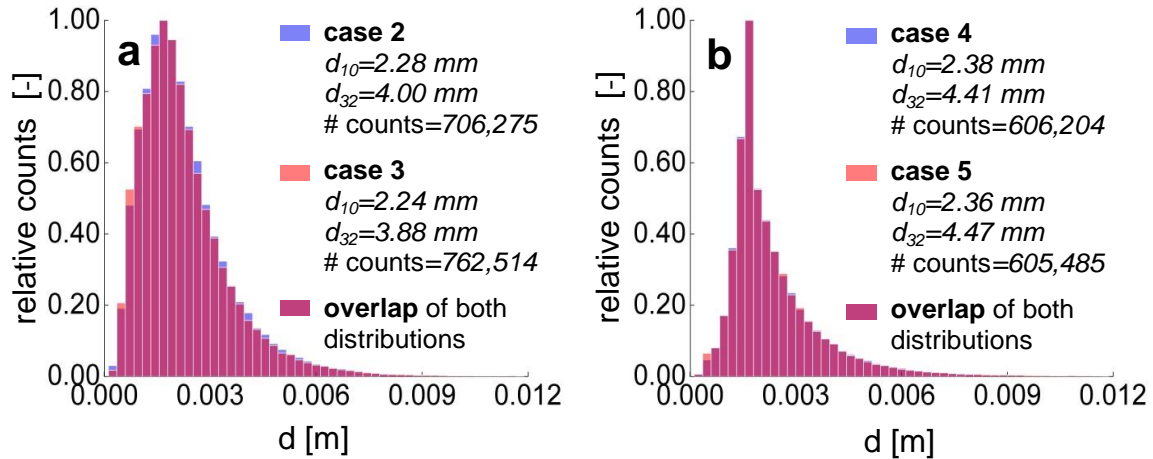


Figure 2.5: Comparison of long-term counted BSD obtained with the B&C models from Coulaloglou and Tavlarides (a) and from Lee et al. (b).

explains the difference of the d_{32} values. A similar characteristic is seen in the computed BSD for the model of LEE (case 4). The BSD is illustrated in Fig. 2.5(b) and shows a positive skewness, nearly no bubbles with diameters greater than 9 mm. Again, the $d_{10}=2.38$ mm is in good agreement with Hansen's BSD, as well. However, the BSD calculated with the LEE model is more leptokurtic than the one measured by Hansen. An evaluation of the simulation results with respect to the size range of the observed bubble diameters reveals the following minima and maxima: With the model of C&T, bubbles between 0.07 mm $< d_B < 19.6$ mm are observed, while bubbles between 0.12 mm $< d_B < 18.6$ mm are predicted with the model of LEE. The evolution of the bubble plume, including break-up and coalescence (B&C) for the LEE model (case 4), is shown as a series of snapshots in Fig. 2.3(b). Again, the typical mushroom-like shape can be observed shortly after the start of the simulation. In the second picture at $t=1$ s, it can be seen that coalescence dominates in the region around the inlet. The relative distributions of the B&C events in a two-dimensional cut through the computational domain are represented in Figs. 2.6(a) and (b).

As can be seen, the bubbles mainly coalesce above the sparger while break-up occurs over the entire height of the BC. Concerning the coalescence processes of the two models, 27 % of the bubble-bubble collision in case 2 lead to coalescence while only 18 % of the collisions in case 4 lead to coalescence. This circumstance results from the fact that the $P^C(v, v')$ values for the C&T model are very high for almost all bubble radii, while the $P^C(v, v')$ function of the LEE model tends towards zero for larger bubble radii (see Fig. 2.1c). In both break-up

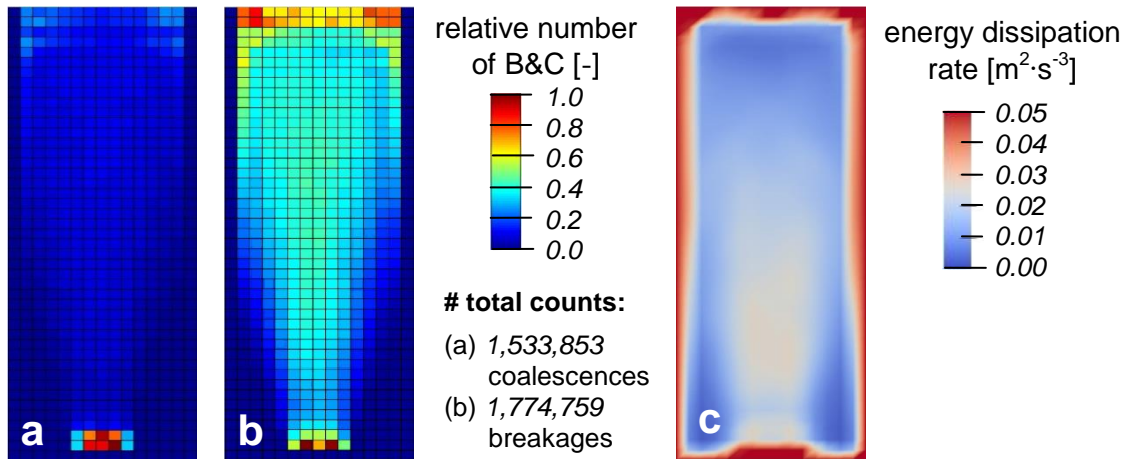


Figure 2.6: LTC spatial distribution of coalescence (a) and break-up events (b) with the model from Lee et al. (case 4). The LTA of the energy-dissipation rate in the mid-depth plane is shown in (c).

models, the local energy-dissipation rate ϵ is, apart from the bubble diameter, the most important parameter that dictates whether break-ups will occur or not. Fig. 2.6(c) shows the LTA ϵ -field in the mid-depth plane of the BC.

As mentioned before, break-up is not considered in the region near the wall thus, bubbles are not allowed to break-up in these regions. A comparison of the Figs. 2.6(b) and (c) reveals that higher break-up rates occur in the region close to the top outlet. This is due to the high ϵ -values of about $0.05 \text{ m}^2 \cdot \text{s}^{-3}$ in this region, as well as the comparably large size of the bubbles in this region.

2.3.3 Sauter Mean Diameter and Gas Volume Fraction

For spherical bubbles, the specific interfacial area a is given through the relation:

$$a = \frac{6\alpha_G}{d_{32}}. \quad (2.31)$$

The LTA properties of both parameters over the column height are shown in Fig. 2.7(a) for the cases 0, 2 and 4. In this diagram, it can be seen that the local Sauter mean diameters $d_{32,local}$ increases up to a maximum at a height of 0.05 m and then decreases continuously to about 4 mm at the top of the BC. The maxima at 0.05 m have values of 6.0 mm and 6.5 mm , for the model from C&T and from LEE, respectively.

Simultaneously, the local gas volume fraction $\alpha_{G,local}$ drops rapidly from the local maximum at

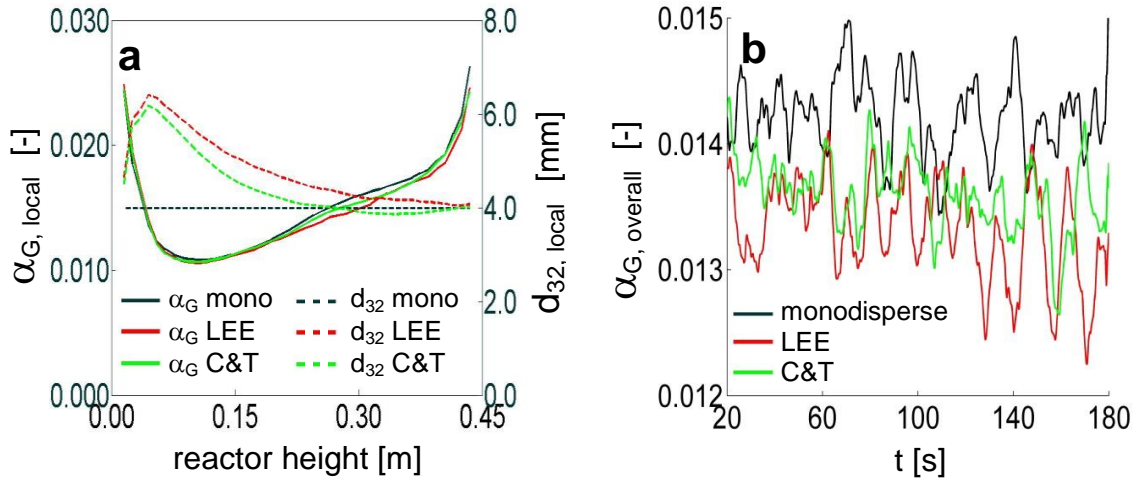


Figure 2.7: Axial profiles of the simulated LTA local gas volume fraction $\alpha_{G,local}$ and the local Sauter mean diameter $d_{32,local}$ (a). The temporal evolution of the overall gas volume fraction $\alpha_{G,overall}$ is shown for the cases 0, 2 and 4 in (b).

the inlet to a minimum value of approximately 1.1 % at a reactor height of 0.10 m. Then, $\alpha_{G,local}$ continuously increases to 2.5 % at the top of the reactor. Surprisingly, the $\alpha_{G,local}$ values are the same for all models up to approximately 0.2 m. Above this level, the monodisperse case results in marginally higher $\alpha_{G,local}$ values, while the results of the LEE model give insignificantly lower predictions. This behavior is also mirrored in the temporal evolution of the overall gas volume fraction $\alpha_{G,overall}$, as shown in Fig. 2.7(b). The LTA $\alpha_{G,overall}$ values of 1.4 %, 1.4 % and 1.3 %, for the cases 0, 2 and 4, respectively, show good agreement with the experimentally measured value of 1.6 % from Bai (2010). Consequently, the local interfacial area a_{local} in the reactor follows the trend of the $\alpha_{G,local}$ in a similar way, in case of the monodisperse case even exactly. Interestingly, for non-uniform BSDs (in case a coalescence and break-up model is employed) the local interfacial area is significantly (ca. 35 %) smaller compared to the monodisperse case. However, the two different coalescence and break-up models give similar results.

Next the influence of B&C on the hydrodynamics of the bubbly flow is investigated. A comparison of the liquid flow field for monodisperse and polydisperse BSDs is shown in Fig. 2.8. As can be seen, cases 0, 2 and 4 have similar characteristics regarding the average and the fluctuating velocities. Additionally, the velocity profiles also show good quantitative, as well as good qualitative agreements, with the experimentally obtained ones. The good agreement between the average velocities for all three cases may be attributed to the used drag

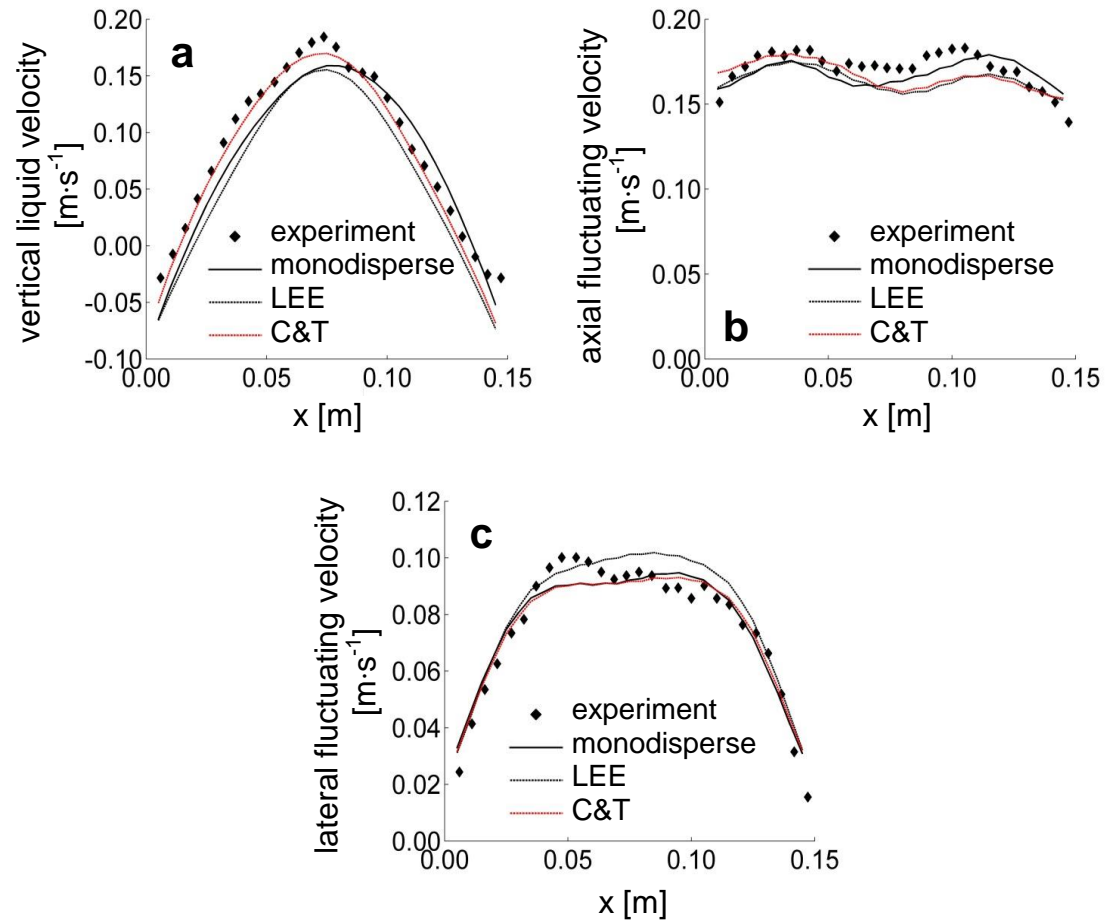


Figure 2.8: Comparison of the simulated and experimental LTA liquid velocities (a) and the fluctuating velocity components (b,c) for the uniform BSD (case 0) and with B&C (case 2 and 4) for $C_S=0.10$ at a height of 0.255 m and a depth of 0.075 m.

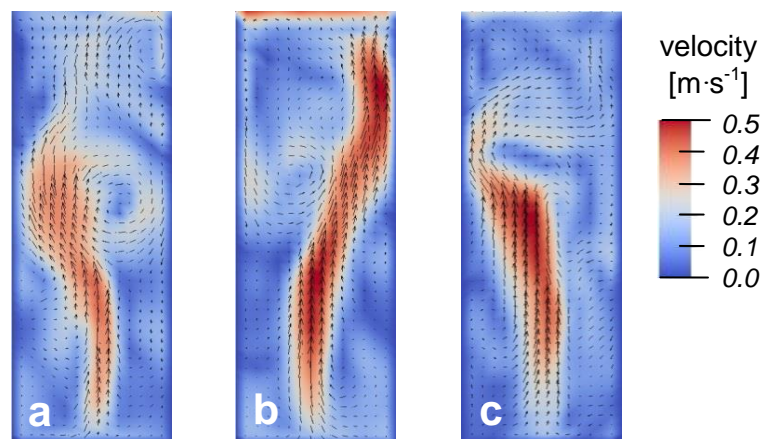


Figure 2.9: Snapshots of the instantaneous liquid velocity after 100 s in the mid-depth plane for the uniform BSD (a, case 0) and with B&C using the models of Lee et al. (b, case 2) and Coualoglou and Tavlarides (c, case 4).

model which results in the same rise velocities independent of the bubble diameters. Fig. 2.9 shows instantaneous snapshots of the velocity field in the mid-depth plane at a simulation time of 100 s . Several small and large vortical structures can be seen in these pictures for all three cases.

2.3.4 Influence of the Smagorinsky Constant

Finally, the influence of a variation of the Smagorinsky constant on the bubbly flow and on the BSD is investigated. Therefore, the C_S was increased to the value of 0.11 in the cases 1, 3 and 5. A comparison of the velocity profiles in Figs. 2.8 and 2.10 reveals that the C_S change has only a marginal impact on all cases. The main effect that can be noticed is a reduction of the axial fluctuation velocity in case 1. Consequently, the BSDs of both B&C models only changes slightly, as shown in Fig. 2.5 The d_{10} values of the new BSDs are 2.24 mm and 2.36 mm , for the models from C&T and from LEE, respectively.

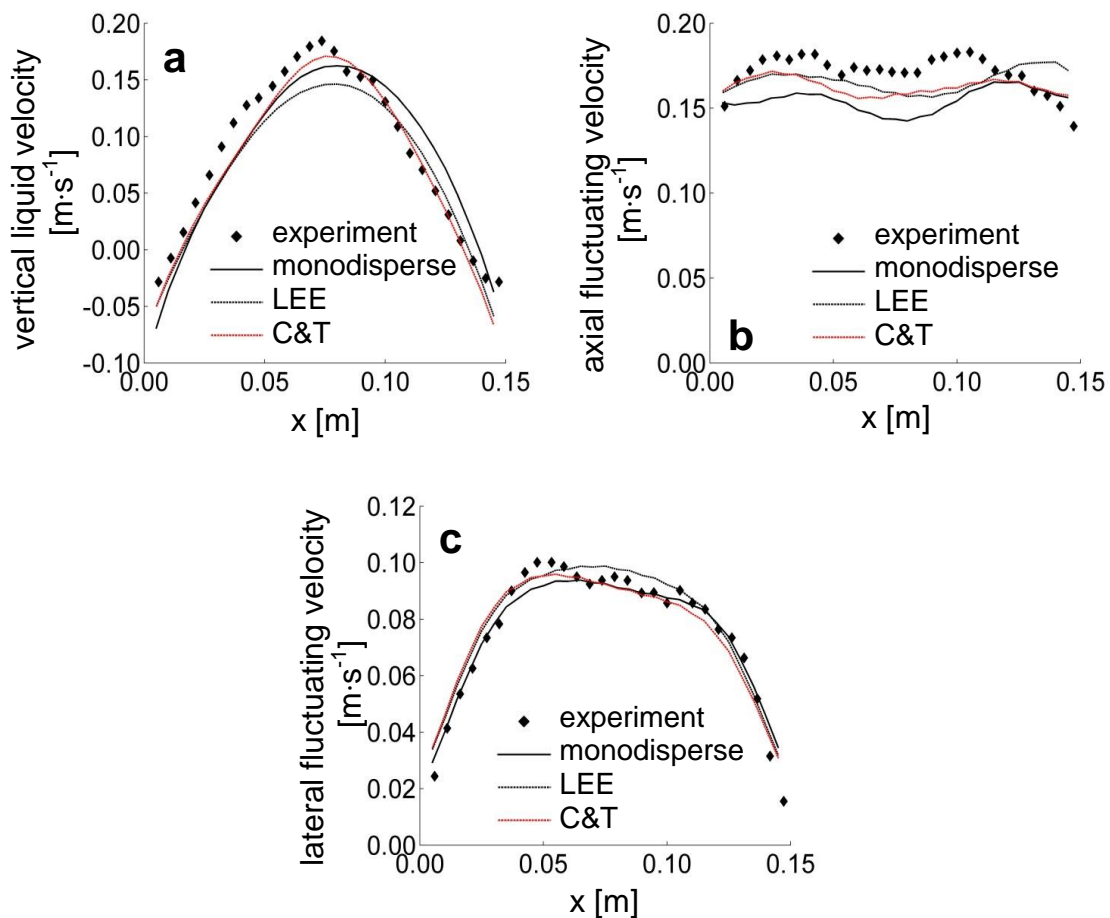


Figure 2.10: Comparison of the simulated and LTA liquid velocities (a) and the fluctuating velocity components (b,c) for the uniform BSD (case 1) and with B&C (case 3 and 5) for $C_S=0.11$ at a height of 0.255 m and a depth of 0.075 m .

2.4 Summary and Conclusions

In this study, gas-liquid flow in a three-dimensional rectangular bubble column (BC) was modeled with a stochastic approach to consider break-up and coalescence. The liquid and the gas phases were modeled based on a four-way coupled, three-dimensional Euler-Lagrangian (EL) approach. Thereby, the bubble break-up and coalescence (B&C) models suggested by [Lee et al. \(1987a, 1987b\)](#) (LEE) and [Coulaloglou and Tavlarides \(1977\)](#) (C&T) were applied.

A validation with the experimental results from [Deen et al. \(2001a, 2001b\)](#) and [Bai \(2010\)](#) showed good agreement regarding the long-term averaged (LTA) mean and fluctuating liquid velocity components, and the overall gas hold-up in the BC. With respect to the flow field and gas hold-up, both B&C models yielded results very close to that using a uniform bubble size. Both B&C models predicted a Sauter mean bubble diameter d_{32} close (within about 10%) to the one used for the simulations with a uniform bubble size. Hence, it was concluded that it is sufficient to use the Sauter mean diameter (if known *a priori*) to make correct predictions of flow and overall gas hold-up for the type of BC that was investigated in this study.

The main benefit from simulations using B&C models is that they seem to better predict the local interfacial areas, especially in the lower half of the BC: coalescence occurs mainly in the region directly above the inlet, leading to a rapid increase on bubble size. Bubble break-up takes place over the whole column height. In summary, this leads to a maximum value of the Sauter mean diameter and a subsequent drop of d_{32} over the remaining height of the column.

Neither with the model of LEE nor with the model of C&T, was it possible to exactly match the experimentally determined bubble size distribution (BSD) from [Hansen \(2009\)](#). However, the agreement was good. The similar results for flow, hold-up and local Sauter mean diameter of the LEE and C&T model indicate that not only the B&C model is critical for more accurate prediction of bubbly flows. Thus, future studies are required to systematically address the effect of various sub-models (e.g. drag, lift, energy-dissipation rate) in order to refine the picture for the most appropriate model structure and parameters for simulations of these complex multiphase flows.

Notation

Latin Letters

a	specific gas-liquid interfacial area, (m^{-1})
A_h	Hamaker constant, ($\text{kg}\cdot\text{m}^2\cdot\text{s}^{-2}$)
C_C, C_{B1}, C_{B2}	break-up and coalescence model parameters, (–)
C_E, C_K	turbulence model constants, (–)
C_D	drag coefficient, (–)
C_L	lift coefficient, (–)
C_S	Smagorinsky constant, (–)
C_{VM}	virtual mass coefficient, (–)
d_B, d	bubble diameter, (m)
d_{eq}	equivalent bubble diameter, (m)
d_{10}, d_{32}	arithmetic / Sauter mean diameter, (m)
$D_3(x)$	cumulative chi-square distribution with three degrees of freedom, (–)
E	damping factor of the wall function, (–)
$E\ddot{o}$	Eötvös number, (–)
f_v	daughter bubble volume fraction, (–)
\mathbf{F}_B	buoyancy force, ($\text{kg}\cdot\text{m}^{-2}\cdot\text{s}^{-2}$)
\mathbf{F}_D	drag force, ($\text{kg}\cdot\text{m}^{-2}\cdot\text{s}^{-2}$)
\mathbf{F}_L	lift force, ($\text{kg}\cdot\text{m}^{-2}\cdot\text{s}^{-2}$)
\mathbf{F}_{VM}	virtual mass force, ($\text{kg}\cdot\text{m}^{-2}\cdot\text{s}^{-2}$)
g	gravitational acceleration, ($\text{m}\cdot\text{s}^{-2}$)
h_i, h_f	initial / critical film thickness, (m)
k_{SGS}	sub-grid kinetic energy, ($\text{m}\cdot\text{s}^{-2}$)
m	mass, (kg)
M	surface immobility parameter, (–)
\mathbf{n}	unit vector, (m)
\mathcal{O}	overlap, (m)
p	liquid pressure / filtered liquid pressure, ($\text{kg}\cdot\text{m}^{-1}\cdot\text{s}^{-2}$)
\mathbf{p}	position vector, (m)
$P^C(v, v')$	coalescence efficiency, (–)
$r^B(v, v')$	break-up rate, ($\text{m}^{-3}\cdot\text{s}^{-1}$)
$r^C(v, v'), r^{C^*}(v, v')$	coalescence rate, ($\text{m}^{-3}\cdot\text{s}^{-1}$)
R_d	liquid film radius, (m)
$\bar{\mathbf{S}}$	rate of strain, (s^{-1})
$\Delta t, \Delta t_{fluid}$	sub-time step / liquid time step, (s)
t	time, (s)
$\bar{t}_{contact}$	contact time, (s)
$t_{drainage}$	drainage time, (s)
u^+	dimensionless velocity, (–)
\mathbf{u}_L	liquid velocity, ($\text{m}\cdot\text{s}^{-1}$)
$\bar{\mathbf{u}}_L$	grid scale velocity, ($\text{m}\cdot\text{s}^{-1}$)
\mathbf{u}'_L	sub-grid scale velocity, ($\text{m}\cdot\text{s}^{-1}$)

\mathbf{u}_B	bubble velocity, ($\text{m}\cdot\text{s}^{-1}$)
$\mathbf{u}^\perp, \mathbf{u}^\parallel$	normal / tangential velocity components, ($\text{m}\cdot\text{s}^{-1}$)
\mathbf{x}, \mathbf{x}_0	position, (m)
y^+	dimensionless wall distance, (-)

Greek Letters

α_G, α_L	gas / liquid volume fraction, (-)
$\beta^B(\nu, \nu')$	daughter bubble size distribution, (m^{-3})
$\beta^B(I, f_\nu)$	dimensionless daughter bubble size distribution, (-)
$\Gamma(a), \Gamma(a, x)$	complete / incomplete gamma function, (-)
δ	vector, (m)
Δ	filter length, (m)
$\Delta_x, \Delta_y, \Delta_z$	cell length in x-, y- and z-direction, (m)
ϵ	energy-dissipation rate, ($\text{m}^2\cdot\text{s}^{-3}$)
κ	wall function model constant, (-)
λ	eddy size, (m)
μ_L	molecular dynamic viscosity, ($\text{kg}\cdot\text{m}^{-1}\cdot\text{s}^{-1}$)
$\mu_{L,EFF}$	viscosity, ($\text{kg}\cdot\text{m}^{-1}\cdot\text{s}^{-1}$)
$\mu_{L,SGS}$	turbulent viscosity, ($\text{kg}\cdot\text{m}^{-1}\cdot\text{s}^{-1}$)
ρ_G, ρ_L	gas / liquid density, ($\text{kg}\cdot\text{m}^{-3}$)
σ	surface tension, ($\text{kg}\cdot\text{s}^{-2}$)
$\tau_L, \bar{\tau}_L$	stress tensor / filtered stress tensor, ($\text{kg}\cdot\text{m}^{-1}\cdot\text{s}^{-2}$)
ν, ν', ν_B	bubble volume, (m^3)
ν_{cell}	cell volume, (m^3)
Φ, ϕ	volume-specific interphase force term, ($\text{kg}\cdot\text{m}^{-2}\cdot\text{s}^{-2}$)
Ψ, ψ	Eulerian quantity, (-)
ω	fourth-order clipping function, (-)
$\varpi^B(\nu, \nu')$	break-up frequency, (s^{-1})

Subscripts

B	bubble
G	dispersed phase
L	continuous phase

References

- Akita, K., Yoshida, Y., 1974. *Bubble Size, Interfacial Area, and Liquid-Phase Mass Transfer Coefficient in Bubble Columns*. *Ind. Eng. Chem. Process Des. Dev.* 13(1), 84–91.
- Bai, W., 2010. *Experimental and Numerical Investigation of Bubble Column Reactors*. PhD Thesis, Eindhoven University of Technology, Eindhoven.
- Bouaifi, M., Hebrard, G., Bastoul, D., Roustan, M., 2001. *A comparative study of gas hold-up, bubble size, interfacial area and mass transfer coefficients in stirred gas-liquid reactors and bubble columns*. *Chem. Eng. Process.* 40(2), 97–111.
- Chappellear, D.C., 1961. *Models of a liquid drop approaching an interface*. *Journal of Colloid Science* 16(2), 186–190.
- Chen, P., Dudukovic, M.P., Sanyal, J., 2005a. *Three-dimensional simulation of bubble column flows with bubble coalescence and breakup*. *AIChE J.* 51(3), 696–712.
- Chen, P., Dudukovic, M.P., Sanyal, J., 2005b. *Numerical simulation of bubble columns flows: effect of different breakup and coalescence closures*. *Chem. Eng. Sci.* 60(4), 1085–1101.
- Coulaloglou, C.A., Tavlarides, L.L., 1977. *Description of interaction processes in agitated liquid-liquid dispersions*. *Chem. Eng. Sci.* 32(11), 1289–1297.
- Crowe, C.T., (Ed.), 2006. *Multiphase Flow Handbook*. CRC Press, Boca Raton, Florida, USA.
- Darmana, D., Deen, N.G., Kuipers, J.A.M., 2005. *Detailed modeling of hydrodynamics, mass transfer and chemical reactions in a bubble column using a discrete bubble model*. *Chem. Eng. Sci.* 60(12), 3383–3404.
- Darmana, D., Deen, N.G., Kuipers, J.A.M., 2006. *Parallelization of an Euler-Lagrange model using mixed domain decomposition and a mirror domain technique: Application to dispersed gas-liquid two-phase flow*. *J. Comput. Phys.* 220(1), 216–248.
- Deen, N.G., Solberg, T., Hjertager, B.H., 2001a. *Large eddy simulation of the Gas-Liquid flow in a square cross-sectioned bubble column*. *Chem. Eng. Sci.* 56(21), 6341–6349.
- Deen, N.G., 2001b. *An Experimental and Computational Study of Fluid Dynamics in Gas-Liquid Chemical Reactors*. PhD Thesis, Aalborg University, Esbjerg.
- Deen, N.G., van Sint Annaland, M., Kuipers, J.A.M., 2004. *Multi-scale modeling of dispersed gas-liquid two-phase flow*. *Chem. Eng. Sci.* 59(8), 1853–1861.
- Delnoij, E., Lammers, A., Kuipers, J.A.M., van Swaaij, W.P.M., 1997. *Dynamic simulation of dispersed gas-liquid two-phase flow using a discrete bubble model*. *Chem. Eng. Sci.* 52(9), 1429–1458.
- Gentle, J.E., 2003. *Random number generation and Monte Carlo methods*. Springer, New York, USA.

- Gillissen, J.J.J., Sundaresan, S., van Den Akker, H.E.A., 2011. *A lattice Boltzmann study on the drag force in bubble swarms*. J. Fluid Mech. 679, 101–121.
- Göz, M.F., Sommerfeld, M., Lain, S., 2006. *Instabilities in Lagrangian tracking of bubbles and particles in two-phase flow*. AIChE J. 52(2), 469–477.
- Hansen, R., 2009. *Computational and Experimental Study of Bubble Size in Bubble Columns*. PhD Thesis, Aalborg University, Esbjerg.
- Hu, G.S., 2009. *Towards large eddy simulation of dispersed gas-liquid two-phase turbulent flows*. PhD Thesis, West Virginia University, Morgantown.
- Ishii, M., Zuber, N., 1979. *Drag coefficient and relative velocity in bubbly, droplet or particulate flows*. AIChE J. 25(5), 843–855.
- Kantarci, N., Borak, F., Ulgen, K.O., 2005. *Bubble column reactors*. Process Biochem. 40(7), 2263–2283.
- Kim, W.K., Lee, K.L., 1987. *Coalescence behavior of two bubbles in stagnant liquids*. J. Chem. Eng. Jpn. 20(5), 448–453.
- Kirkpatrick, R.D., Lockett, M.J., 1974. *The influence of approach velocity on bubble coalescence*. Chem. Eng. Sci. 29(2), 2363–2373.
- Lage, P.L.C., Esposito, R.O., 1999. *Experimental determination of bubble size distributions in bubble columns: prediction of mean bubble diameter and gas hold up*. Powder Technol. 101(2), 142–150.
- Lain, S., Bröder, D., Sommerfeld, M., Göz, M.F., 2002. *Modelling hydrodynamics and turbulence in a bubble column using the Euler-Lagrange procedure*. Int. J. Multiphase Flow 28(8), 1381–1407.
- Lapin, A., Lübbert, A., 1994. *Numerical simulation of the dynamics of two-phase gas-liquid flows in bubble columns*. Chem. Eng. Sci. 49(21), 3661–3674.
- Lasheras, J.C., Eastwood, C., Martinez-Bazan, C., Montanes, J.L., 2002. *A review of statistical models for the break-up of an immiscible fluid immersed into a fully developed turbulent flow*. Int. J. Multiphase Flow 28(2), 247–278.
- Lau, Y.M., Deen N.G., Kuipers, J.A.M., 2010. *Bubble Breakup in Euler-Lagrange Simulations of Bubbly Flow*. 7th Int. Conf. on Multiphase Flow (ICMF), Tampa, Florida, USA.
- Lee, C.H., Erickson, L.E., Glasgow, L.A., 1987a. *Bubble breakup and coalescence in turbulent gas-liquid dispersions*. Chem. Eng. Commun. 59(1), 65–84.
- Lee, C.H., Erickson, L.E., Glasgow, L.A., 1987b. *Dynamics of bubble size distribution in turbulent gas-liquid dispersions*. Chem. Eng. Commun. 61(1), 181–195.
- Lehr, F., Millies M., Mewes, D., 2002. *Bubble-size distributions and flow fields in bubble columns*. AIChE J. 48(11), 2426–2443.
- Levich, V.G., 1962. *Physicochemical Hydrodynamics*. Prentice Hall Englewood Cliffs, New Jersey, USA.

- Liao, Y., Lucas, D., 2009. *A literature review of theoretical models for drop and bubble breakup in turbulent dispersions*. Chem. Eng. Sci. 64(15), 3389–3406.
- Liao, Y., Lucas, D., 2010. *A literature review on mechanisms and models for the coalescence process of fluid particles*. Chem. Eng. Sci. 65(10), 2851–2864.
- Luo, H., 1993. *Coalescence, Breakup and Liquid Circulation in Bubble Column Reactors*. PhD Thesis, Norwegian University of Science and Technology, Trondheim.
- Martinez-Bazan, C., Rodriguez-Rodriguez, J., Deane, G.B., Montanes, J.L., Lasheras, J.C., 2010. *Considerations on bubble fragmentation models*. J. Liquid Mech. 661, 159–177.
- Olmos, E., Vial, C.C., Wild, G., Midoux, N., 2001. *Numerical simulation of multiphase flow in bubble column reactors. Influence of bubble coalescence and break-up*. Chem. Eng. Sci. 56(21), 6359–6365.
- Radl, S., Khinast, J.G., 2010a. *Multiphase flow and mixing in dilute bubble swarms*. AIChE J. 56(9), 2421–2445.
- Radl, S., Suzzi, D., Khinast, J.G., 2010b. *Fast Reactions in Bubbly Flows: Film Model and Micromixing Effects*. Ind. Eng. Chem. Res. 49(21), 10715–10729.
- Smagorinsky, J., 1963. *General circulation experiments with the primitive equations - I. The basic experiment*. Mon. Wea. Rev. 91, 99–164.
- Sommerfeld, M., Bourloutski, E., Bröder, D., 2003. *Euler/Lagrange Calculations of Bubbly Flows with Consideration of Bubble Coalescence*. Can. J. Chem. Eng. 81(3), 508–518.
- Spalding, D.B., 1961. *A Single Formula for the Law of the Wall*. J. Appl. Mech. 28(3), 455–457.
- Tomiya, A., 2004. *Drag lift and virtual mass forces acting on a single bubble*. Proceedings of the 3rd International Symposium on Two-Phase Flow Modeling and Experimentation, Pisa, Italy.
- van den Hengel., E.I.V., Deen, N.G., Kuipers, J.A.M., 2005. *Application of Coalescence and Breakup Models in a Discrete Bubble Model for Bubble Columns*. Ind. Eng. Chem. Res. 44(14), 5233–5245.

CHAPTER

3

“A complex system that works is invariably found to have evolved from a simple system that worked.

A complex system designed from scratch never works and cannot be patched up to make it work.”

– John Gall (1925)

Impact of Bubble Breakage and Coalescence on Absorption and Chemisorption²

Abstract

In this study, the impact of bubble breakage and coalescence on the mass transfer and on the temporal evolution of species concentration during absorption and chemisorption is investigated. Thereby, the carbon dioxide absorption in water and the carbon dioxide chemisorption in sodium hydroxide solutions of various initial pH serve as model cases. A

² This chapter is based on: Gruber, M.C., Radl, S., Khinast, J.G., 2015. *Rigorous Modeling of CO₂ Absorption and Chemisorption: The Influence of Bubble Coalescence and Breakage*. Submitted to *Chem. Eng. Sci.*

three-dimensional Euler-Lagrange algorithm is used for the handling of the gaseous and the liquid phase in a laboratory-scale bubble column. The algorithm accurately forecasts the mean and fluctuating liquid velocities and predicts the bubble size distribution reasonably good.

The results show that breakage and coalescence critically impact mass transfer, liquid phase mixing, as well as reaction rates in systems with low to moderately large pH. In contrast, for extremely high pH values, shrinkage of bubbles becomes the dominating phenomenon. This is because bubble shrinkage leads to small bubbles, low gas hold-up, as well as little liquid phase agitation in the upper part of the reactor. Consequently, the relevance of breakage and coalescence events decreases gradually with increasing pH. A plot of the results as function of the overall pH illustrates that a regime change occurs close to pH 12.5. This transition is caused by a dramatic reduction of the gas hold-up, leading to a significant reduction of liquid-phase agitation.

3.1 Introduction

One of the most primitive, but nevertheless often used, reactor types for multiphase reactions are bubble columns (BCs). Typically, a BC is constructed as a cylindrical vessel which accommodates a gas sparger at its bottom. The sparger has the function to segment a continuous gas stream into discrete bubbles, which then ascend either through a liquid or through a suspension. The widespread of BCs in chemical, biochemical and pharmaceutical industries is based on some beneficial characteristics: BCs possess high heat and mass transfer rates and cause only low operation and maintenance costs due to absence of moving parts (Kantarci et al., 2005).

As simple as the construction of BCs may appear, so complex are the interactions of the phenomena that occur during its operation and which range over several orders of magnitudes in both, length and time scale. Fig. 3.1 schematically illustrates the correlations of some of them for the general case of gas-liquid mass transfer depending chemical reactions in the liquid phase, such as chemisorption.

As the figure points out, the bubbles' sizes, represented by their diameters d_B , take a center stage within these interdependencies. The ascending gas bubbles induce turbulences of lengths proportional to d_B into the liquid. These turbulences either decay to eddies in the order of micrometers (Kolmogorov microscale) or interact with each other in order to form

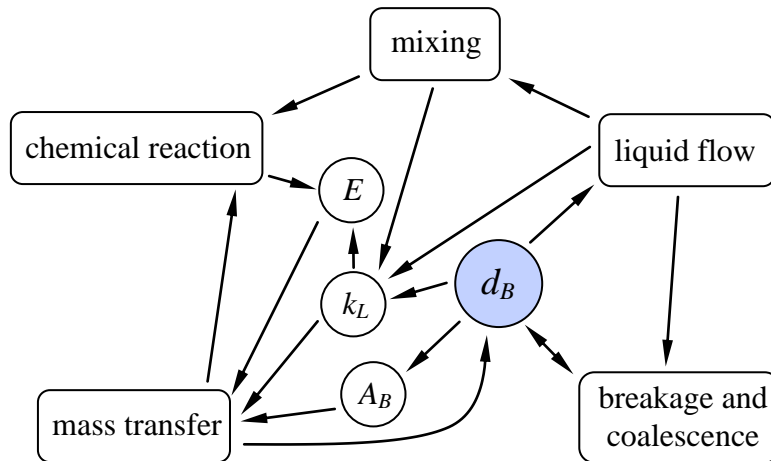


Figure 3.1: Schematic representation of the inter-dependency of break-up and coalescence, fluid flow, mixing, mass transfer and chemical reactions (adapted from Darmana, 2006).

unsteady recirculating flow patterns in the order of meters (macroscale of the BC). Moreover, small-scale turbulences can deform bubbles and cause bubble-bubble collisions, which leads to bubble break-ups and coalescences (B&Cs). The sizes of the bubbles also change due to interphase mass transfer, commonly caused through the dissolution of the gas in the liquid. Besides, the liquid turbulences cause macro- and micromixing of the liquid reactants (i.e. the dissolved gas, the solvent or already dissolved species), whose local distributions are in turn decisive for the reaction rates and hence, decisive for the evolution of the chemical reactions. Consequently, the reactions generate (via consumption) higher concentration gradients of the dissolved gas close to the gas-liquid interfaces, such that the interphase mass transfer is enhanced by the factor E . The enhanced mass transfer consequently leads to accelerated bubble shrinkage (BS), especially in case the reaction is fast and the gas consists of pure reactant. In addition, the rate of interphase mass transfer depends on the local hydrodynamics on the scale of the bubble, which is traditionally quantified by the mass transfer coefficient k_L and the interphase area A_B of the bubbles (Darmana, 2006).

The above mentioned interactions of various phenomena complicate the rational design and operation of BCs. For example, the *a priori* calculation of process parameters, that maximize the yield of the desired product and minimize impurities formed in side reactions, is challenging for a general reaction network. Also, the scale-up and transfer to a new BC design, or the optimization of reactor performance (in terms of yield and selectivity) is very limited using traditional engineering guidelines and simple correlations. Hence, state-of-the-art engineering of BCs is based on either (i) experimental studies on various scales using sophisticated image analysis or advanced chemometrics, or on (ii) detailed

computer simulations (Dani et al., 2007; Francois et al., 2011). With respect to the latter, computational fluid dynamics (CFD) has become a powerful tool, which has demonstrated that it can indeed guide the development process of BCs and gassed stirred tank (Krishna et al., 2001). CFD enables a quantification of the previous depicted phenomena with relative ease (without performing costly experiments). Additionally, CFD offers the possibility to explore the influence of a variety of phenomena on the total performance of BCs. Consequently, *a priori* information can be gained, e.g. which phenomena is most important for the performance of a full-scale BC, which is only possible to a limited extent with experimental routines. Clearly, CFD has attracted both academia and industry in recent years, which was caused by a number of factors: (i) progress in computer technology (i.e. the decrease of the cost associated with simulations), (ii) higher confidence in models to describe certain phenomena in a more robust (e.g. mechanistic) and realistic way, and (iii) the availability of computer algorithms to efficiently evaluate the relevant set of equations.

Two different approaches are widely used for the modeling of gas-liquid two-phase flows: First, the Euler-Euler (EE) approach treats both phases as interpenetrating continua and describes their time-dependent motion via a set of volume-averaged Navier-Stokes equations (NSEs). The interactions between the phases are incorporated through exchange models (Monahan et al., 2005). Since individual properties of the gas bubbles are lost during an averaging procedure (required for deriving the NSEs), a population balance equation (PBE) must be formulated in order to model the distribution of bubble sizes. Thereby, the PBE relies on closures, e.g. for bubble-bubble collision frequencies, that are based on the local gas fraction and account for phenomena such as B&C and BS caused by interphase mass transfer (Zhang et al., 2007).

Second, the Euler-Lagrange (EL) approach regards the liquid phase as continuum and the corresponding NSEs are formulated just as for the EE approach. On the other hand, the bubbles are tracked individually by solving Newton's equation of translational motion. Both phases interact via exchange terms for momentum and mass. Consequently, this individual bubble treatment enables a more direct on bubble-bubble and bubble-liquid interactions than the EE approach: The EL approach does not require an additional PBE to model the bubble properties, since they are already part of the solution. Hence, the EL approach allows a "more realistic" observation of the impact of phenomena such as B&C on bubble size distributions (BSDs). However, the main disadvantage of the EL approach are higher computational costs due to the individual bubble treatment, wherefore the sizes of the simulated systems are

restricted to laboratory-scale or small pilot-scale BCs (Witz et al., 2014). Clearly, the EL approach is preferred for fundamental studies (Delnoij et al., 1997).

The published literature concerning EL simulations often assumes monodisperse bubbles (see e.g. Delnoij et al., 1997; Deen et al., 2001; Radl et al., 2010a, 2010b; Besbes et al., 2015), while more sophisticated studies consider bubble coalescence (e.g. Darmana, 2006). In general, B&C needs to be considered for higher gas flow rates as used in industry (Dhotre et al., 2013). In recent years, some authors incorporated the topic of bubble B&C in their researches (van den Hengel, 2005; Lau et al., 2010; Gruber et al., 2013). Their findings indicate that the Sauter mean diameter d_{32} of the bubble plume varies significantly over the reactor height: While the majority of bubble coalescences occur in the vicinity of the gas sparger, bubble break-up events take place over the entire height. This circumstance is reflected in a maximum d_{32} near the gas sparger, which drops subsequently over the remaining column height. However, these previous studies have not investigated the impact of B&C on (reactive) interphase mass transfer.

The algorithm used in the present study considers four-way coupling between the phases, and its implementation is complementary described in Gruber et al. (2013). For B&C, the models of Coulaloglou and Tavlarides (1977) are implemented in the algorithm. In order to reflect the random nature of B&C, the decisions if bubbles are going to break up or coalesce is based on a stochastic approach.

This study extends the work of the aforementioned groups on the impact of B&C on the outcome of reactions in a BC. Specifically, focus is put on the influence of the interphase mass transfer (which depends on the bubble sizes and hence on coalescence and break-up) on the temporal evolution of a chemical model reaction. The results of the EL simulations are then compared with the outcome of simulations without B&C. To complete the understanding of key model parameters that impact the results of EL simulations, this study also evaluates the effect of BS on the reactions in a BC.

The systems investigated in the current contribution include (i) the absorption of carbon dioxide (CO_2) in water, as well as (ii) the chemisorption of gaseous CO_2 in aqueous sodium hydroxide ($NaOH$) solutions. The reaction model and the technique which is used for solving the transport equation are based on the work of Darmana (2006). Finally, the simulation approach is applied to a three-dimensional rectangular laboratory-scale BC, which is in literature well-known as the “Deen case” (Deen et al., 2001).

3.2 Modeling

3.2.1 Liquid Hydrodynamics

The hydrodynamic of the continuous phase (L) is represented through the volume-averaged Navier-Stokes equations (NSEs) which are composed of continuity and momentum conservation equations:

$$\frac{\partial(\alpha_L \rho_L)}{\partial t} + \nabla \cdot (\alpha_L \rho_L \mathbf{u}_L) = \dot{M}_{B \rightarrow L} - \dot{M}_{L \rightarrow B}, \quad (3.1)$$

$$\frac{\partial(\alpha_L \rho_L \mathbf{u}_L)}{\partial t} + \nabla \cdot (\alpha_L \rho_L \mathbf{u}_L \mathbf{u}_L) = -\alpha_L \nabla p - \nabla \cdot (\alpha_L \boldsymbol{\tau}_L) + \alpha_L \rho_L \mathbf{g} + \boldsymbol{\Phi}, \quad (3.2)$$

where \mathbf{g} is the gravitational constant and the liquid properties ρ_L , \mathbf{u}_L , and p are the density, the velocity and the pressure, respectively. In the NSEs, the influence of the dispersed phase (B) is incorporated through the liquid phase volume fraction α_L and source terms to account for interphase exchange: the momentum transfer rate $\boldsymbol{\Phi}$ and the mass transfer rate \dot{M} . By assuming that the liquid has a Newtonian characteristic, the stress tensor $\boldsymbol{\tau}_L$ is given through:

$$\boldsymbol{\tau}_L = -\mu_{L,EFF} \left(\nabla \mathbf{u}_L + (\nabla \mathbf{u}_L)^T - \frac{2}{3} \mathbf{I}(\nabla \cdot \mathbf{u}_L) \right). \quad (3.3)$$

In this study, the effective viscosity $\mu_{L,EFF}$ is composed of the molecular viscosity μ_L and the sub-grid scale (SGS) viscosity $\mu_{L,SGS}$:

$$\mu_{L,EFF} = \mu_L + \mu_{L,SGS}. \quad (3.4)$$

The direct numerical solution of the NSEs is computationally costly, due to the great order of magnitudes of length and time scales. Alternatively, the large eddy simulation (LES) approach is used in this study. The LES solves the NSEs only for length scales larger than the one of a characteristic cell length $\Delta = (\Delta_x \Delta_y \Delta_z)^{1/3}$. Thereby, the LES technique relies on Kolmogorov's theory of self-similarity of small eddies and on their universal character: Contrary to the flow dependency and anisotropy of large eddies, small eddies are self-similar and nearly isotropic, which makes them easy to be modeled. For the modeling of the SGS viscosity, the approach from [Smagorinsky \(1963\)](#) is used:

$$\mu_{L,SGS} = \rho_L (C_S \Delta)^2 |\mathbf{S}|, \quad (3.5)$$

where C_S is the Smagorinsky constant and \mathbf{S} is the (filtered) rate of strain. The SGS kinetic energy and the turbulent energy dissipation rate are defined as $k_{SGS} = 2C_K \Delta^2 \mathbf{S}^2 / C_E$ and $\epsilon = C_E k_{SGS}^{3/2} / \Delta$, respectively. Thereby, C_K and C_E are model constants, whereat the latter has the fixed value of 1.05. Both constants are related to the Smagorinsky constant through $C_S = (2C_K^3 / C_E)^{1/4}$. In this study, a Smagorinsky constant of $C_S = 0.10$ is used for all simulations.

3.2.2 Bubble Dynamics

In order to resolve the dynamics of the bubbles with the EL approach, the motion of each individual bubble has to be calculated from its mass and momentum equation. For a typical laboratory-scale bubble column (BC), i.e. insignificant changes in the absolute bubble pressures, a bubble can be assumed to be an incompressible sphere with a rigid surface. The gas mass balance equation and Newton's equation of motion are then given for each bubble by:

$$\rho_B \frac{d\nu_B}{dt} = \dot{m}_{B \rightarrow L} - \dot{m}_{L \rightarrow B}, \quad (3.6)$$

$$\rho_B \nu_B \frac{d\mathbf{u}_B}{dt} = \sum \mathbf{F}, \quad (3.7)$$

with the gas density ρ_B and the bubble volume $\nu_B = \pi/6 d_B^3$. Thereby, the coupling with the liquid phase is taken into account via the contributions of the interphase mass transfer rate \dot{m} and of the net force $\sum \mathbf{F}$. The latter is the total force that is experienced by each bubble in the presence of the liquid. The net force is composed of the following individual forces: the buoyancy force \mathbf{F}_B , the lift force \mathbf{F}_L , the drag force \mathbf{F}_D and the virtual mass force \mathbf{F}_{VM} :

$$\sum \mathbf{F} = \mathbf{F}_B + \mathbf{F}_L + \mathbf{F}_D + \mathbf{F}_{VM}. \quad (3.8)$$

The definitions of the individual bubble forces, including their corresponding closures, are listed in Tab. 3.1. Therein, C_{VM} , C_D , C_L , Re_B and $E\ddot{o}$ are the coefficients for the virtual mass force, the drag force and the lift force, as well as the bubble Reynolds number and the Eötvös number, respectively. A detailed explanation concerning the derivation of the forces can be found in [Tomiyama et al. \(1998, 2002\)](#).

Table 3.1: Overview of forces and closures used in this study.

Forces	Closures
$\mathbf{F}_B = \nu_B(-\nabla p + \rho_G \mathbf{g})$	$C_{VM} = 0.5$
$\mathbf{F}_{VM} = -C_{VM} \rho_L \nu_B \left(\frac{D_B \mathbf{u}_B}{D_B t} - \frac{D_L \mathbf{u}_L}{D_L t} \right)$	$C_D = \max \left(\min \left(\frac{16}{Re_B} (1 + 0.15 Re_B^{0.687}), \frac{48}{Re_B} \right), \frac{8}{3} \frac{E\ddot{\alpha}}{E\ddot{\alpha} + 4} \right)$
$\mathbf{F}_D = -\frac{C_D}{2} A_B \rho_L \mathbf{u}_B - \mathbf{u}_L (\mathbf{u}_B - \mathbf{u}_L)$	$C_L = \begin{cases} \min(0.288 \tanh(0.121 Re_B), f(E\ddot{\alpha}_d)) & E\ddot{\alpha}_d \leq 4 \\ f(E\ddot{\alpha}_d) & 4 < E\ddot{\alpha}_d \leq 10 \\ -0.29 & 10 < E\ddot{\alpha}_d \end{cases}$
$\mathbf{F}_L = -C_L \rho_L \nu_B (\mathbf{u}_B - \mathbf{u}_L) \times \nabla \times \mathbf{u}_L$	$f(E\ddot{\alpha}_d) = 0.00105 E\ddot{\alpha}_d^3 - 0.0159 E\ddot{\alpha}_d^2 - 0.0204 E\ddot{\alpha}_d + 0.474$ $E\ddot{\alpha}_d = E\ddot{\alpha} (1 + 0.163 E\ddot{\alpha}^{0.757})^{2/3}$

The liquid velocity \mathbf{u}_L , used in Tab. 3.1 to compute the forces on the bubble, is composed of a resolved component, interpolated from the neighboring grid points, and an unresolved (SGS) fluctuating component \mathbf{u}_L' . In order to capture also the influence of \mathbf{u}_L' on the motion of a bubble, a Langevin type model is used in this study (Pozorski and Minier, 1998; Sommerfeld, 2001). In this closure model, here denoted as bubble dispersion model, the fluctuations $\mathbf{u}_L'(t^n)$ at the particle's actual position are correlated with the fluctuations $\mathbf{u}_L'(t^{n-1})$ from the particle's former position at the time t^{n-1} via a correlation function $\mathbf{R}_B(\Delta t, \Delta \mathbf{r})$. A brief summary of the bubble dispersion model is given in the appendix.

3.2.3 Transport Equation of Chemical Species

Each species j of the liquid mixture is represented by its mass fraction Y_L^j , whereat all species complement each other to unity $\sum_j Y_L^j = 1$. The temporal variation of Y_L^j is described through a transport equation that considers fraction changes due to convection, diffusion, as well as consumption or production caused by chemical reaction or interphase transfer:

$$\frac{\partial(\alpha_L \rho_L Y_L^j)}{\partial t} + \nabla \cdot (\alpha_L (\rho_L \mathbf{u}_L Y_L^j - \rho_L D_{EFF}^j \nabla Y_L^j)) = (\dot{M}_{B \rightarrow L}^j - \dot{M}_{L \rightarrow B}^j) + \alpha_L S^j. \quad (3.9)$$

Note, that the above equation is a spatially filtered form of a microscopic transport equation and hence, dispersion due to SGS motion needs to be modeled via an effective diffusion coefficient D_{EFF}^j . This spatially distributed variable is composed of the species diffusivity D^j and the SGS contribution, whereupon the latter depends on the Schmidt number Sc^j of the particular species:

$$D_{EFF}^j = D^j + \frac{\mu_{L,EFF}}{\rho_L Sc^j}. \quad (3.10)$$

Referring to Radl et al. (2010b), the Schmidt number has no significant impact on species mixing, wherefore a constant value of $Sc=0.7$ is used for all species. The reaction source terms S^j for the chemisorption of carbon dioxide (CO_2) into aqueous sodium hydroxide ($NaOH$) solutions are reported in Tab. 3.2.

3.2.4 Reaction Model

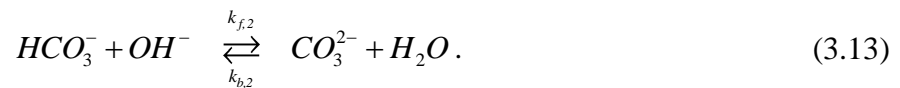
The chemisorption of CO_2 into aqueous $NaOH$ solutions takes place in three steps: in the first step, the gaseous carbon dioxide $CO_2(g)$ is physically dissolved in the liquid:



In the second step, the dissolved carbon dioxide $CO_2(aq)$ reacts with hydroxide ions (OH^-) to form the intermediate product of hydrogen carbonate ions (HCO_3^-):



with k_f and k_b as the forward and the backward reaction rate constants, respectively. In the last reaction step, the HCO_3^- ions react onward with the OH^- ions to form carbonate ions (CO_3^{2-}):



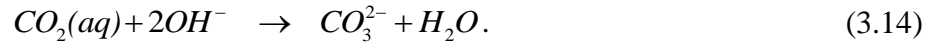
Following Pohorecki (1988), the forward reaction rate of the second reaction Eq. (3.13) is significantly higher than the one of the first reaction Eq. (3.12). Therefore, it can be concluded that the first reaction step is the limiting one. The expressions for the forward reaction rate R_f and for the backward reaction rate R_b of the relevant reactions are listed in Tab. 3.2. The values for k_f and k_b in Eqs. (3.12) and (3.13) are summarized in the appendix.

At high values of the pH, the equilibrium concentration of the HCO_3^- ions is small and can be neglected. Thus, for highly concentrated $NaOH$ solutions, only the following overall reaction,

Table 3.2: Summarization of the source terms S^j for the diverse species j of the transport equation Eq. (3.9), of the forward R_f and of the backward reaction rates R_b of the Eqs. (3.12) and (3.13). Here, k_f , k_b and M^j are the forward and the backward reaction rate constants and the molar masses, respectively.

j	S^j ($\text{kg}\cdot\text{m}^{-3}\cdot\text{s}^{-1}$)	
	Detailed reaction	Overall reaction
$\text{CO}_2(\text{aq})$	$(R_{b,1}-R_{f,1})M^{\text{CO}_2}$	$-R_{f,1}M^{\text{CO}_2}$
OH^-	$(R_{b,1}+R_{b,2}-R_{f,1}-R_{f,2})M^{\text{OH}^-}$	$-2R_{f,1}M^{\text{OH}^-}$
HCO_3^-	$(R_{f,1}+R_{f,2}-R_{b,1}-R_{b,2})M^{\text{HCO}_3^-}$	
CO_3^{2-}	$(R_{f,2}-R_{b,2})M^{\text{CO}_3^{2-}}$	$R_{f,1}M^{\text{CO}_3^{2-}}$
	$R_{f,1} = k_{f,1}[\text{CO}_2(\text{aq})][\text{OH}^-]$	$R_{f,2} = k_{f,2}[\text{HCO}_3^-][\text{OH}^-]$
	$R_{b,1} = k_{b,1}[\text{HCO}_3^-]$	$R_{b,2} = k_{b,2}[\text{CO}_3^{2-}]$

with a single forward reaction rate step characterized by $R_f=k_{f,1}[\text{CO}_2(\text{aq})][\text{OH}^-]$, needs to be considered (Hikita et al., 1976):



Finally, following the investigations of Bhat (1998), the temperature during the chemisorption can be assumed to be constant, wherefore $T=298.15\text{ K}$ is used for the whole system.

3.2.5 Interphase Mass Transfer

In this study, the interphase mass transfer of CO_2 is modeled based on a mass fraction difference between the bubble bulk $Y_B^{\text{CO}_2^\infty}$ and the liquid bulk $Y_L^{\text{CO}_2^\infty}$, as shown in Fig. 3.2.

Assuming that the gas-side mass transfer resistance is negligible, the mass transfer rate $\dot{m}_B^{\text{CO}_2}$ for a single bubble is proportional to the gradient among the liquid side interface $Y_L^{\text{CO}_2^*}$ and the liquid bulk:

$$\dot{m}_B^{\text{CO}_2} = Ek_L^{\text{CO}_2} A_B \rho_L (Y_L^{\text{CO}_2^*} - Y_L^{\text{CO}_2^\infty}). \quad (3.15)$$

Here, E , $k_L^{\text{CO}_2}$ and $A_B=\pi d_B^2$ are the enhancement factor, the mass transfer coefficient in a non-reacting system and the surface area of the bubble, respectively. The mass fraction on the

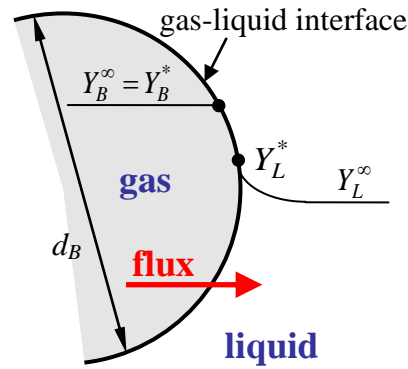


Figure 3.2: Schematic representation of the mass fractions of the liquid side limited interphase mass transfer of CO_2 .

liquid side interface is related to the mass fraction in the bubble bulk by Henry's law: $\rho_L Y_L^{CO_2^*} = (\rho_B Y_B^{CO_2^\infty}) H^{CO_2}$. Moreover, the dimensionless Henry constant for the dissolution of CO_2 into pure water has the value $H_w^{CO_2} = 2.94 \times 10^{-6} T \exp(2044/T)$ (Versteeg and van Swaaij, 1988). By taking into account that the CO_2 solubility decreases with increasing salt concentration (the so-called "salting-out" effect), the Henry constant H^{CO_2} is adapted through the relation: $\log(H_w^{CO_2} / H^{CO_2}) = \sum_i (h_l + h_G) [i]$ (Weisenberger and Schumpe, 1996). Thereby, $[i]$ symbolizes the local concentration of the electrolyte i in the liquid. The values used for the ion- and gas-specific parameters h_l and h_G are listed up in Tab. 3.3.

Table 3.3: Ion- and gas-specific parameters h_l and h_G and diffusivities D^j for $T=298.15$ K (Weisenberger and Schumpe, 1996; Cussler, 2007).

	CO_2	OH^-	HCO_3^-	CO_3^{2-}	Na^+
$h_G / h_l (m^3 \cdot kmol^{-1})$	-0.0172	0.0839	0.0967	0.1423	0.1143
$D^j \times 10^9 (m^2 \cdot s^{-1})$	1.93	5.28	1.10	0.92	1.33

The mass transfer of CO_2 is accelerated due to the consumption of $CO_2(aq)$ in the liquid film close to the bubble's interface. This acceleration is reflected by the enhancement factor E , which is a function of the Hatta number $Ha = (k_{f,l} D^{CO_2} [OH^-])^{1/2} / k_L^{CO_2}$. In this study, the approximation from Westerterp et al. (1994) is used for the calculation of the enhancement factor:

$$E = \begin{cases} 1 & E_\infty \leq 1 \\ -\frac{Ha^2}{2(E_\infty - 1)} + \left(\frac{Ha^4}{4(E_\infty - 1)^2} + \frac{E_\infty Ha^2}{E_\infty - 1} + 1 \right)^{1/2} & 1 < E_\infty \end{cases}, \quad (3.16)$$

$$E_\infty = \left(1 + \frac{D^{OH^-} [OH^-]}{2D^{CO_2} H^{CO_2} [CO_2(aq)]} \right) \left(\frac{D^{CO_2}}{D^{OH^-}} \right)^{1/2}, \quad (3.17)$$

As shown in Fig. 3.3, the chemisorption of CO_2 into aqueous $NaOH$ solutions is not enhanced for pH less than 12, while it increases strongly for pH greater than 12.

Finally, the mass transfer coefficient $k_L^{CO_2} = ShD^{CO_2} / d_B$ can be determined by the empirical Sherwood number relation $Sh = 2 + 0.015 + Re_B^{0.89} Sc^{0.7}$ proposed by Brauer (1981). Note that this relationship is only strictly valid for isolated bubbles of spherical shape. Since even highly resolved direct numerical simulations have not been able to derive a more appropriate Sherwood number model so far (see e.g. Roghair, 2012), this simple relationship is used in the present study.

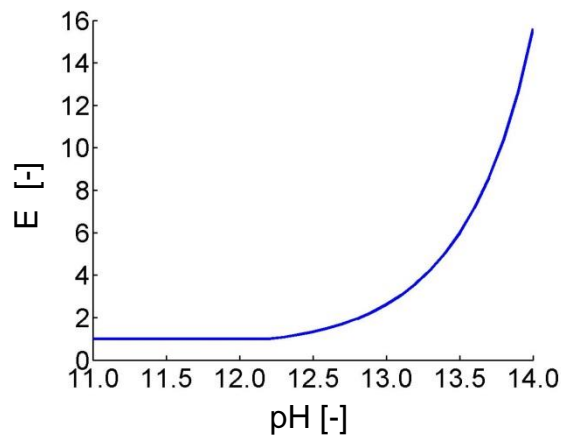


Figure 3.3: The enhancement factor E for CO_2 dissolution as function of the pH value.

3.2.6 Break-up and Coalescence Model of Coualoglou and Tavlarides

Coualoglou and Tavlarides (1977) derived binary break-up and coalescence (B&C) models for bubbles in turbulent flows. The coalescence probability for two bubbles of diameters d_{B1} and d_{B2} is given as function of their equivalent diameter $d_{eq} = 2 / (1/d_{B1} + 1/d_{B2})^{-1}$:

$$P^C(d_{eq}) = C_C \frac{\mu_L \rho_L \epsilon d_{eq}^4}{16\sigma^2} \left(\frac{1}{h_f^2} - \frac{1}{h_i^2} \right), \quad (3.18)$$

with the surface tension σ and the model constant C_C . Experimental investigations suggest the values of 10^{-4} m and 10^{-8} m for the initial film thickness h_i and the critical film thickness h_f , respectively. The break-up frequency $\varpi^B(d_B)$ and the “daughter” bubble size distribution (BSD) $\beta^B(d_B', d_B)$ for a breaking up “mother” bubble of diameter d_B are given by:

$$\varpi^B(d_B) = C_{B1} \left(\frac{\epsilon}{d_B^2} \right)^{1/3} \exp \left[-\frac{C_{B2} \sigma}{\rho_G \epsilon^{2/3} d_B^{5/3}} \right], \quad (3.19)$$

$$\beta^B(d_B', d_B) = \frac{2.4}{d_B^3} \exp \left[-\frac{4.5(2d_B'^3 - d_B^3)^2}{d_B^6} \right]. \quad (3.20)$$

Again, C_{B1} and C_{B2} are model constants. The diameters of the through break-up generated daughter bubbles are given by d_B' and $(d_B^3 - d_B'^3)^{-3}$.

3.2.7 Numerical Implementation

As illustrated in Fig. 3.4, all iteration cycles of the EL algorithm start with the Lagrangian tracking of the bubbles. In the first step, new bubbles are injected into the computational domain. Then, each bubble in the domain is examined, whether the criterion for its break-up is fulfilled or not. Thereby, the method described by [Gruber et al. \(2013\)](#) serves as criterion for the break-up, and for the calculation of the volumes of the daughter bubbles. If the break-up condition is fulfilled for a bubble, it is replaced by two daughter bubbles. In the third step, the interphase mass transfers and the experienced net forces are calculated for all bubbles in the domain. Based on these calculations, the diameters and positions of the bubbles are updated. During the movement of the bubbles, bubble-bubble interactions can occur, which result in either coalescences or rebounds events.

After the Lagrangian bubble tracking, the liquid is handled in the Eulerian way. Therefore, the volume fraction and the interphase exchange terms for momentum and mass are determined. With this information at hand, the governing equations of the liquid phase are evolved in time. Finally, the spatial mass fraction distribution is determined for all involved chemical species. Therefore, the reaction source terms are calculated first, whereupon the spatial distributions are obtained by solving the corresponding transport equation.

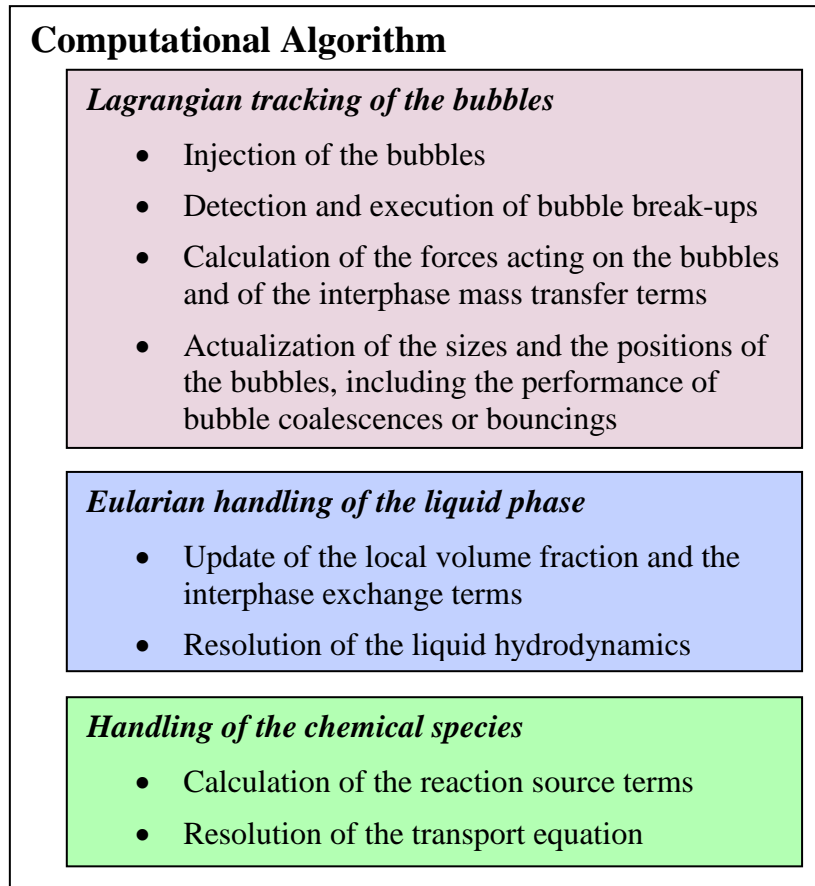


Figure 3.4: Schematic view of the computational sequence.

3.2.8 The “Deen Case”

In this study, the three-dimensional rectangular BC used by Deen et al. (2001) in their experiments, and hence denoted here as “Deen case”, is utilized as setup and for validation purposes. In Deen’s experiments, the column had a cross-section area of $0.15 \times 0.15 \text{ m}^2$ and was filled with water up to a height of 0.45 m , as shown in Fig. 3.5(a). A centrally arranged sparger was mounted at the bottom, consisting of 7×7 circular-shaped holes with a square pitch of 6.25 mm (see Fig. 3.5(b)). The sparger segmented a continuous air stream, flowing with a superficial velocity of $4.9 \text{ mm} \cdot \text{s}^{-1}$, into bubbles of 4 mm in diameter. Hansen (2009) measured the BSD of the Deen case, using an interferometric particle imaging (IPI) technique, between the heights of 0.20 m and 0.30 m . He found the values of 2.26 mm and 5.94 mm for the arithmetic mean diameter $d_{10} = \sum N_i d_{B,i} / \sum N_i$ and the Sauter mean diameter $d_{32} = \sum N_i d_{B,i}^3 / \sum N_i d_{B,i}^2$, respectively.

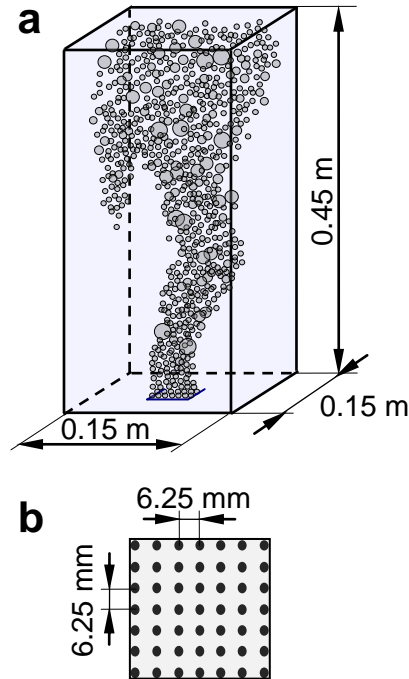


Figure 3.5: Schematic view of (a) the computational domain and (b) the perforated plate used as a sparger.

3.2.9 Simulation Setup

The Deen case is adopted for the computational model via a mesh that is composed of $15 \times 15 \times 45$ cubic cells with a constant length of 10 mm . For the fluid, no-slip conditions are applied for each wall except for the outlet (top face), for which a free-slip condition is used. Furthermore, second-order accurate numerical schemes are used in space (for the convection and diffusion terms) and time to avoid excessive numerical diffusion. For the bubbles, elastic bounce-back conditions are applied for bubble-wall interactions.

As in Deen's experiments, a continuous gas stream of $1.10 \times 10^{-4} \text{ m}^3 \cdot \text{s}^{-1}$ is segmented into uniform bubbles, which enter at the bottom with a diameter of 4 mm and a speed of $0.269 \text{ m} \cdot \text{s}^{-1}$. The bubbles then rise through the liquid until they reach the top face, whereupon they are removed from the computational domain. Additionally, bubbles are also removed from the domain if they dissolve to a (arbitrarily chosen) size smaller than $20 \text{ }\mu\text{m}$. Their volume is then treated as transferred to the liquid phase, in order to conserve mass. Moreover, the temperature in the system is chosen to be uniform and equal to $20 \text{ }^\circ\text{C}$.

According to the simulation cases, pure water or aqueous NaOH solutions of certain initial pH are used as liquid. Due to the lack of more accurate data concerning the liquid phase's

transport properties, the initial fluid properties (e.g. density, viscosity) are treated as constant during the simulations. Each simulation starts with the injection of the bubbles into a stagnant liquid. For the solution of the NSEs, a time step of 1 ms is used, while the simulation of the bubbles proceeds with a time step of 0.1 ms . Using this time increments, only negligible differences occur compared to simulations with smaller time steps ([Darmana, 2006](#)). The time step for the transport equation depends on the initial pH of the NaOH solution: The higher the concentration, the smaller the time step is chosen, in order to prevent negative species concentrations in the computational domain due to the explicit treatment of the reaction source terms.

3.3 Results and Discussion

All simulated cases, as well as their specific setups, are summarized in Tab. 3.4. Each simulation was run on a single core of an Intel® i7-3930K CPU. Depending on the simulated case, the number of bubbles in the system averaged between 3,400 and 9,800. Further, depending on the performed reaction, the durations of the simulations lay between 4 and 12 days.

Table 3.4: Summary of the simulated cases: The cases 0a-0c served for the verification of the mixing, of the mass transfer and of the diameter shrinkage, while the case 01 was used as standard case in this study. In case 02, the impact of the bubble SGS (Langevin) model was tested, while in case 03 the bubble size distribution (BSD) of the break-up and coalescence (B&C) model was evaluated. Concerning bubble shrinkage (BS) and B&C, the cases 8-11, 16-19 and 20-23 were built up in the same sequence as the cases 04-07, while the cases 14-15 followed the same order as the cases 12-13. If both, BS as well as bubble B&C, were not considered for a case, then the BSD therein was monodisperse ($d_B=0.004$ m), otherwise polydisperse.

Case	Duration	SGS model	Mass transfer	BS	B&C	Reaction	Initial solution	Gas
0a	12 s	–	–	–	–	–	3 species	CO ₂
0b	500 s	–	yes	–	–	–	water	CO ₂
0c	0.8 s	–	yes	yes	–	–	NaOH (pH 14.0)	CO ₂
01	180 s	–	–	–	–	–	water	air
02	180 s	yes	–	–	–	–	water	air
03	180 s	yes	–	–	yes	–	water	air
04	180 s	yes	yes	–	–	–	water	CO ₂
05	180 s	yes	yes	yes	–	–	water	CO ₂
06	180 s	yes	yes	–	yes	–	water	CO ₂
07	180 s	yes	yes	yes	yes	–	water	CO ₂
08-11	140 s	yes	yes	– / yes	– / yes	yes	NaOH (pH 12.0)	CO ₂
12	200 s	yes	yes	yes	–	yes	NaOH (pH 12.5)	CO ₂
13	200 s	yes	yes	yes	yes	yes	NaOH (pH 12.5)	CO ₂
14-15	200 s	yes	yes	yes	– / yes	yes	NaOH (pH 13.0)	CO ₂
16-19	200 s	yes	yes	– / yes	– / yes	yes	NaOH (pH 13.5)	CO ₂
20-23	200 s	yes	yes	– / yes	– / yes	yes	NaOH (pH 14.0)	CO ₂

3.3.1 Verification of the Mixing and the Mass Transfer Models

In order to verify the implemented models for liquid mixing and for interphase mass transfer, three simulations, namely the cases 0a, 0b and 0c, were setup.

Liquid Mixing

To illustrate the liquid mixing rate and to test the conservation of individual species, three different tracer species with the same material properties as water were vertically stacked over each other in the computational domain (Darmana, 2006). In doing so, each species occupied a third of the volume of the bubble column (BC). Other details of the simulation setup were chosen to replicate the previously described Deen case. After the start of the simulation, the mass fractions of three species were tracked until a homogeneously mixed state was achieved (case 0a). Fig. 3.6 shows the local temporal variations of the three species mass fractions at a probe point localized in the middle of the BC. As can be seen in the figure, it took about approximately 10 s till a well-mixed state was reached.

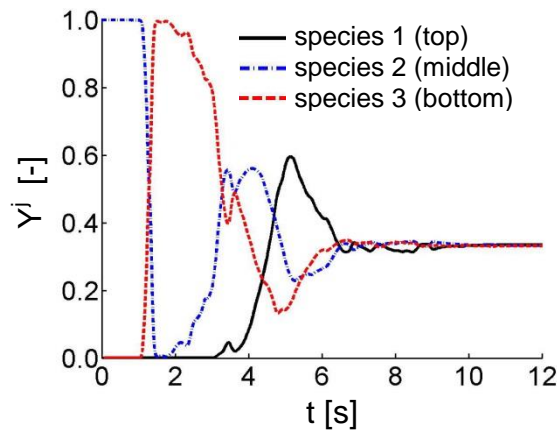


Figure 3.6: Temporal evolution of the mass fractions (mixing) of three tracer species in the centerline of the column at a height of $z/H=0.5$ (case 0a).

Interphase Mass Transfer

For the purpose of verifying the correct implementation of the mass transfer model, an analytical solution of Eq. (3.15), initially reported by Darmana (2006), was used as reference. Assuming that CO_2 bubbles of constant diameter ascend in water, the mean mass fraction $\bar{Y}_L^{CO_2\infty}$ of dissolved CO_2 in the column can be expressed as normalized function of time:

$$\frac{\rho_L \bar{Y}_L^{CO_2\infty}(t)}{\rho_B H^{CO_2}} = 1 - \exp\left(-\frac{t \bar{N}_B k_L^{CO_2} A_B}{V_L}\right), \quad (3.21)$$

with \bar{N}_B , V_L and A_B being the average number of bubbles, the liquid volume in the BC and the bubble surface area, respectively. To simplify the calculation of the mass transfer

coefficient $k_L^{CO_2}$, the following bubble drag force coefficient was used:

$$C_D = 2/3(E\dot{\sigma})^{1/2}. \quad (3.22)$$

Then, the terminal rise velocity $u_{B,TERM}$ of the bubbles was given through $u_{B,TERM}=(4(\rho_L-\rho_B)\sigma g/\rho_L)^{1/4}$. The verification of the mass transfer strongly depended on the value of \bar{N}_B , which was obtained by continuously averaging the number of bubbles during the simulation. Fig. 3.7 shows a comparison of the temporal evolution of the analytical and the numerically predicted mass fraction (case 0b) of $CO_2(aq)$.

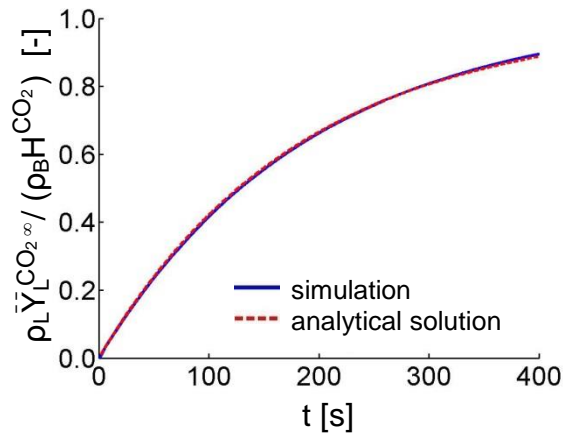


Figure 3.7: The normalized mean mass fraction of dissolved CO_2 in the bubble column as function of time (case 0b, $\bar{N}_B=4480$).

Shrinkage of a Single Bubble

Finally, to verify the correct implementation of the mass transfer enhancement factor, a test case was set up in which a single bubble with an initial diameter of $d_B=0.004\text{ m}$ rose through a quiescent sodium hydroxide solution of pH 14 (Zhang et al., 2009). By setting the liquid side mass fraction of dissolved CO_2 permanently to zero ($Y_L^{CO_2^\infty}=0$), the temporal decrease of d_B is constant and given by:

$$\frac{d(d_B)}{dt} = -2E k_L^{CO_2} H^{CO_2}. \quad (3.23)$$

Again, the calculation of $k_L^{CO_2}$ was simplified by using Eq. (3.22) for the drag force coefficient. In Fig. 3.8, the integrated form of Eq. (3.23) is compared with the simulated decrease of the diameter (case 0c). As can be seen in the figure, the numerical model showed

excellent agreement with the analytical solution.

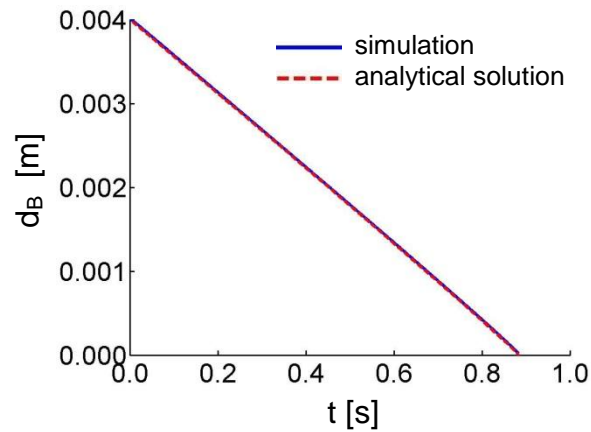


Figure 3.8: The shrinkage of a single bubble during its ascent in a quiescent *NaOH* solution of pH 14.0 (case 0c).

3.3.2 Liquid Velocity Profiles

The presented modeling technique demanded a quantitative validation of the simulated liquid hydrodynamics with experimental data. The experimental data was obtained from [Deen et al. \(2001\)](#), who performed particle image velocimetry (PIV) measurements for certain positions along the column width. On the other hand, the simulation data was determined through time-averaging of the liquid velocities for a sufficiently long duration. In doing so, the averaging was started after 20 s, which was a sufficiently long period of time for the liquid flow to be fully developed. As criterion for the end of the averaging period served the convergence of the velocity profiles that was reached after a runtime of 180 s ([Gruber et al., 2013](#)). A comparison of the thus obtained average and fluctuating velocity profiles is shown in Fig. 3.9. Clearly, the predictions for the standard case (monosized bubbles, case 01) reveal good agreement for both the qualitative (e.g. the position of the velocity maxima) and quantitative (e.g. the magnitude of the maxima) characteristics of the flow.

With exception of the standard case, the bubble dispersion model has been used for all subsequent cases. The impact of this model on the liquid hydrodynamics was investigated in case 02 and the results are shown in Fig. 3.9 and compared to the results of case 01. In comparison to the standard case, the SGS model resulted in a lower and laterally displaced average velocity maximum. Furthermore, the dispersion model seemed to resolve the bimodal shape of the vertical fluctuating profile more accurately.

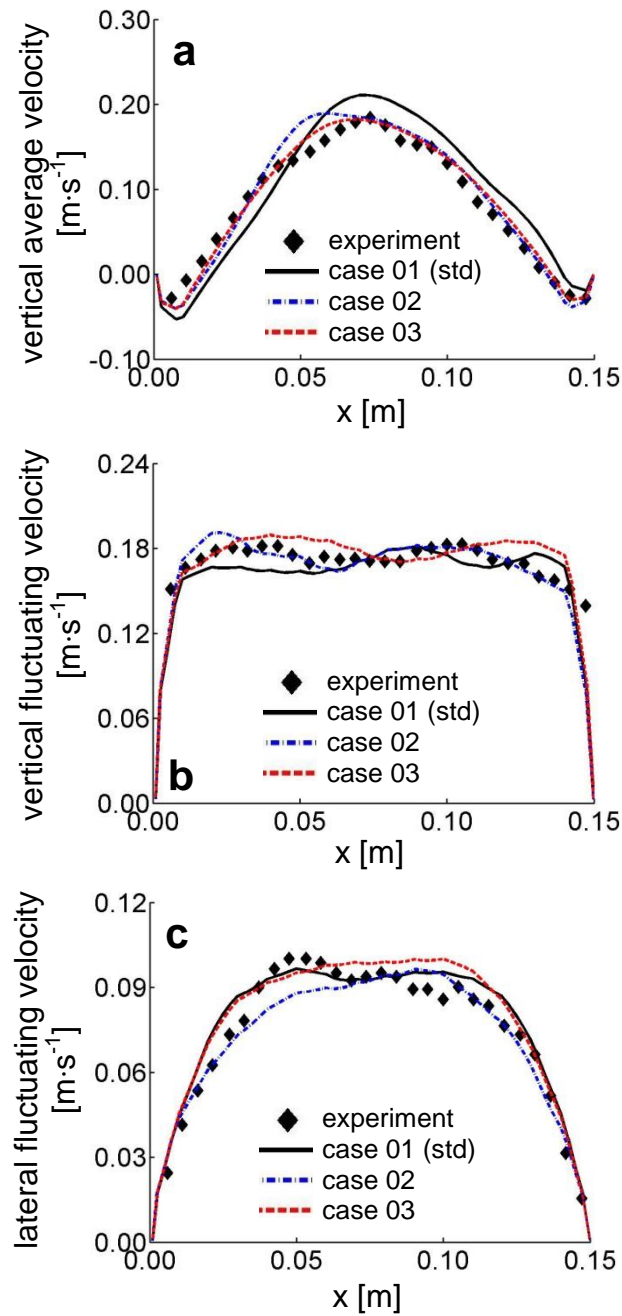


Figure 3.9: Comparison of (a) the average and (b, c) the fluctuating liquid velocity components for simulations of monodisperse and polydisperse bubble distributions and the experiment performed by [Deen et al. \(2001\)](#) at a column height of 0.255 m and a depth of 0.075 m.

The constants for the bubble break-up and coalescence (B&C) model of [Coulaloglou and Tavlarides \(1977\)](#) were determined by trial and error in some test simulations. In doing so, the bubble size distribution (BSD) was recorded between the column heights of 0.20 m and 0.30 m, accordingly to the experiments of [Hansen \(2009\)](#). The closest match for d_{10} and d_{32} was obtained with the values $C_C=8.0 \times 10^9$, $C_{B1}=3.8$ and $C_{B2}=2.0 \times 10^{-4}$. A detail comparison of

the experimentally and the numerically obtained BSDs is given in the next chapter. By taking into account B&C, the liquid hydrodynamic was predicted best. As shown in Fig. 3.9, the results of case 03 agreed very well with the experimental velocity profiles: Not only the magnitudes and the locations of the average velocity characteristics matched, but also both fluctuating profiles were captured more accurately.

Finally, the mean overall gas hold-up α_G , averaged between 20 s and 180 s, revealed only small deviations: The values of 1.28 %, 1.29 % and 1.25 % were predicted for α_G for the cases 01 to 03, respectively.

3.3.3 Bubble Size Distribution of Case 03

As described above, the experimentally obtained BSD from Hansen has been used as reference for the determination of the B&C model constants. Despite best efforts, it was not possible to preserve the experimental BSD. Therefore, the main focus was put on the concurrence of the arithmetic mean diameter d_{10} (model: 2.20 mm, experiment: 2.26 mm, relative deviation: 2.7 %), while the Sauter mean diameter d_{32} was treated secondarily (model: 3.44 mm, experiment: 5.94 mm, relative deviation: 42 %). Fig. 3.10 illustrates both BSDs, the one predicted by case 03 within 20 s and 180 s and the one measured by Hansen. As one can see, both distributions had a positive skewness, but the experimental result was more leptokurtic and possessed a small number of bubbles with diameters larger than 9 mm. The latter fact was the reason for the discrepancy of the d_{32} values.

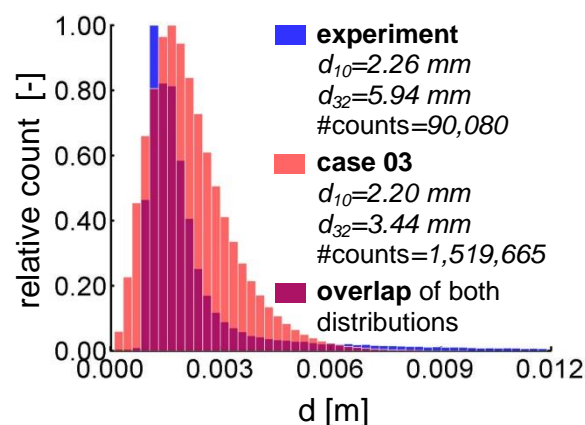


Figure 3.10: Comparison of simulation results (case 03) and experimentally measured bubble number distribution (Hansen, 2009) within the column heights of 0.2 m and 0.3 m.

3.3.4 Absorption of CO_2 in Water (Cases 04-07)

Next, the influence of bubble shrinkage (BS) and B&C on the CO_2 absorption in water was investigated. Therefore, all four possible combinations of BS and B&C were compared. These combinations also included physically unreasonable settings, in order to assess the impact of the particular phenomena on interphase mass transfer and liquid hydrodynamics. In case 04, bubbles with constant diameters of 4 mm were considered, while the bubbles in case 05 shrank due to mass transfer. B&C in case 06 and 07 generated polydisperse bubble swarms, and BS was incorporated in the latter simulation. The top part in Fig. 3.11 shows the total amount of transferred CO_2 for the case of absorption: Clearly, the simulations without BS (cases 04 and 06) revealed higher values of transferred CO_2 than the ones without. Besides this fact, whether BS was considered or not, the simulations with B&C (cases 06-07) predicted higher amounts of transferred CO_2 than the ones without B&C (cases 04-05). After a simulation time of 140 s, the difference in mass transfer between case 05 and 06 constituted 25 %, related to the former.

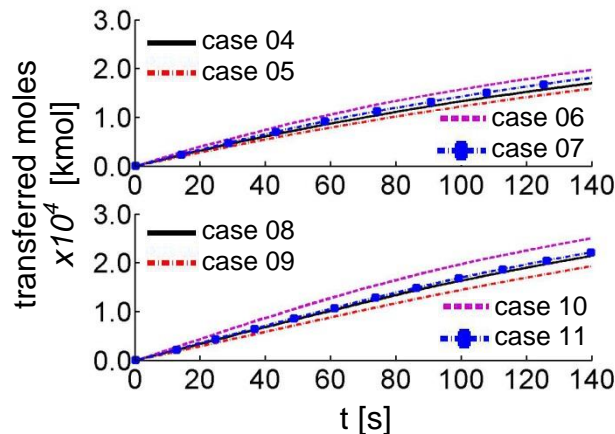


Figure 3.11: Total amount of transferred CO_2 over the time for absorption in water (top part) and for chemisorption in a $NaOH$ solution of pH 12.0 (bottom part).

The interphase mass transfer in the BC is proportional to the specific interfacial area a , and hence can be estimated for spherical bubbles via:

$$a = \frac{6\alpha_G}{d_{32}}, \quad (3.24)$$

The time-averaged values for α_G , d_{32} and a in Tab. 3.5 reveal, that the higher values for \bar{a} in simulations with B&C were attributed to lower values for \bar{d}_{32} , which more than compensated

the drop in $\bar{\alpha}_G$. Furthermore, the information provided in Tab. 3.5 shows that BS causes a reduction of \bar{d}_{32} from 4 mm to 3.88 mm for case 05. However, for case 07 the \bar{d}_{32} increased despite BS was considered from 3.03 mm (case 03, with air) to 3.32 mm, which can be attributed to changed liquid properties in B&C model. The \bar{d}_{10} decreased from 1.91 mm (case 03) to 1.73 mm (case 07). This fact can be explained with the appearance of a small number of big bubbles due to coalescence, while most of the bubbles shrank due to BS. Similarly, for case 06, the \bar{d}_{32} increased to 3.40 mm while the \bar{d}_{10} remained almost unaffected with 1.89 mm as result of the absence of BS.

Table 3.5: Summary of the time-averaged overall gas hold-up α_G , arithmetic mean diameter d_{10} and Sauter mean diameter d_{32} of various simulations. The averaging procedure has been started after 20 s and persisted for the remaining simulation. The specific interfacial area a is calculated from these mean values. Complementary, case 01: $\bar{\alpha}_G=1.28$ %; case 02: $\bar{\alpha}_G=1.29$ %; case 03: $\bar{\alpha}_G=1.25$ %, $\bar{d}_{32}=3.03$ mm and $\bar{d}_{10}=1.91$ mm.

	case	$\bar{\alpha}_G$	\bar{d}_{32}	\bar{d}_{10}	\bar{a}	case	$\bar{\alpha}_G$	\bar{d}_{32}	\bar{d}_{10}	\bar{a}
	[-]	[%]	[mm]	[mm]	[m ² ·m ⁻³]	[-]	[%]	[mm]	[mm]	[m ² ·m ⁻³]
	no BS & no B&C					no BS & with B&C				
absorption	04	1.29	4.00	4.00	19.39	06	1.25	3.40	1.89	22.02
pH 12.0	08	1.31	4.00	4.00	19.64	10	1.24	3.38	1.89	21.98
pH 12.5	–	–	–	–	–	–	–	–	–	–
pH 13.0	–	–	–	–	–	–	–	–	–	–
pH 13.5	16	1.29	4.00	4.00	19.36	18	1.22	3.38	1.94	21.68
pH 14.0	20	1.27	4.00	4.00	19.12	22	1.22	3.49	2.00	21.05
	with BS & no B&C					with BS & with B&C				
absorption	05	1.12	3.82	3.81	17.53	07	1.06	3.32	1.73	19.19
pH 12.0	09	1.06	3.75	3.73	16.87	11	0.98	3.22	1.59	18.22
pH 12.5	12	1.03	3.74	3.71	16.59	13	0.98	3.33	1.67	17.58
pH 13.0	14	0.93	3.62	3.56	15.36	15	0.86	3.26	1.56	15.86
pH 13.5	17	0.55	3.24	2.88	10.02	19	0.53	3.18	1.34	10.05
pH 14.0	21	0.27	3.03	1.91	5.27	23	0.30	3.46	1.43	5.24

The impact of CO_2 absorption on the liquid average velocities, determined between 20 s and 180 s, is shown in Fig. 3.12. The standard case (without absorption) served as a reference. A comparison of the cases 04 and 05 revealed only a minor influence of BS on the liquid flow characteristics. The predicted maximum of case 07 was the lowest and its profile showed a slight shift towards right.

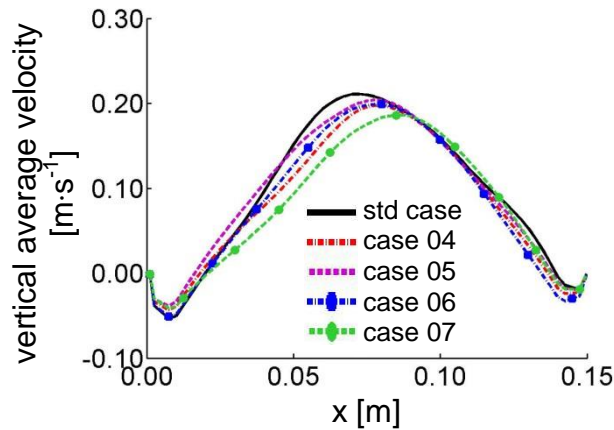


Figure 3.12: Comparison of the time-averaged vertical liquid velocity for CO_2 absorption in water at a column height of 0.255 m and a depth of 0.075 m .

3.3.5 Chemisorption of CO_2 in a $NaOH$ Solutions with $pH\ 12.0$ (Cases 08-11)

The CO_2 chemisorption in a comparably dilute $NaOH$ solution is investigated in this chapter. Fig. 3.13 shows the temporal evolution of the chemical species during chemisorption in a $NaOH$ solution of $pH\ 12.0$. At the beginning of the chemisorption process, the dissolved $CO_2(aq)$ reacted to the intermediate product CO_3^{2-} by consuming OH^- ions. The drop in the OH^- concentration led to a shift in the pH , causing the intermediate product to be converted to HCO_3^- . After around 75 s , only HCO_3^- was present and the amount of dissolved CO_2 increased more rapidly, indicating that all reactions were completed.

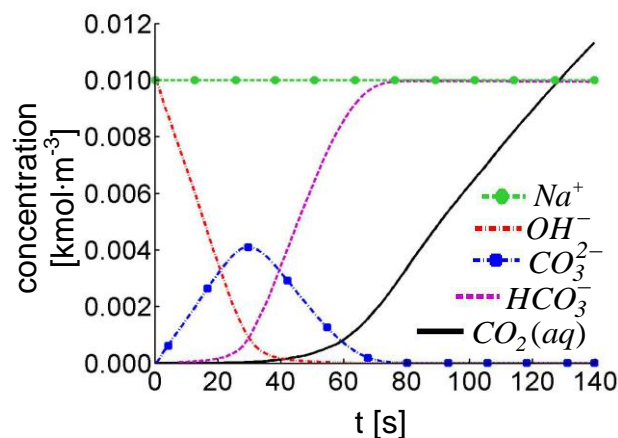


Figure 3.13: The temporal evolution of the volume-averaged species concentrations during chemisorption of CO_2 in a $NaOH$ solution initially at $pH\ 12.0$ (case 08).

This spatial aspect of the reaction is depicted in Fig. 3.14 by a series of snapshots after 20 s for the midplane of the BC. Thereby, Fig. 3.14(a) illustrates the positions of the bubbles while Figs. 3.14(b) indicates the liquid velocity. As shown in Fig. 3.14 (c), the concentration of $CO_2(aq)$ had its maximum in the region around the sparger, which is explained by the locally high gas volume fraction (i.e. high CO_2 transfer rate) and the lower pH value. Under these conditions CO_3^{2-} and HCO_3^- are formed, shifting the equilibrium towards $CO_2(aq)$. Inasmuch as the bubble plume expanded radially with increasing reactor height, the local gas fraction decreased. Hence, dissolved CO_2 was mixed with the reactant OH^- and quickly reacted, resulting in a decrease of both species. The opposite effect, an increase of concentration with the reactor height, was observed for the reaction products CO_3^{2-} and HCO_3^- , as shown in Figs. 3.14(e)-(f). Clearly, these results indicate that the assumption of a well-mixed BC was not justified and that the local concentrations should be taken into account for prediction integral reaction rates.

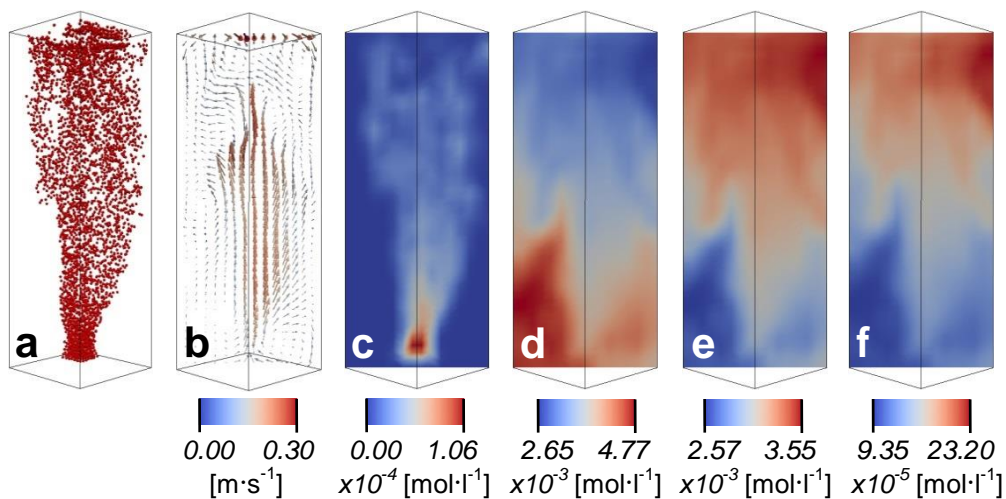


Figure 3.14: Snapshots of CO_2 chemisorption in a $NaOH$ solution of pH 12.0 after 20 s (case 08). The pictures show (a) the bubbles' positions, (b) the liquid velocity, (c) the $CO_2(aq)$ concentration, (d) the OH^- concentration, (e) the CO_3^{2-} concentration and (f) the HCO_3^- concentration.

The lower part of Fig. 3.11 shows the integral amount of CO_2 transferred to the liquid phase for the chemisorption of CO_2 in a $NaOH$ solution with pH 12.0. Again, the simulations with B&C (cases 10-11) indicated increased values of transferred CO_2 compared to the cases without B&C (cases 08-09). After 140 s, the cases 09 and 10 differed up to 32 %, whereby 1.9×10^{-4} kmol and 2.5×10^{-4} kmol of CO_2 were transferred. As expected, a comparison of the

graphs for absorption and chemisorption revealed higher interphase mass transfers for the latter. Clearly, in contrast to the increase in concentration of $CO_2(aq)$ during absorption, $CO_2(aq)$ is consumed during chemisorption by liquid phase reactions. This led to a higher concentration difference between the gas and the liquid phase in the reactive case and ultimately to a higher mass transfer rate. Besides, BS in the case of chemisorption in a $NaOH$ solution with pH 12.0 showed the same impact as B&C events.

The consequences of the different bubble treatments on the temporal evolution of the pH value are shown in Fig. 3.15. While the lowering of the pH below the value 7 took 65 s in the simulation with B&C but without BS (case 10), 93 s were necessary in the simulation neglecting B&C but considering BS (case 09). Thus, when accounting for B&C, a substantial decrease in the order of 40 % of the predicted reaction time was observed. This clearly indicated the need to account for these models when predicting reactor performance.

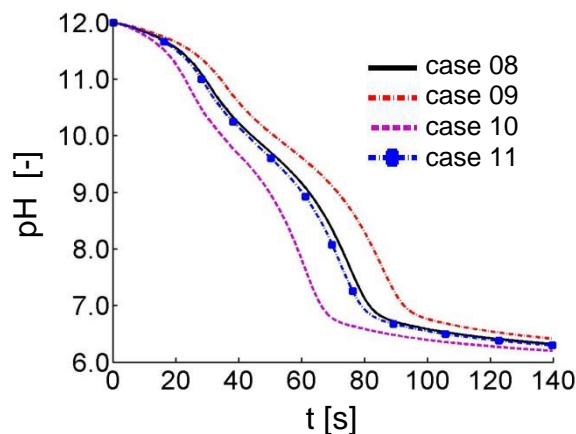


Figure 3.15: The temporal evolution of the pH value during CO_2 chemisorption in a $NaOH$ solution of pH 12.0.

In order to complete the picture of the response of chemical reactions on B&C model details, the (domain-averaged) concentration of the intermediate product CO_3^{2-} is shown in Fig. 3.16. As example, a duration of 90 s was necessary for the CO_3^{2-} concentration to drop below $10^{-5} \text{ kmol m}^{-3}$ in case 09. This concentration was obtained already after 64 s in case 10.

Compared to the CO_2 absorption, the cases with chemisorption caused only a small reduction of the gas hold-ups: in simulations without B&C, α_G dropped by 0.06 % to 1.06 % (case 09), while in case 11, α_G dropped by 0.08 % to 0.98 %. Also, the results in Tab. 3.5 show only an insignificant reduction of d_{32} and d_{10} compared to the cases with absorption. Due to the

comparably short reaction phase in a NaOH solution of pH 12.0, BS was insignificant and liquid velocity profiles change only little. However, this situation is expected to change in case of NaOH solutions with initially higher pH. In the next chapter, substantial BS is considered which is expected at the very beginning of the chemisorption simulations.

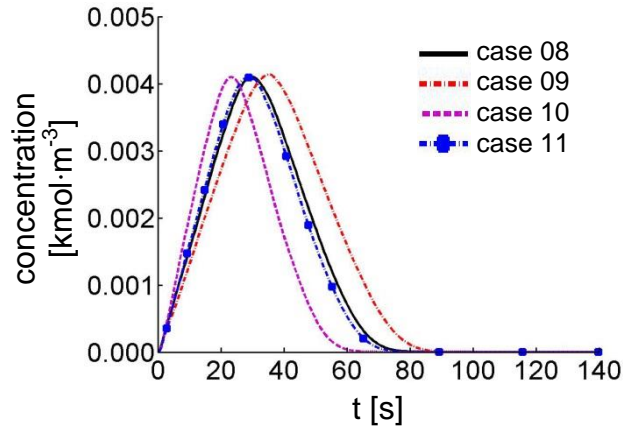


Figure 3.16: The temporal evolution of the CO_3^{2-} concentrations during CO_2 chemisorption in a NaOH solution of pH 12.0.

3.3.6 Chemisorption of CO_2 in NaOH Solutions with pH between 12.5 and 14.0

In order to give an impression of the appearance of the bubble plumes during CO_2 chemisorption in NaOH solutions with different initial pH, a series of snapshots is shown in Fig. 3.17. The snapshots, taken after 20 s, reveal a visually noticeable decrease of the gas phase concentration in the upper column half for pH 13.0. This effect became stronger for pH 13.5, and finally at pH 14.0, only small bubbles were able to reach the top of the BC. Accordingly, the time-averaged gas hold-ups (summarized in Tab. 3.5) reflected this decrease of the gas phase concentration: for the cases without B&C, $\bar{\alpha}_G$ continuously dropped from 1.06 % at pH 12.0 (case 09) to 0.27 % at pH 14.0 (case 21). The $\bar{\alpha}_G$ in the cases with B&C followed this trend and decreased from 0.98 % (case 11) to 0.30 % (case 23).

The vertical decrease of the bubble diameter is illustrated in Fig. 3.18, which shows the chronological progression of the Sauter mean diameters at various heights for pH 14.0. Clearly, when the B&C model was not applied (case 21, see left part in Fig. 3.18), the d_{32} shrank with increasing reactor height to approximately 0.9 mm at 0.40 m. This was 1/88 of the

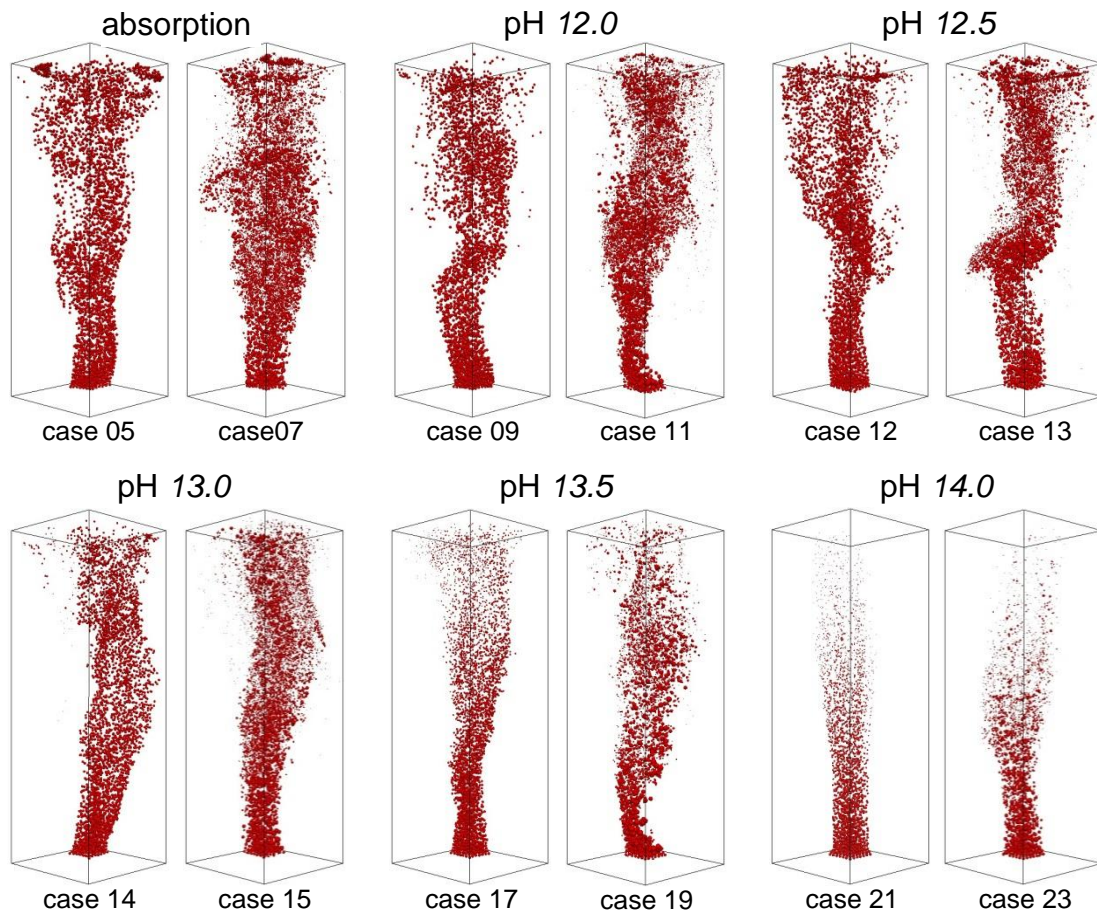


Figure 3.17: Snapshots of the CO_2 absorption in water and CO_2 chemisorption in $NaOH$ solutions of different pH after 20 s. The left image of each pH shows simulations without consideration of B&C, the right side with B&C.

bubbles' initial volume. At two instances of time during the simulation, the bubbles were already completely dissolved at this height. Moreover, the figure indicates that the rate of BS decreased with increasing height. This finding is explained by a lower concentration gradient of CO_2 in the upper column region: the liquid reactant OH^- was already consumed by the ascending bubbles. Consequently, the local $CO_{2(aq)}$ concentration rose, causing a lower CO_2 concentration gradient between the phases. Ultimately, this resulted in a deceleration of the mass transfer rate with increasing height. Additionally, the figure indicates a temporal increase of the d_{32} , which is explained by the temporally decreasing total OH^- concentration in the BC.

Finally, considering the case with B&C (see right part in Fig. 3.18), a drastic increase of the temporal fluctuation of d_{32} at all heights in the reactor was observed. This was expected, since not only the fluctuations in the flow field and due to BS cause these fluctuations, but also discrete B&C events. Also, B&C events led to a clear shift towards a larger mean bubble size.

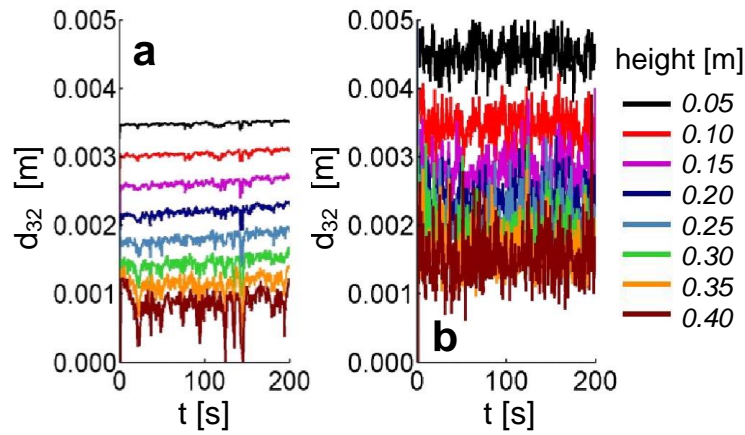


Figure 3.18: The temporal evolution of the Sauter mean diameters during CO_2 chemisorption in a $NaOH$ solution of pH 14.0 at various column heights (a) without B&C (case 21) and (b) with B&C (case 23).

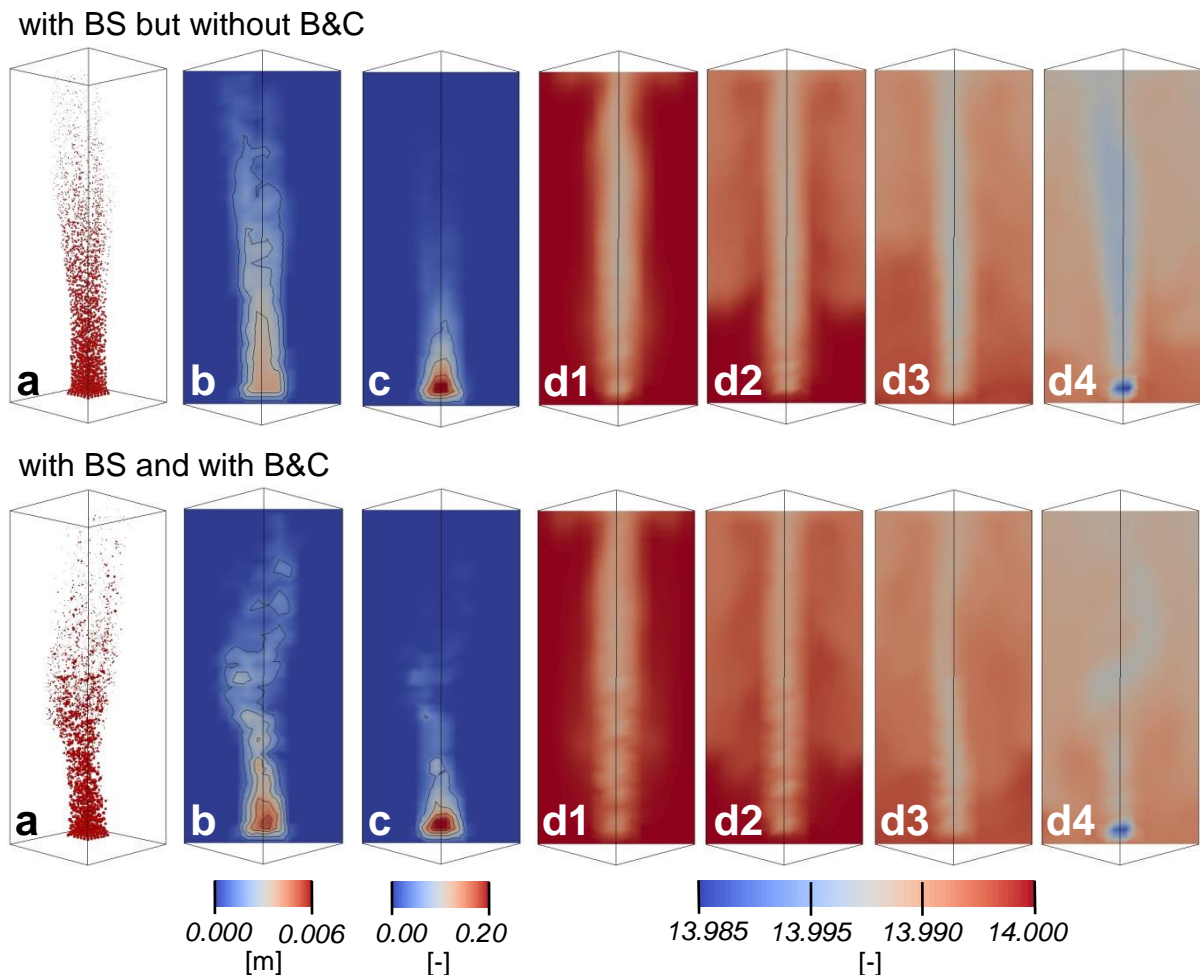


Figure 3.19: Instantaneous snapshots of the CO_2 chemisorption in a $NaOH$ solution with pH 14.0 without B&C (case 21) and with B&C (case 23). Snapshots taken after 20 s show (a) the bubbles' positions, (b) the Sauter mean diameters and (c) the gas hold-up. The images (d1)-(d4) illustrate the temporal evolution of the pH value for 5 s, 10 s, 15 s and 20 s.

In contrast to case 21, the B&C model in Fig. 3.18(b) resulted in an increase of the Sauter mean diameter up to 4.6 mm shortly above the sparger. Between a height of 0.05 m and 0.10 m , the number of bubble breakage events seemed to overwhelm the coalescence events, resulting in a drop of d_{32} to 3.5 mm . The spatial distributions of the B&C events that occurred during the simulation are shown in Fig. 3.20. For heights above 0.10 m , the figure indicates a decreasing shrinkage rate of the Sauter mean diameter. The reason for this was again the lower OH^- concentration in the upper reactor region, as shown in Fig. 3.19 for case 23. However, at some times the d_{32} observed in the upper region of the reactor was higher than the d_{32} observed in the lower regions.

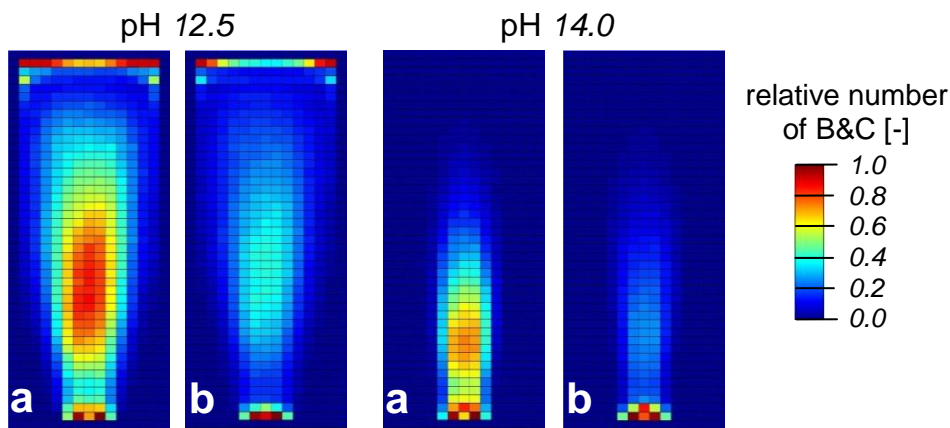


Figure 3.20: The normalized number of (a) breakage and (b) coalescence events occurring during CO_2 chemisorption in NaOH solutions of pH 12.5 (case 13) and pH 14.0 (case 23).

Despite of the major impact on the vertical BSD, the B&C model unveiled a surprisingly insignificant consequence on the interphase mass transfer rate. Due to the large dissolution rate at pH 13.5 and 14.0 , the mass transfer rate was not sensitive to B&C events: As shown in the top part of Fig. 3.21, the values of transferred CO_2 after 200 s amounted to be $7.5 \times 10^{-4}\text{ kmol}$ without B&C (case 17) and $7.8 \times 10^{-4}\text{ kmol}$ when the B&C model was applied (case 19). At pH 14.0 , the amount of transferred CO_2 from the injected bubbles nearly reached its theoretical maximum, so that nearly all bubbles were completely dissolved. Using the molar gas volume of $24.5 \times 10^{-4}\text{ kmol}\cdot\text{m}^{-3}$ (Hucknall, 1991), the total amount of injected CO_2 was $9.0 \times 10^{-4}\text{ kmol}$ after 200 s . The simulations predicted the values of $8.9 \times 10^{-4}\text{ kmol}$ (case 21) and $8.6 \times 10^{-4}\text{ kmol}$ (case 23) which indicated a consumption of 99% and 96% , respectively.

Furthermore, the differences of the transferred moles for the cases with and without BS deviated dramatically. For the latter unphysical case, the amount of transferred CO_2 was twice (at pH 13.5) or even 3.5 times higher (at pH 14.0).

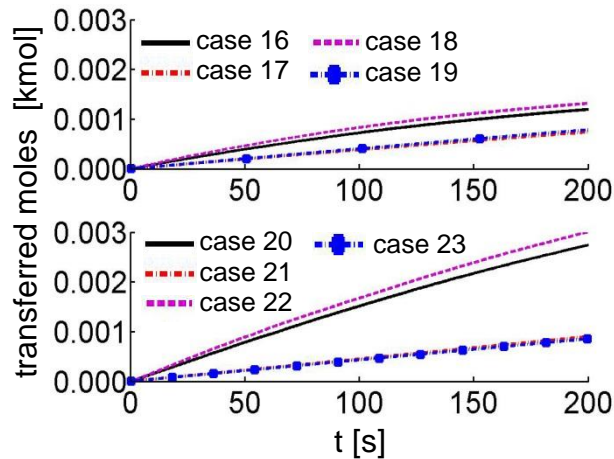


Figure 3.21: Sum of interphase transferred CO_2 over the time for chemisorption in $NaOH$ solutions of pH 13.5 (top) and pH 14.0 (bottom).

The impact of different bubble treatment on the liquid hydrodynamics is depicted in Fig. 3.22. As can be seen, the average liquid velocity in the simulations without B&C seemed to be nearly unaffected for the cases with pH 12.5 to 13.5. The vertical fluctuations were predicted to continually decrease with increasing pH, especially towards the walls. A reduction of the fluctuations in the lateral direction was also predicted. Both aspects indicated a lower tendency for the bubble plume to oscillate with increasing dissolution rate. For the simulation with pH 14.0, the maximum of the average velocity showed a significant increase, while the profile itself became narrower. The simulations applying the B&C model showed distinct changes of the average velocities already at lower pH. As expected, the discrepancy was most pronounced at pH 14.0 due to almost complete dissolution of bubbles in the upper section of the reactor. In parallel to the cases without B&C, the vertical and lateral fluctuations decreased continuously and the profile became narrower too.

Next, the progression of the overall gas hold-up and the Sauter mean diameter is illustrated as function of the pH. Thereby, the graphs were obtained by combining the simulation results for CO_2 chemisorption in $NaOH$ solutions with a pH between 12.0 and 14.0. As depicted in Fig. 3.23, the simulations neglecting B&C possessed nearly constant α_G values of 1.03 % up to pH 12.5. Thereafter, α_G dropped almost linearly down to 0.24 % at pH 14.0. In comparison, the cases considering B&C showed a lower gas hold-up of approximately 0.96 % till pH 12.4. The enhanced dissolution of the gas bubbles caused a decrease of α_G down to 0.28 % at pH 14.0. Around pH 13.6, the predicted α_G values of both methods were identical. In summary, the decrease of α_G with pH is more pronounced compared the B&C model.

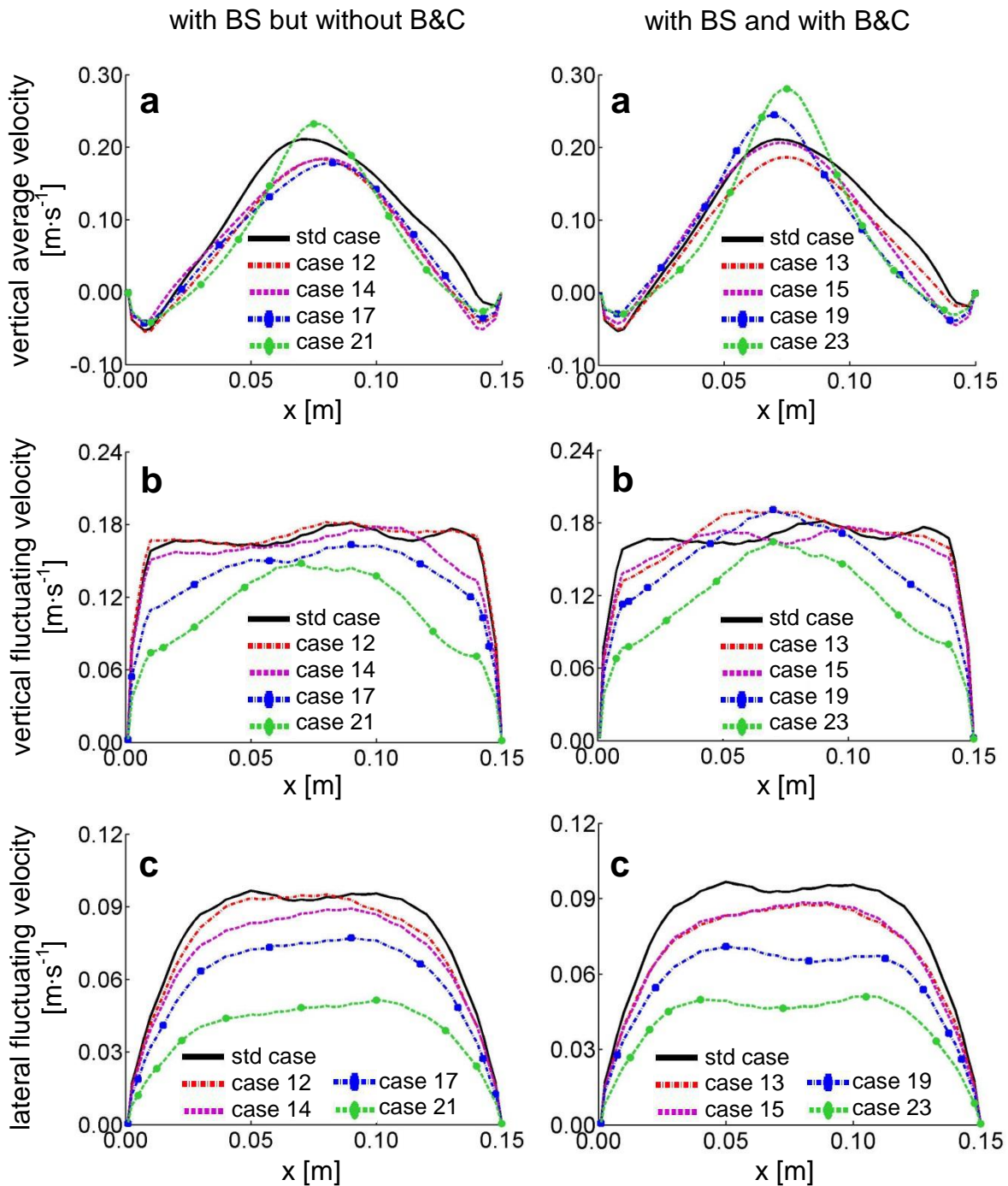


Figure 3.22: Comparison of the average (a) and the fluctuating (b, c) liquid velocity components for CO_2 chemisorption in NaOH solutions with a pH between 12.5 and 14.0 at a column height of 0.255 m and a depth of 0.075 m. The left parts show characteristics for simulations without B&C, while the right show characteristics with consideration of B&C.

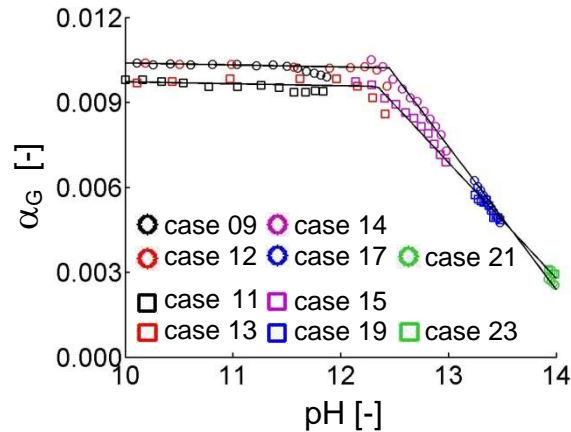


Figure 3.23: The overall gas hold-up during CO_2 chemisorption in $NaOH$ solutions as function of the pH. The solid lines represent trendlines for chemisorption with (squares) and without (circles) B&C.

Finally, the d_{32} at various reactor heights is shown as function of the time. For a clear representation, the Sauter mean diameter is represented in dimensionless form using the ratio of the current reactor height and d_{32} . As illustrated in Fig. 3.24 for the cases without B&C, the d_{32} remained nearly constant up to pH 12.5. For higher pH values the d_{32} strongly decreased, which was indicated by a step increase of the dimensionless quantity. The vertical decrease of the d_{32} at a certain pH followed the same trend as illustrated in Fig. 3.18. This was also valid for the simulations in which the B&C model is applied.

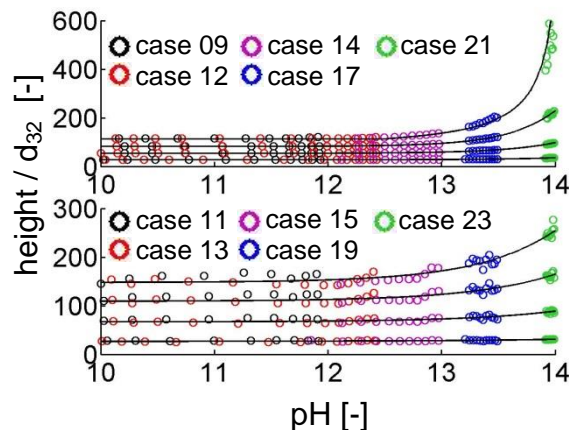


Figure 3.24: The ratio of the current reactor height and the Sauter mean diameter during CO_2 chemisorption in $NaOH$ solutions as a function of the pH. The images show chemisorption without B&C (top) and with B&C (bottom). The Sauter mean diameters are measured at column heights of 0.1 m (lowest trendlines), 0.2 m , 0.3 m and 0.4 m (topmost trendlines).

3.4 Summary and Conclusions

The impact of break-up and coalescence (B&C) events on the flow and concentration profiles in a small bubble column (BC) was studied. Specifically the model of [Coulaloglou and Tavlarides \(1977\)](#) was used, and the implementation followed the stochastic approach detailed in [Gruber et al. \(2013\)](#). Multiphase flow and species transport was numerically investigated using an Euler-Lagrange approach. Besides the absorption of CO_2 in water, the chemisorption of CO_2 in $NaOH$ solutions with a pH between 12.0 and 14.0 was chosen as model reaction. Thereby, the kinetic reaction models described in [Darmana \(2006\)](#) were utilized in this work.

As reference case the well-documented rectangular laboratory-scale BC of [Deen et al. \(2001\)](#) was used. The validation of the liquid hydrodynamics showed excellent agreement concerning the average and fluctuating velocity profiles. Moreover, the implementation of all relevant models and algorithms was verified by considering test cases for liquid phase mixing, interphase mass transfer, and bubble shrinkage (BS). Finally, the model constants for the B&C model were calibrated based on the bubble size distribution (BSD) experimentally measured by [Hansen \(2009\)](#). Unfortunately, a full match of the numerically and experimentally obtained BSDs was not possible. Hence, the focus was put on the arithmetic mean bubble diameter d_{10} (model: 2.20 mm, experiment: 2.26 mm), while the Sauter mean diameter d_{32} was treated to be of secondary importance (model: 3.44 mm, experiment: 5.94 mm). The reason for this is that only a small number of extremely large bubbles was observed in the experiment, which was not predicted by the numerical simulations. One can only speculate that the inability to predict these extremely large bubbles was due to the assumption of bubbles to be rigid spheres. This assumption clearly breaks down for the almost centimeter-sized bubbles observed by [Hansen \(2009\)](#). Consequently, the collision rates and hence the coalescence frequency were underpredicted, mainly due to the assumption of undeformed spheres in this simulations.

First, the CO_2 absorption in water was investigated: Due to higher interfacial areas a , the cases with B&C showed a higher amount of dissolved CO_2 (see Fig. 3.11) compared to that without B&C. However, whether B&C was applied or not, the absorption had only minor impact on the average liquid velocities (see Fig. 3.12), the overall mean gas hold-up $\bar{\alpha}_G$ and the overall mean \bar{d}_{32} (see Tab. 3.5). For CO_2 chemisorption in a $NaOH$ solution of pH 12.0,

similar results as for the absorption were obtained (see Fig. 3.11 and Tab. 3.5). Moreover, the impact of different BSDs on the temporal evolution of the reaction showed significant differences, as shown in Figs. 3.15 and 3.16.

With increasing concentration of the *NaOH* solution, i.e. increasing the *pH* from 12.0 to 14.0, the gas hold-up $\bar{\alpha}_G$ decreased from typically 1.06 % (without B&C; 0.98 % were observed with B&C) to approximately 0.3 %. The \bar{d}_{32} in simulations neglecting B&C continuously shrank within this *pH* range from 3.75 mm to 3.03 mm. In contrast, the \bar{d}_{32} in simulations applying the B&C model increased moderately from 3.22 mm to 3.46 mm. The reason for this is the large number of bubble coalescence events right above the gas sparger, as shown in Fig. 3.18. However, along with the *pH* increase, the differences between simulations with and without B&C became smaller: at *pH* 14.0 and after 200 s of gas injection, the predicted amount of transferred moles *CO*₂, namely 8.9×10^{-4} kmol (without B&C) and 8.6×10^{-4} kmol (with B&C), lay close to the theoretical limit of 9.0×10^{-4} kmol. Thus, in the extreme situation of fast chemisorption and hence almost complete dissolution of the injected gas, B&C did not play a significant role.

Finally, the impact of B&C on the liquid hydrodynamics during chemisorption was investigated, as shown in Fig. 3.22. While the average liquid velocity between *pH* 12.5 and 13.5 in simulations without B&C seemed nearly unaffected, its maxima in the simulation with B&C continually increased and the velocity profiles became narrower. At *pH* 14.0, all maxima of the mean liquid velocity showed an (further) increase. Whether B&C was incorporated or not in the simulations, the vertical and lateral fluctuation continually decreased with increasing *pH*. This was due to the lower amount of liquid phase agitation as a result of the decrease in bubble size with increasing *pH*. Thus, while the modeled BS became essential, the effect of B&C events gradually decreased for fast reactions in which bubbles were almost completely dissolved.

3.5 Appendix

A Bubble Dispersion Model (Langevin Model)

For the generation of the instantaneous liquid velocity along bubble trajectory, the so-called Langevin equation model is used: The liquid velocity fluctuation at the new bubble position $\mathbf{u}_L'(t^{n+1})$ is related with the fluctuation at the old position $\mathbf{u}_L'(t^n)$ through a correlation function $\mathbf{R}_B(\Delta t, \Delta \mathbf{r})$ in the following way:

$$\mathbf{u}'_{L,i}(t^{n+1}) = R_{B,i}(\Delta t, \Delta \mathbf{r}) \mathbf{u}'_{L,i}(t^n) + \sigma_{sgs} \sqrt{1 - R_{B,i}^2(\Delta t, \Delta \mathbf{r})} \xi_i(t^n), \quad (\text{A } 3.1)$$

whereby the Gaussian random number $\xi_i(t^n)$ for the spatial direction i has a mean value of zero and a standard deviation of one. The distance $\Delta \mathbf{r}(t^{n+1})$ between a bubble and a fluid element, which shared the same position at the former time $t=t^n$, is given through $\Delta \mathbf{r} = (\mathbf{u}_L(t^n) - \mathbf{u}_B(t^n)) \Delta t$. Furthermore, the correlation function is given by:

$$R_{B,i}(\Delta t, \Delta \mathbf{r}) = R_L(\Delta t) \left[f_i(\Delta \mathbf{r}) \frac{\Delta r_i^2}{\Delta \mathbf{r}^2} + g_i(\Delta \mathbf{r}) \left(1 - \frac{\Delta r_i^2}{\Delta \mathbf{r}^2} \right) \right], \quad (\text{A } 3.2)$$

itself is composed of three auto-correlation functions $R_L(\Delta t) = \exp(-\Delta t/T_L)$, $f_i(\Delta \mathbf{r}) = \exp(-|\Delta \mathbf{r}|/L_{E,i})$ and $g_i(\Delta \mathbf{r}) = (1 - |\Delta \mathbf{r}|/(2L_{E,i}))f_i(\Delta \mathbf{r})$, whereby i denotes the spatial direction. The auto-correlation functions in turn rely on the time scale $T_L = c_T \sigma_{SGS}^2 / \epsilon$ (with $c_T = 0.4$ and $\sigma_{SGS} = (2/3 k_{SGS})^{1/2}$) and on the length scales in stream wise $L_{E,1} = 1.1 T_L \sigma_{SGS}$ and in lateral directions $L_{E,2} = L_{E,3} = 0.5 L_{E,1}$.

B Reaction Model

The calculation of the forward k_f and the backward reaction rate constants k_b is described in the following two sub-chapters.

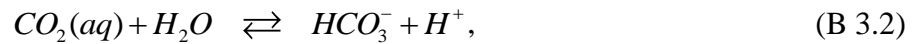
First Reaction (Eq. (3.12))

The $k_{f,I}$ value depends on the ionic strength I of the solution and can be determined via the relation proposed by [Pohorecki and Moniuk \(1988\)](#) as $\log(k_{f,I}/k_{f,I}^\infty)=0.221I-0.016I^2$.

Thereby, the reaction rate $k_{f,I}^\infty$ for infinitely diluted solutions is given by $\log(k_{f,I}^\infty)=11.895-2382/T$. The ionic strength of the electrolyte solution in turn depends on the concentration and the charge number z of the dissolved ions:

$$I = 0.5([\text{Na}^+]z_{\text{Na}^+}^2 + [\text{OH}^-]z_{\text{OH}^-}^2 + [\text{HCO}_3^-]z_{\text{HCO}_3^-}^2 + [\text{CO}_3^{2-}]z_{\text{CO}_3^{2-}}^2). \quad (\text{B } 3.1)$$

Before $k_{b,I}$ can be calculated, the equilibrium constant K_I has to be determined, whereby latter is derived using the equilibrium constants of the following two reactions:



[Edwards et al. \(1978\)](#) and [Tsonopolous et al. \(1976\)](#) determined the relations $\ln(K_3) = -12092.1/T - 36.8\ln(T) + 235.5$ as well as $\log(K_w) = -5839.5/T - 22.5\log(T) + 61.2$ for the equilibrium constants:

$$K_3 = \frac{[\text{HCO}_3^-][\text{H}^+]}{[\text{CO}_2(\text{aq})]}, \quad (\text{B } 3.4)$$

$$K_w = [\text{H}^+][\text{OH}^-]. \quad (\text{B } 3.5)$$

Finally, K_I and $k_{b,I}$ can be calculated via:

$$K_I = \frac{k_{f,I}}{k_{b,I}} = \frac{K_3}{K_w}. \quad (\text{B } 3.6)$$

Second Reaction (Eq. (3.13))

[Eigen \(1954\)](#) determined the value for $k_{f,2}$ to be in the order of 10^{10} to $10^{11} \text{ m}^3 \cdot \text{kmol}^{-1} \cdot \text{s}^{-1}$. Later, [Darmana \(2006\)](#) showed that a reduction of the $k_{f,2}$ value to $10^6 \text{ m}^3 \cdot \text{kmol}^{-1} \cdot \text{s}^{-1}$ (which is still much higher than $k_{f,1}$) only produces a negligible imprecision, but highly improves the performance of the simulation. Further, [Hikita et al. \(1976\)](#) proposed the following $[\text{Na}^+]$ dependent relation for the equilibrium constant K_2 :

$$\log\left(\frac{K_2}{K_2^\infty}\right) = \frac{1.01[\text{Na}^+]^{1/2}}{1+1.27[\text{Na}^+]} + 0.125[\text{Na}^+], \quad (\text{B } 3.7)$$

with $\log(K_2^\infty) = 1568.94/T + 0.4134 - 0.00673T$. Finally, $k_{b,2}$ can be calculated through:

$$K_2 = \frac{k_{f,2}}{k_{b,2}}. \quad (\text{B } 3.8)$$

Notation

Latin Letters

a	specific interfacial area, ($\text{m}^2 \cdot \text{m}^{-3}$)
A	surface area, (m^2)
C	model constant, (–)
C_E, C_K	turbulence model constants, (–)
C_C, C_{B1}, C_{B2}	break-up and coalescence model constants, (–)
C_S	Smagorinsky constant, (–)
d, d_{32}, d_{10}	diameter; Sauter mean diameter; arithmetic mean diameter (m)
D	diffusivity, ($\text{m}^2 \cdot \text{s}^{-1}$)
E	damping factor of the wall function, (–); enhancement factor, (–)
$Eö$	Eötvös number, (–)
$f_i(\Delta \mathbf{r})$	auto-correlation function, (–)
\mathbf{F}	force, ($\text{kg} \cdot \text{m} \cdot \text{s}^{-2}$)
$g_i(\Delta \mathbf{r})$	auto-correlation function, (–)
h_b, h_G	ion- and gas-specific parameters ($\text{m}^3 \cdot \text{kmol}^{-1}$)
h_i, h_g	initial and critical film thickness, (m)
H	Henry constant, (–)
\mathbf{g}	gravitational acceleration, ($\text{m} \cdot \text{s}^{-2}$)
Ha	Hatta number, (–)
I	ionic strength, ($\text{kmol} \cdot \text{m}^{-3}$)
\mathbf{I}	unity tensor, (–)
k_b	backward reaction rate constant, (s^{-1})
k_f	forward reaction rate constant, ($\text{m}^3 \cdot \text{kmol}^{-1} \cdot \text{s}^{-1}$)
k_L	mass transfer coefficient ($\text{m} \cdot \text{s}^{-1}$)
k_{SGS}	sub-grid kinetic energy, ($\text{m}^2 \cdot \text{s}^{-2}$)
K_1, K_2, K_3, K_w	equilibrium constant, ($\text{m}^3 \cdot \text{kmol}^{-1}$); ($\text{m}^3 \cdot \text{kmol}^{-1}$); ($\text{kmol} \cdot \text{m}^3$); ($\text{kmol}^2 \cdot \text{m}^{-6}$)
\dot{m}	mass transfer rate from a single bubble, ($\text{kg} \cdot \text{s}^{-1}$)
M	molar mass, ($\text{kg} \cdot \text{kmol}^{-1}$)
\dot{M}	liquid-side volume averaged mass transfer rate, ($\text{kg} \cdot \text{m}^{-3} \cdot \text{s}^{-1}$)
N, \bar{N}	number, (–); average number, (–)
p	pressure, ($\text{kg} \cdot \text{m}^{-1} \cdot \text{s}^{-2}$)
$P^C(d_{eq})$	coalescence efficiency, (–)
\mathbf{r}	position vector, (m)
$R_B(\Delta t, \Delta \mathbf{r})$	auto-correlation function, (–)
Re	bubble Reynolds number, (–)
S	source term of a specific species in the transport equation, ($\text{kg} \cdot \text{m}^{-3} \cdot \text{s}^{-1}$)
\mathbf{S}	rate of strain, (s^{-1})
Sc	Schmidt number, (–)
Sh	Sherwood number, (–)
t	time, (s)
T	temperature, (K)
\mathbf{u}	velocity, ($\text{m} \cdot \text{s}^{-1}$)

V	volume, (m^3)
Y	mass fraction, (-)
z	ionic charge, (-)

Greek Letters

α	volume fraction, (-)
$\beta^B(d_B, d_B)$	daughter bubble size distribution, (-)
Δ	filter length, cell length, (m)
ϵ	dissipation rate, ($\text{m}^2 \cdot \text{s}^{-3}$)
μ	liquid phase viscosity, ($\text{kg} \cdot \text{m}^{-1} \cdot \text{s}^{-1}$)
ξ	Gaussian random number, (-)
ρ	density, ($\text{kg} \cdot \text{m}^{-3}$)
σ	surface tension, ($\text{kg} \cdot \text{s}^{-2}$)
τ	stress tensor, ($\text{kg} \cdot \text{m}^{-1} \cdot \text{s}^{-2}$)
ν	volume, (m^3)
Φ	volume specific interphase force term, ($\text{kg} \cdot \text{m}^{-2} \cdot \text{s}^{-2}$)
$\omega^B(d_B)$	break-up frequency, (s^{-1})

Subscripts and Superscripts

B	buoyancy
$coll$	collision
D	drag
eff	effective
G	gas phase, bubble
ind	individual
I	induced
key	key value for storage in the collision table
$lagr$	Lagrange
L	continuous phase, liquid, lift
n	normal
nbl	neighbor cell list
P	dispersed phase, solid particle or bubble
S	solid phase, solid particle, Smagorinsky
t	tangential
$term$	terminal
T	turbulent
VM	virtual mass
*	modified

References

- Besbes, S., El Hajem, M., Aissia, H.B., Champagne J.Y., Jay, J., 2015. *PIV measurements and Eulerian-Lagrangian simulations of the unsteady gas-liquid flow in a needle sparger rectangular bubble column*. Chem. Eng. Sci. 126, 560–572.
- Bhat, R.V., 1998. *Mass Transfer Accompanied by Multi-step Reactions and its Application to Gas-Liquid Reactor Design*. PhD Thesis, Universiteit Twente, Enschede, The Netherlands.
- Brauer, H., 1981. *Particle/fluid transport processes*. Progress in Chemical Engineering 19, 81–111.
- Coulaloglou, C.A., Tavlarides, L.L., 1977. *Description of interaction processes in agitated liquid-liquid dispersions*. Chem. Eng. Sci. 32(11), 1289–1297.
- Cussler, E.L., 2007. *Diffusion: Mass Transfer in Fluid Systems*. Cambridge University Press, New York, USA.
- Dani, A., Guiraud P., Cockx, A., 2007. *Local measurement of oxygen transfer around a single bubble by planar laser-induced fluorescence*. Chem. Eng. Sci. 62, 7245–7252.
- Darmana, D., 2006. *On the multiscale modeling of hydrodynamics, mass transfer and chemical reactions in bubble columns*. PhD Thesis, Universiteit Twente, Enschede, The Netherlands.
- Deen, N.G., Solberg, T., Hjertager, B.H., 2001. *Large Eddy Simulation of the Gas–Liquid Flow in a Square Cross-Sectioned Bubble Column*. Chem. Eng. Sci. 56(22), 6341–6349.
- Delnoij, E., Lammers, F.A., Kuipers, J.A.M., van Swaaij, W.P.M., 1997. *Dynamic simulation of dispersed gas-liquid two-phase flow using a discrete bubble model*. Chem. Eng. Sci. 52(9), 1429–1458.
- Dhotre, M.T., Deen, N.G., Niceno, B., Khan, Z., Joshi, J.B., 2013. *Large eddy simulation for dispersed bubbly flows: A review*. International Journal of Chemical Engineering, 1–22.
- Edwards, T.J., Maurer, G., Newman, J., Prausnitz, J.M., 1978. *Vapor-liquid equilibria in multicomponent aqueous solutions of volatile weak electrolytes*. AiChE J. 24(6), 966–976.
- Eigen, M., 1954. *Methods for investigation of ionic reactions in aqueous solutions with half-times as short as 10^{-9} sec. Application to neutralization and hydrolysis reactions*. Discuss. Faraday Soc. 17, 194–205.
- Francois, J., Dietrich, N., Guiraud, P., Cockx, A., 2011. *Direct measurement of mass transfer around a single bubble by micro-PLIFI*. Chem. Eng. Sci. 66, 3328–3338.
- Gruber, M.C., Radl, S., Khinast, J.G., 2013. *Coalescence and Break-Up in Bubble Columns: Euler-Lagrange Simulations Using a Stochastic Approach*. Chem. Ing. Tech. 85(7), 1118–1130.
- Hansen, R., 2009. *Computational and Experimental Study of Bubble Size in Bubble Columns*. PhD Thesis, Aalborg University, Esbjerg, Denmark.

- Hikita, H., Asai, S., Takatsuka, T., 1976. *Absorption of carbon dioxide into aqueous sodium hydroxide and sodium carbonate-bicarbonate solutions*. Chem. Eng. J. 11(2), 131–141.
- Hucknall, D.J., 1991. *Vacuum Technology and Applications*. Butterworth-Heinemann Ltd, Oxford, UK.
- Kantarci, N., Borak, F., Ulgen, K.O., 2005. *Bubble column reactors*. Process Biochem. 40, 2263–2283.
- Krishna, R., van Baten, J.M., Urseanu, M.I., Ellenberger, J., 2001. *Design and scale up of a bubble column slurry reactor for Fischer-Tropsch synthesis*. Chem. Eng. Sci. 56, 537–545.
- Lau, Y.M., Deen, N.G., Kuipers, J.A.M., 2010. *Bubble Breakup in Euler-Lagrangian Simulations of Bubbly Flow*. 7th Int. Conf. on Multiphase Flow (ICMF), Tampa, Florida (2010).
- Monahan, S.M., Vitankar, V.S., Fox, R.O., 2005. *CFD predictions for flow-regime transitions in bubble columns*. AIChE J. 51, 1897–1923.
- Pohorecki, R., Moniuk, W., 1988. *Kinetics of reaction between carbon dioxide and hydroxyl ions in aqueous electrolyte solutions*. Chem. Eng. Sci. 43(7), 1677–1684.
- Pozorski, J., Minier, J.P., 1998. *On the Lagrangian turbulent dispersion models based on the Langevin equation*. Int. J. Multiphase Flow 24(6), 913–945.
- Radl, S., Khinast, J.G., 2010a. *Multiphase Flow and Mixing in Dilute Bubble Swarms*. AIChE J. 56(9), 2421–2445.
- Radl, S., Suzzi, D., Khinast, J.G., 2010b. *Fast Reactions in Bubbly Flows: Film Model and Micromixing Effects*. Ind. Eng. Chem. Res. 49(21), 10715–10729.
- Roghair, I., 2012. *Direct numerical simulations of hydrodynamics and mass transfer in dense bubbly flows*. PhD Thesis, Technische Universiteit Eindhoven, Eindhoven, The Netherlands.
- Smagorinsky, J., 1963. *General Circulation Experiments with the Primitive Equations*. Mon. Wea. Rev. 91(3), 99–164.
- Sommerfeld, M., 2001. *Validation of a Stochastic Lagrangian Modelling Approach for Inter-Particle Collisions in Homogeneous Isotropic Turbulence*. Int. J. Multiphase Flow 27(10), 1829–1858.
- Tomiyama, A., 1998. *Struggle with Computational Bubble Dynamics*. Proc. 3rd Int. Conf. Multiphase Flow (ICMF), Lyon, France.
- Tomiyama, A., Tamai, H., Zun, I., Hosokawa, S., 2002. *Transverse Migration of Single Bubbles in Simple Shear Flows*. Chem. Eng. Sci. 57(11), 1849–1858.
- Tsonopoulos, C., Coulson, D.M., Inman, L.B., 1976. *Ionization constants of water pollutants*. J. Chem. Eng. Data 21(2), 190–193.
- van den Hengel, E.I.V., Deen, N.G., Kuipers, J.A.M., 2005. *Application of Coalescence and Breakup Models in a Discrete Bubble Model for Bubble Columns*. Ind. Eng. Chem. Res. 44(14), 5233–5245.

Versteeg, G.F., van Swaaij, W.P.M., 1988. *Solubility and diffusivity of acid gases (carbon dioxide, nitrous oxide) in aqueous alkanolamine solutions*. J. Chem. Eng. Data 33(1), 29–34.

Weisenberger, S., Schumpe, A., 1996. *Estimation of gas solubilities in salt solutions at temperatures from 273 K to 363 K*. AIChE J. 42(1), 298–300.

Westerterp, K.R., van Swaaij, W.P.M., Beenackers, A.A.C.M., 1994. *Chemical Reactor Design and Operation*. John Wiley & Sons Ltd, New York, USA.

Witz, C., Prakash, A., Khinast, J.G., 2014. *Large Bioreactor Simulation with Graphic Processors*. Proc. 14th AIChE Annual Meeting, Atlanta, USA.

Zhang, D., Deen, N.G., Kuipers, J.A.M., 2007. *Numerical Modeling of Hydrodynamics, Mass Transfer and Chemical Reaction in Bubble Columns*. Proc. 6th Int. Conf. Multiphase Flow (ICMF), Leipzig, Germany.

Zhang, D, Deen, N.G., Kuipers, J.A.M., 2009. *Euler-Euler Modeling of Flow, Mass Transfer, and Chemical Reaction in a Bubble Column*. Ind. Eng. Chem. Res. 48(1), 47–57.

CHAPTER

4

*“Scientists study the world as it is, engineers
create the world that never has been.”*
– Theodore von Karman (1881-1963)

Euler–Lagrange Modeling of Gas–Liquid–Solid Flows³

Abstract

The hydrodynamics of gas-liquid-solid flows are investigated by applying event-driven three-dimensional Euler-Lagrange simulations. Thereby, the focus is put on the modeling of the interaction between ascending gas bubbles and solid particles, which are suspended in a liquid. Specifically, the following approaches are used: (i) coupling via drag force modification (Mitra-Majumdar et al., 1997), (ii) solely elastic collisions, (iii) multistage collisions model (Ralston et al., 1999) and (iv) no interactions between the phases. The setup of the simulations is based on the experimental measurements of Gan (2013), who used a labor-scale cylindrical bubble column, neutrally buoyant acrylic beads of 3 mm in diameter and a solids hold-up of 1.6 vol-%.

³ This chapter is based on: Gruber, M.C., Radl, S., Khinast, J.G., 2015. *Effect of Bubble-Particle Interaction Models on Flow Predictions in Three-Phase Bubble Columns*. Submitted to *Chem. Eng. Sci.*

The results indicate a vertical transport of solid particles from the lowest column quarter towards the upper column region. Furthermore, the effect of the particles on the suspension's viscosity has a significant impact on the local gas hold-up distribution. While the drag force modification model leads to uniform solid hold-ups and lower bubble velocities, the elastic collision model and the multistage collision model showed similar flow predictions. Compared to the experimental measurements of Gan, the velocities at the column's center are underpredicted for the solid phase and overpredicted for the gas phase. This indicates that none of the employed models is able to correctly picture the complex physics in three-phase bubble columns.

4.1 Introduction

Bubble columns (BCs) are very common as three-phase reactors in a variety of industries, such as chemical, petrochemical or biochemical industries. Classical examples for gas-liquid-solid processes in these industries involve the carbonation of lime slurry, the catalytic chlorination of alkenes and the production of penicillin and of citric acid with the aid of microorganisms. The frequent usage of BCs in these and other industrial processes is based on some beneficial characteristics: Compared with other reactor types, BCs possess high heat and mass transfer rates and cause only low operation and maintenance costs due to absence of moving parts (Kantarci et al., 2005; Anil et al., 2007). Also, flotation cells can be seen as three-phase BCs, and their industrial importance for the pulp and paper, as well as the minerals sectors, has stimulated significant research efforts in the past (Koh and Schwarz, 2007; Wang et al., 2010).

Over the last decades, many phenomenological models and empirical correlations have been proposed in literature to quantify three-phase flows in BCs. Most of these models indicate that alongside with the hold-up, various others physical properties of the solid phase (e.g. particle size, particle shape, density) affect the key process parameters (e.g. gas hold-up, terminal rise velocity of the bubbles or size distribution of the bubbles). Most important, it was found that particle parameters also influence flow phenomena like mixing, mass transfer or chemical reactions. Furthermore, the findings of these models and correlations were often ambiguous or even contradictory, which was usually attributed to the complexity of the interactions between the solid and the gas-liquid phases. For instance, many studies concluded that an increase of the solid particle size leads to a decrease of the gas hold-up, while others reported none or even the opposite effect. Furthermore, the validity of these models was often restricted to

similar operating conditions (e.g. reactor dimensions), critically limiting their suitability for reactor design and scale-up (Kantarci et al., 2005; Wang et al., 2007; Rabha et al., 2013).

In recent years, computational fluid dynamic (CFD) has become a powerful tool for engineers, to overcome the drawback of a purely empirical approach, or at least to supplement experimental studies with some mechanistic insight. Clearly, CFD offers the possibility to gain better insights into the complex, often interconnected phenomena in three-phase flows. Generally, two main approaches are used for the modeling of multiphase flows which differ regarding the treatment of the dispersed phases (see the work of Karimi, 2014 for a recent overview).

First, the Euler-Euler (EE) approach treats all phases as interpenetrating continua that are coupled through pressure and interphase exchange coefficients. This approach has been extensively applied with some success, e.g. in the minerals flotation community (Koh and Schwarz, 2008). The EE approach offers the principal advantage of relatively low computational effort and hence, is suited for fitting one or more model parameters to experimental data. Such an approach is often fruitful in the sense of a pragmatic approach to CFD modeling. However, fitted parameters often lack of generality.

Second, the Euler-Lagrange (EL) approach treats the liquid phase as a continuum, while the dispersed phases (solid particles and bubbles) are tracked as discrete particles, whereby an individual force balance equation is solved for each particle. Compared to the EE method, the EL approach requires a smaller number of sub models, since, e.g. particle collisions can be calculated directly. Thus, EL-based simulations offer a more detailed view on events occurring at the scale of the solid particles and bubbles. However, the main drawback of the EL approach is the limitation of the system size, i.e. the number of solid particles and bubbles that can be tracked due to the higher computational costs of this method. Nonetheless, in parallel with the progression in computer technology, the EL approach has been increasingly used for modeling multiphase flows (Zhang and Ahmadi, 2005).

While a bunch of literature exists for EE based simulations of three-phase flows (Darcovic, 1995; Mitra-Majumdar et al., 1997; Padial et al., 2000; Michele and Hempel, 2002; Rampure et al., 2003; Rados et al., 2005; Jia et al., 2007; Koh and Schwarz, 2007, 2008; Anil et al., 2008; Wasewar et al., 2008; Lahiri et al., 2010; Jianping and Shonglin, 2011; Rabha et al., 2013; Silva et al., 2013), only a few number of hybrid EE/EL (Ström et al., 2013) and pure EL based simulations were published in the past. To the authors' best of knowledge, only two

research groups dealt with EL simulations of gas-liquid-solid flows so far.

The first group around Ahmadi and Zhang performed pseudo two-dimensional simulations for a small rectangular BC of the size $25 \times 2 \times 75 \text{ cm}^3$ (Ahmadi and Zhang, 2005; Zhang and Ahmadi, 2005, 2011, 2013). They used neutrally buoyant particles of 0.25 mm in diameter as solid phase and varied the solids hold-up up to 6 vol-\% . The injected air bubbles had an initial diameter of 2 mm which then coalesced during their ascent through the aqueous suspension. In their simulations, Ahmadi and Zhang did not consider interactions between the discrete phases, whether between particles of the same phase nor between different ones. They concluded that at extremely low hold-ups (3 ppm), the solid phase has only little impact on the hydrodynamics, while at higher hold-ups the presence of the solid phase causes larger liquid vortices and increased oscillation of the bubble plume. This in turn causes a reduction of the solid particle concentration in vortical structures and results in an accumulation of the solid particles in areas of high liquid velocity.

Second, the group around Sommerfeld and Bourloutski simulated the hydrodynamics in a cylindrical pilot-scale BC of 63 cm in diameter and of 440 cm in height (Sommerfeld and Bourloutski, 2002; Sommerfeld et al., 2003). They used PMMA particles with a diameter of 3 mm , and air bubbles of 8 mm in diameter for their three-dimensional simulations. A solid and gas hold-up of up to 10 vol-\% and 16 vol-\% was considered in their work. Sommerfeld and Bourloutski observed a considerable suppression of the liquid agitation due to the presence of the particles, as well as an accumulation of the solid particles in the lower half of the BC. After a modification of the drag force coefficients, following the model of Mitra-Majumdar et al. (1997), both the liquid velocity and the spatial distribution of particles, were in better agreement with their experimental data.

All of these previous computational studies were either interesting in qualitative predictions, demonstrated a new computational approach without more in-depth analysis (Ström et al., 2013), or fitted a key model parameter to obtain quantitatively correct predictions (Koh and Schwarz, 2008). This study focuses on a single model, namely the strategy to handle solid particle-bubble collisions, to gain a better understanding of its effect on the predicted flow in a small-scale three-phase BC. Most important, the main interest is put on the quantitative comparison with experimental data, and not on the adjustment of any model parameters for better data fitting.

In the present study, an event-driven three-dimensional EL approach is used to investigate

three-phase flow in a small BC. Since this topic has been disregarded in literature so far, nearly no preliminary work exists. To the authors' best knowledge, this study is the first, which systematically investigates the influence of various solid particle-bubble interaction models on the flow predictions. Specifically, configurations are considered in which (i) the dispersed phases do not interact with each other, (ii) the coupling takes place via drag force modifications as proposed by [Mitra-Majumdar et al. \(1997\)](#), (iii) only elastic collisions take place and (iv) the interaction is modeled using a multistage model which accounts for inelastic collisions as well ([Ralston et al., 1999](#)).

The simulation setup is based on the experimental study of [Gan \(2013\)](#), who used a small cylindrical bubble column, filled with a suspension of neutrally buoyant acrylic beads of 3 mm in diameter and a solids hold-up of 1.6 vol-\% . Interestingly, in the work of Gan, the bubbles were significantly smaller (diameters between 0.7 mm and 2.3 mm) than the suspended solid particles, making this setup an exceptionally challenging one.

4.2 Modeling

4.2.1 Liquid Phase

The liquid phase is assumed to be incompressible and its local hydrodynamics are described through the transient volume-averaged Navier-Stokes equations (NSEs):

$$\frac{\partial(\alpha_L \rho_L)}{\partial t} + \nabla \cdot (\alpha_L \rho_L \mathbf{u}_L) = 0, \quad (4.1)$$

$$\frac{\partial(\alpha_L \rho_L \mathbf{u}_L)}{\partial t} + \nabla \cdot (\alpha_L \rho_L \mathbf{u}_L \mathbf{u}_L) = -\alpha_L \nabla p - \nabla \cdot (\alpha_L \boldsymbol{\tau}_L) + \alpha_L \rho_L \mathbf{g} + \boldsymbol{\Phi}, \quad (4.2)$$

where the liquid (L) properties \mathbf{u} , ρ , p denote the velocity, the density and the pressure, respectively. The solid particles (S) and the bubbles (G) are considered in the above NSEs via the liquid volume fraction α_L and the interphase momentum transfer rate $\boldsymbol{\Phi}$. Thereby, the volume fractions of the three phases satisfy the following compatibility condition:

$$\alpha_L + \alpha_G + \alpha_S = 1. \quad (4.3)$$

The above NSEs are averaged over a representative volume with a typical length larger than the diameters of the bubbles and solid particles. This implies that the large eddy simulation (LES) concept needs to be used to model sub-grid scale turbulent fluid motion. Thereby, only turbulent flow structures are resolved that are larger than the sub grid scale filter length $\Delta = v_{cell}^{1/3}$, while structures smaller than Δ remain unresolved. Consequently, the liquid phase stress tensor $\boldsymbol{\tau}_L$ is modeled via:

$$\boldsymbol{\tau}_L = -\mu_{L,EFF} \left(\left(\nabla \mathbf{u}_L + (\nabla \mathbf{u}_L)^T \right) - \frac{2}{3} \mathbf{I}(\nabla \cdot \mathbf{u}_L) \right), \quad (4.4)$$

with the effective viscosity $\mu_{L,EFF}$ and the unity tensor \mathbf{I} . The effective viscosity is composed of the molecular viscosity μ_L , the sub-grid scale viscosity $\mu_{L,T}$, as well as the eddy viscosity induced by the bubbles $\mu_{G,I}$ and by the solid particles $\mu_{S,I}$:

$$\mu_{L,EFF} = \mu_L + \mu_{L,T} + \mu_{G,I} + \mu_{S,I}. \quad (4.5)$$

The model of [Smagorinsky \(1963\)](#) is used to close the sub-grid scale viscosity:

$$\mu_{L,T} = \rho_L (C_S \Delta)^2 |\mathbf{S}|, \quad (4.6)$$

with \mathbf{S} being the characteristic filtered strain rate, and the Smagorinsky constant C_S (assumed to be equal to 0.1). The enhanced eddy viscosity model due to particle-induced turbulence, proposed by [Sato and Sekoguchi \(1975\)](#), accounts for momentum transfer by wakes of moving particles, whereby $\mu_{G,I}$ and $\mu_{S,I}$ are proportional to the particles' diameters d and slip velocities:

$$\mu_{G,I} = C_\mu \rho_L \alpha_G d_G |\mathbf{u}_G - \mathbf{u}_L|, \quad (4.7)$$

$$\mu_{S,I} = C_\mu \rho_L \alpha_S d_S |\mathbf{u}_S - \mathbf{u}_L|, \quad (4.8)$$

where the model constant C_μ has the value of 0.6 ([Jia et al., 2007](#)).

4.2.2 Dispersed Phases

For the Lagrangian tracking of the dispersed phases, each individual dispersed particle (P), whether gas bubble or solid particle, is assumed to have a spherical shape of constant volume $\nu_P = \pi/6 d_P^3$. The mass $m_P = \rho_P \nu_P$ of each particle is assumed to be concentrated at the position \mathbf{x}_P . Then, a particle's trajectory (i.e. the increment $\Delta \mathbf{x}_P$) and velocity change $\Delta \mathbf{u}_P$ within the time step Δt are calculated with Newton's equation of motion:

$$\Delta \mathbf{x}_P = \mathbf{u}_P \Delta t, \quad (4.9)$$

$$\rho_P \nu_P \Delta \mathbf{u}_P = \Delta t \mathbf{F}_P. \quad (4.10)$$

The net force \mathbf{F}_P , experienced by each individual particle in the presence of the liquid, is composed of the buoyancy force \mathbf{F}_B , the lift force \mathbf{F}_L , the drag force \mathbf{F}_D and the virtual mass force \mathbf{F}_{VM} :

$$\mathbf{F}_P = \mathbf{F}_B + \mathbf{F}_L + \mathbf{F}_D + \mathbf{F}_{VM}. \quad (4.11)$$

The definitions of the forces and of the related closures are summarized in Tab. 4.1. The cross-section area and the particle Reynolds number therein are given by $A_P = \pi d_P^2/4$ and $Re_P = \rho_L |\mathbf{u}_P - \mathbf{u}_L| d_P / \mu_L$, respectively. A thorough discussion of the forces and of their derivation can be found in [Hu \(2005\)](#).

Table 4.1: Forces and closure models for Lagrangian tracking. For bubbles, the drag force coefficient C_D takes the value $C_{D,G}$ while for solid particles it becomes $C_{D,S}$.

Force	Closure
$\mathbf{F}_B = \nu_p(-\nabla p + \rho_p \mathbf{g})$	$C_L = 0.5$
$\mathbf{F}_{VM} = -C_{VM} \rho_L \nu_p \left(\frac{D_p \mathbf{u}_p}{D_p t} - \frac{D_L \mathbf{u}_L}{D_L t} \right)$	$C_{VM} = 0.5$
$\mathbf{F}_D = -\frac{C_D}{2} A_p \rho_L \mathbf{u}_p - \mathbf{u}_L (\mathbf{u}_p - \mathbf{u}_L)$	$C_{D,G} = \begin{cases} 16 \text{Re}_p^{-1} & \text{Re}_p < 1.5 \\ 14.9 \text{Re}_p^{-0.78} & 1.5 \leq \text{Re}_p < 80 \\ 49.9 \text{Re}_p^{-1} (1 - 2.21 \text{Re}_p^{-0.5}) + 1.17 \times 10^{-8} \text{Re}_p^{2.615} & 80 \leq \text{Re}_p < 1530 \\ 2.61 & 1530 \leq \text{Re}_p \end{cases}$
$\mathbf{F}_L = -C_L \rho_L \nu_p (\mathbf{u}_p - \mathbf{u}_L) \times \nabla \times \mathbf{u}_L$	$C_{D,S} = \begin{cases} 24 \text{Re}_p^{-1} (1 + 0.15 \text{Re}_p^{0.687}) & \text{Re}_p < 1000 \\ 0.44 & 1000 \leq \text{Re}_p \end{cases}$

Moreover, to capture the influence of the unresolved sub-grid scale fluid motion on the movement of the dispersed phase, a particle dispersion model (Langevin model) proposed by Sommerfeld et al. (1993) is used in this study. The Langevin model correlates the unresolved fluid motion at the actual position of a particle with the turbulences from its former position. A detailed description of the model along with all governing equations is given in Pozorski and Minier (1998). Finally, the interested reader is referred to the work of Gruber et al. (2013) for an in-depth description of model details (e.g. interpolation of the liquid properties, coupling between continuous and dispersed phases, wall treatment).

4.2.3 Interaction of the Dispersed Phases

For modeling the interactions of the dispersed phases, the hard-sphere model approach is used in this study (Hoomans et al., 1996). Thereby, the time till two particles, which are moving towards each other, collide, is defined by:

$$t_{coll} = \frac{-\Delta \mathbf{x} \Delta \mathbf{u} - \sqrt{(\Delta \mathbf{x} \Delta \mathbf{u})^2 - (\Delta \mathbf{u})^2 \left[(\Delta \mathbf{x})^2 - ((d_1 + d_2)/2)^2 \right]}}{(\Delta \mathbf{u})^2}, \quad (4.12)$$

with the relative velocity $\Delta \mathbf{u} = \mathbf{u}_1 - \mathbf{u}_2$ and the spatial distance $\Delta \mathbf{x} = \mathbf{x}_1 - \mathbf{x}_2$ of the particles. By neglecting the rotation of the particles and assuming that only binary collisions take place, the postcollision velocity of a particle is given through:

$$\mathbf{u}_1^* = \frac{m_1 \mathbf{u}_1 + m_2 \mathbf{u}_2 + m_2 e (\mathbf{u}_2 - \mathbf{u}_1)}{m_1 + m_2}, \quad (4.13)$$

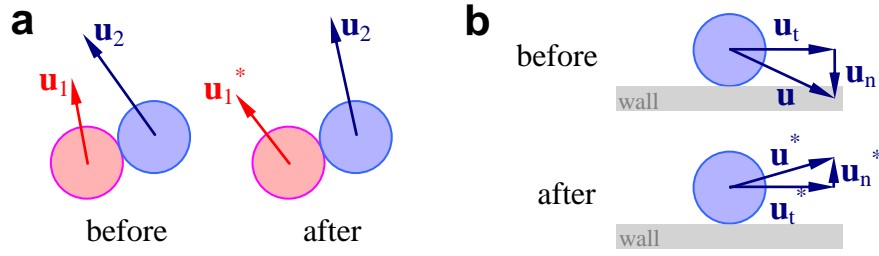


Figure 4.1: Schematic view of the pre- and postcollision (indicated by *) velocities for (a) particle-particle and (b) particle-wall collisions.

with the coefficient of restitution e (see Fig. 4.1). While inelastic bubble-bubble ($e=0.9$) and solid particle-particle ($e=0.9$) collisions are incorporated in every simulation, four different bubble-solid particle interaction models have been considered:

1. *No interaction model (NIM)*: The bubbles and the solid particles do not experience the presence of each other, wherefore overlaps of the two phases occur.
2. *Drag force modification model (DFMM)*: The bubbles and the solid particles experience the presence of the other phase only through a change of the respective drag coefficient (Mitra-Majumdar et al., 1997). Hence, overlaps between particles of different phases can occur in this model as well. Specifically, the modified drag force coefficient for the bubbles is given by:

$$C_D^* = \frac{C_D}{1 - \alpha_s^{0.3}}, \quad (4.14)$$

while the drag force coefficient for the solid particles changes to:

$$C_D^* = C_D (1 - \alpha_G^{0.06}). \quad (4.15)$$

3. *Elastic collision model (ECM)*: A collision between a bubble and a solid particle always results in total elastic rebound ($e=1.0$). This model ensures that no overlaps occur.
4. *Multistage collision model (MCM)*: Depending on the hydrodynamics and on the inertia of the dispersed particles, various interactions can occur (Ralston et al., 1999). As criterion for the type of interaction serves the particle Stokes number:

$$St = \frac{\rho_s |\mathbf{u}_G - \mathbf{u}_s| d_s^2}{9d_G \mu_L}. \quad (4.16)$$

First, for $St < 0.1$, the inertia of the particles (described by a characteristic stopping distance) is small compared to a characteristic time scale for flow around a bubble. In this case, a solid

particle will follow the (complex shaped) fluid streamline around a bubble, and will not collide with the bubble. To avoid the computational cost associated with modeling the small-scale details of particle motion in such a case, the solid particle and the bubble simply penetrate each other without exchanging momentum. Second, for $0.1 \leq St < 3$, a solid particle impacts inelastically on the bubble surface, whereby a major proportion of the kinetic energies gets lost. Since no values were suggested for that case, e is chosen to be 0.4 . Third, for $3 \leq St$, a solid particle's trajectory deviates only slightly from a straight line, and the collision can be considered as quasi-elastic ($e=1.0$).

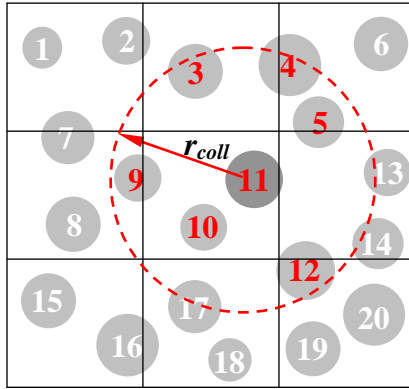
The normal \mathbf{u}_n^* and tangential \mathbf{u}_t^* velocity components for a particle after a wall collision are given by:

$$\mathbf{u}_n^* = -e\mathbf{u}_n, \quad \mathbf{u}_t^* = \mathbf{u}_t. \quad (4.17)$$

As shown in Fig. 4.1, the tangential velocity component remains constant, while the magnitude of the normal velocity component changes proportional to e . This fundamental study focuses on the interactions between bubbles and solid particles in three-phase flow using an event-driven algorithm. This has been done primarily due to efficiency reasons, i.e. to keep the simulation time within a feasible limit. More complex interactions, such as particle-bubble attachment or cluster formation (i.e. enduring particle-bubble interactions), cannot be easily modeled with such an algorithm. Hence, these interactions have not been considered in the present study.

4.2.4 Collision Detection Algorithm

The enormous number of dispersed particles in three-phase systems requires algorithm-based optimization techniques in order to speed up the EL simulations. One strategy to reduce the computational effort for the collision detection was suggested by [Hoomans et al. \(1996\)](#) and is based on neighbor lists. In case the Lagrangian time step is small enough, the spatial region containing potential collision partners for a certain particle can be limited to the neighbor cells of the cell the particle is located in. By applying this technique, a unique lifetime ID-number is assigned to each particle (see Fig. 4.2). At the beginning of Lagrangian tracking, an ID-list is build for each cell. The ID-list contains the IDs of all particles within the particular cell and within its neighbor cells. Consequently, the ID-list contains all potential collision partners for a particle within the particular cell. It should be mentioned that if the Lagrangian time step is



The “particle neighbor cell list” contains ID-numbers of potential collision partners. For a particle in a particular cell, the particle IDs are:

middle cell: 1–20 (all particles),

top left cell: 1–3 and 7–11,

bottom right cell: 10–14 and 17–20.

Using the “collision sphere” technique, only the particles with the IDs 3–5 and 9–12 must be considered for the collision with the particle 11.

Figure 4.2: Schematic representation of the “particle neighbor cell list” and the “collision sphere” technique.

too high or the particles’ diameters are too large, the neighbor cell list should be build with more than one layer of neighbor cells.

For further reduction of the simulation time, [Zeilstra \(2007\)](#) suggested the construction of a collision sphere around each particle that contains its potential collisions partners, as shown in Fig. 4.2. The radius of the collision sphere r_{coll} is calculated with the maximum velocity \mathbf{u}_{max} , the maximum diameter d_{max} of the particles in the neighbor cell list and the time interval Δt_{nbl} in which the neighbor cell list is rebuild:

$$r_{coll} = 2|\mathbf{u}_{max}|\Delta t_{nbl} + d_{max}. \quad (4.18)$$

After the detection of the next occurring collision in the system, all particles are moved on for the collision time t_{coll} . Thereafter, the collision is performed for the two colliding particles (collision pair). In case previous particle position and velocities are not kept in memory, the algorithm will simply continue with collision detection as explained above.

In this study, a technique is presented to overcome these drawbacks, namely the loss of information after collision detection and the movement of all particles before/after each collision (see Fig. 4.3). Based on the work of [Darmana \(2006\)](#), an individual time t_{ind} is introduced for each particle in the system, which is set to zero at the beginning of the Lagrangian tracking with a time step of Δt_{lagr} . The collision times are then calculated for all particles in the system, as described above. If a collision pair fulfills the criterion $t_{key} < \Delta t_{lagr}$, which is given by:

$$t_{key} = t_{coll} + \max[t_{ind,1}, t_{ind,2}], \quad (4.19)$$

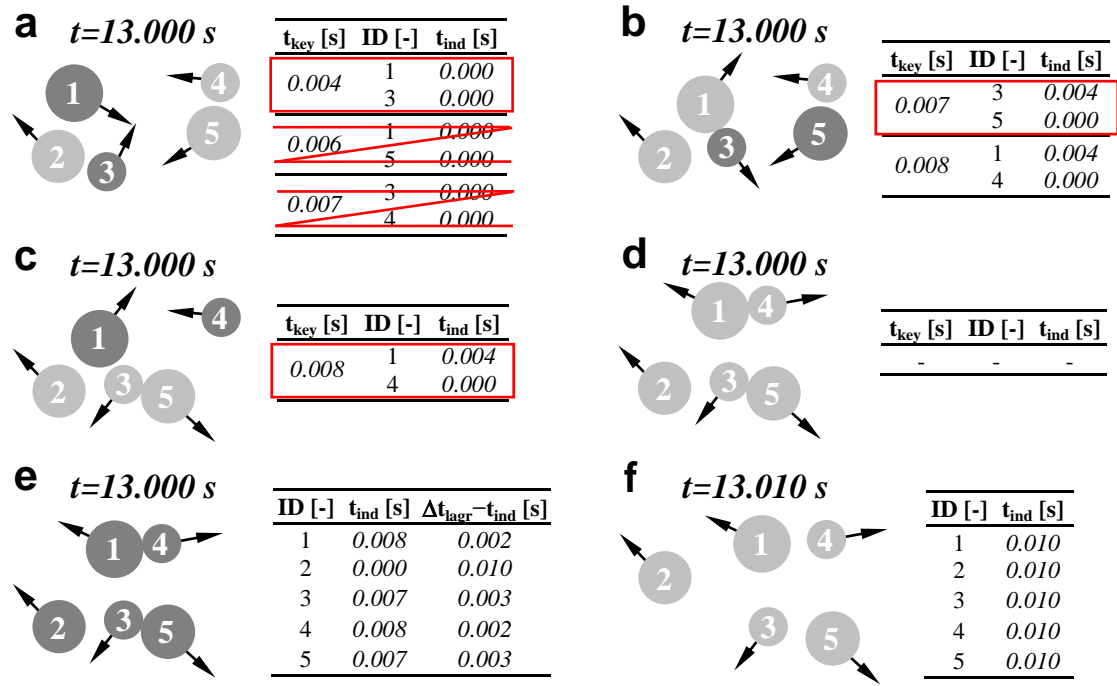


Figure 4.3: Schematic description of the speed-up technique. Exemplarily five particles with arrow indicated velocities are moved for $\Delta t_{\text{lagr}}=0.010\text{ s}$, starting at a simulation time $t=13.000\text{ s}$. At the beginning of the Lagrangian tracking (a) the collision times t_{coll} are calculated for all particles in the system. The collision pairs which fulfill the condition $t_{\text{key}} < \Delta t_{\text{lagr}}$ are chronologically registered in a collision table. Thereafter, the first collision pair (1 and 3) of the collision table is moved and the collision is performed. Then, all collision pairs including one of the two moved particles are removed from the table. Afterwards, t_{coll} are calculated for the two particles and the collision pairs which fulfill $t_{\text{key}} < \Delta t_{\text{lagr}}$ are chronologically added to the table. This procedure is repeated (b-c), till the collision table is cleared (d). Finally, all particles are moved for $\Delta t_{\text{lagr}} - t_{\text{ind}}$ (e), till their individual times t_{ind} match the increased simulation time $t + \Delta t_{\text{lagr}}$ (f).

its collision information is preserved in a collision table, whereby the entries are chronologically ranked by their t_{key} values. After the collision table is build, the two particles, forming the actual collision pair (the pair with the smallest t_{key}), are moved forward to the collision points \mathbf{x}_j^* :

$$\mathbf{x}_j^* = \mathbf{x}_j + \mathbf{u}_j \max[t_{\text{coll}}, t_{\text{ind},2} - t_{\text{ind},1} + t_{\text{coll}}], \quad (4.20)$$

whereupon the collision is performed by calculating the new velocities of the two particles.

Further, the individual times $t_{\text{ind},1}$ and $t_{\text{ind},2}$ of the two particles have to be updated. Then, all entries in the collision table, which involve one particle of the actual collision pair, have to be removed. In the next step, t_{coll} is only calculated for the two particles with potential collision partners registered in the ID-list. Thereby, collision pairs which fulfill $t_{\text{key}} < \Delta t_{\text{lagr}}$ are added

chronologically to the collision table. Again, the collision pair with the lowest t_{key} is moved accordingly to Eq. (4.20). This sequence is repeated till no collision pairs are left in the collision table within Δt_{lagr} . Hereupon, to finish the Lagrangian tracking, all particles in the system are moved for:

$$\mathbf{x}_I^* = \mathbf{x}_I + \mathbf{u}_I(\Delta t_{lagr} - t_{ind,1}). \quad (4.21)$$

The techniques described above can also be used for particle-wall collisions whereby, the value of $t_{ind,2}$ in Eqs. (4.19) and (4.20) remains zero.

4.2.5 The Experiments of Gan

The simulations in this study are compared to the experimental investigations of three-phase flow by Gan (2013). For his measurements, Gan used a laboratory-scale cylindrical BC of 0.152 m in diameter that was filled with a salt water mixture ($\rho_L=1049\text{ kg}\cdot\text{m}^{-3}$ and $\mu_L=9.85\cdot 10^{-4}\text{ Pa}\cdot\text{s}$ at 20°C) up to a height of 1.050 m , as shown in Fig. 4.4(a). A sparger with a diameter of 0.030 m and a height of 0.050 m was placed in the center of the column's bottom. A continuous air stream, injected with a flow rate of $0.8\text{ dm}^3\cdot\text{min}^{-1}$, was segmented by the sparger into discrete bubbles with diameters between 0.7 mm and 2.3 mm . Phase Doppler anemometry (PDA) measurement at various heights of the BC showed insignificant changes of the bubble size distributions (BSD), wherefore the in Fig. 4.4(c) shown invariant BSD is used for all simulations. For the solid phase, Gan used $20,000$ monosized acrylic beads ($\rho_L=1050\text{ kg}\cdot\text{m}^{-3}$) of 3.0 mm in diameter, giving a total solid hold-up of $\alpha_S=1.6\text{ vol}\%$.

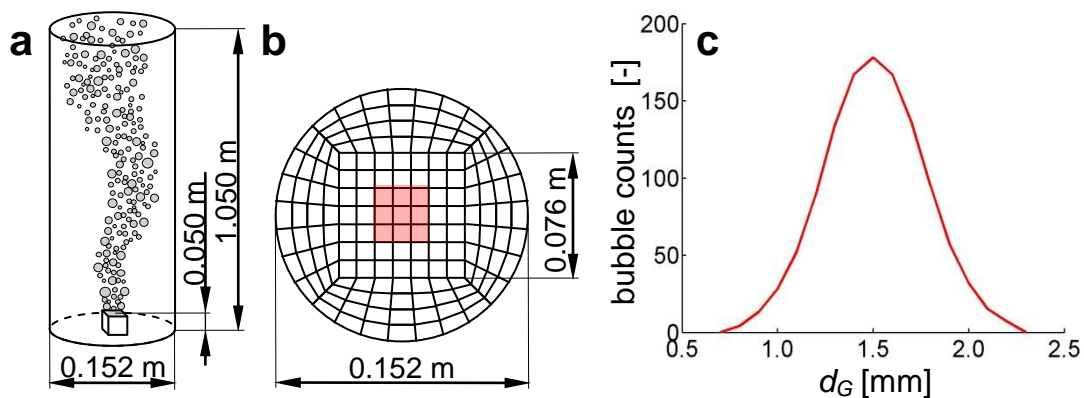


Figure 4.4: Schematic view of (a) the dimensions of the cylindrical bubble column, (b) the cross sectional profile of the grid whereby the red square marks the sparger, and (c) the bubble size distribution above the sparger.

4.2.6 Numerical Implementation

The geometry of Gan's experiments case is discretized using an appropriate computational grid, the center part of the BC has cuboid form that is composed of $7 \times 7 \times 105$ cubic cells with a typical edge length of 0.010 m , as shown in Fig. 4.4(b). In order to represent the sparger, the inner $3 \times 3 \times 5$ cells at the bottom of the above mentioned cuboid are left blank (they were not considered to be part of the computational domain). Air bubbles, following the size distribution in Fig. 4.4(c), are injected right above the sparger with a velocity of $0.290 \text{ m} \cdot \text{s}^{-1}$. The bubbles then ascend through the computational domain till they reach the top face (outlet), whereupon they are removed. For the three-phase simulations, $20,000$ solid particles are randomly distributed within the domain. If the solid particles reach the top face, they bounce back as described in Eq. (4.17) with $e=0.1$. For the integration of the liquid motion governing equations, second-order accurate numerical schemes are used in space (for the convection and diffusion terms) and time to avoid excessive numerical diffusion. The no-slip condition is applied at all bounding walls, while a free-slip condition is used for the top face. All simulations start with a stagnant liquid and proceed with a fluid time step of $\Delta t=1 \text{ ms}$ for 180 s , while the dispersed phases are tracked with a sub-time step of $\Delta t_{lagr}=1/3 \text{ ms}$.

4.3 Results and Discussion

The key parameters of the different simulation cases are summarized in Tab. 4.2. During the three-phase simulations, approximately 42,000 particles were moved during each time step, requiring an average simulation time of 8 days on a single-core desktop system.

Table 4.2: Summary of the simulated cases. The particle induced viscosities are given through Eqs. (4.7) and (4.8). In this study, case 1 (gas-liquid flow, GLF) serves as reference.

Case	Solid phase	Langevin model	Solid particle and bubble induced viscosities	Interaction model for dispersed phases
1	–	yes	yes	– (GLF)
2	yes	yes	–	no interaction model (NIM)
3	yes	yes	yes	no interaction model (NIM)
4	yes	yes	yes	drag force modification model (DFMM)
5	yes	yes	yes	elastic collision model (ECM)
6	yes	yes	yes	multistage collision model (MCM)

4.3.1 Algorithm Verification and Validation

Verification of the Terminal Rise Velocity of a Single Bubble

The terminal rise velocity u_{TERM} of a single gas bubble offers a good possibility to verify the coupling between the gas and the liquid phase. In order to obtain an analytical solution, the drag force coefficient $C_D=2/3(Eö)^{1/2}$ was used, where $Eö$ denotes the Eötvös number. The terminal rise velocity resulting from this drag model is $u_{TERM}=(4\sigma g(\rho_L-\rho_G)/\rho_L)^{1/4}$ (Darmana, 2006). Fig. 4.5 illustrates u_{TERM} for a single bubble of 5 mm in diameter that ascended in stagnant water with a temperature of 20 °C. As can be seen in the figure, the analytically and the numerically obtained graphs match very well.

Validation of the Trajectories of Two Colliding Solid Particles

The interactions between the solid particles, as well as the coupling between the solid and the liquid phase are validated via the experiment of Zhang et al. (1999). In their experiments, Zhang et al. recorded the trajectories of two glass beads ($d_S=2$ mm, $\rho_S=2000$ kg·m⁻³) in water

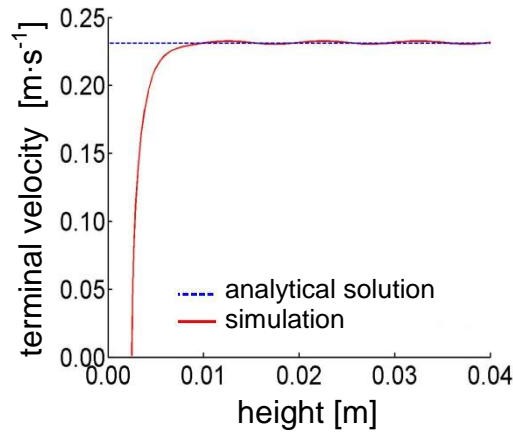


Figure 4.5: The terminal rise velocity of a single gas bubble as function of the column height ($d_B=5\text{ mm}$).

of $20\text{ }^\circ\text{C}$. Thereby, one of the particles accelerated in the gravity field over a height of 6 mm , before it hit the other particle, resting at the bottom of a vessel. For the simulation, the Stokes drag coefficient $C_D=24/Re_P(1+0.15Re_P^{0.687})$ was used. As shown in Fig. 4.6, the predicted trajectories showed good agreements with the experimentally obtained ones.

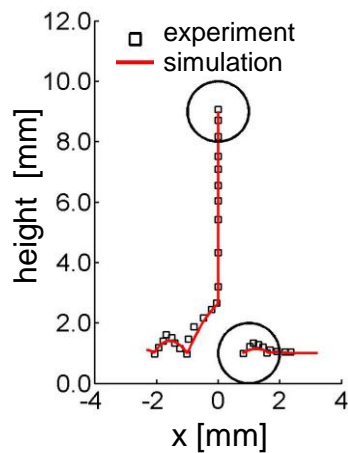


Figure 4.6: Trajectories of two colliding glass beads in a small vessel filled with water.

4.3.2 Three-Phase Flow

A series of snapshots in Fig. 4.7 illustrates the temporal evolution of the bubble plume and of the suspended particles for case 2. Since similar effects were observed in all gas-liquid-solid simulations, case 2 was chosen as representative for a qualitative discussion of the observed

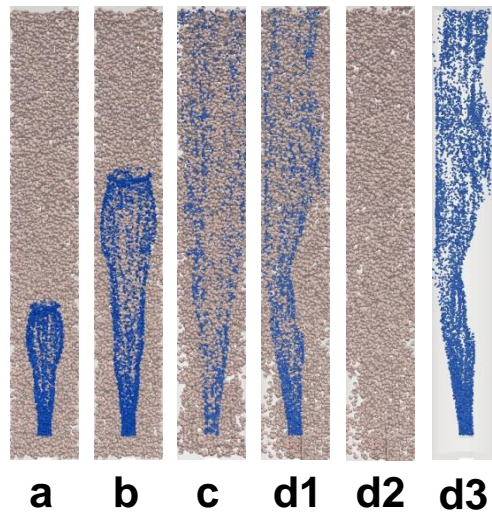


Figure 4.7: Snapshots of the evolving bubble plume (blue, d3), the solid particles (brown, d2) after (a) 1 s, (b) 2 s, (c) 20 s and (d) 100 s for case 2 (NIM). For illustration purposes, only the rear half of the column is displayed and all particles are magnified by a factor of three.

effects. In the beginning of the simulation, the solid particles were randomly distributed within the whole bubble column (BC). Along with the injection of the bubbles, a liquid flow was induced into the BC that started to carry the solid particles too. Fig. 4.8 demonstrates the trajectories of two randomly chosen solid particles. As can be seen in the figure, the particles were transported through the entire BC during the simulation. The induced liquid flow also led to an accumulation or depletion of the particles in particular regions of the bubble column. For instance, regions in the lowest column quarter (around the sparger) can be identified in Fig. 4.7(c) which contain no solid particles.

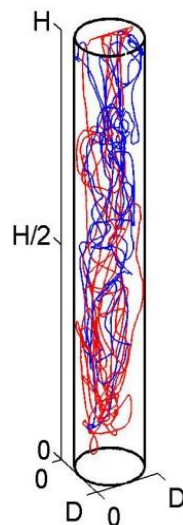


Figure 4.8: Trajectories (red and blue lines) of two solid particles during a typical simulation (case 2, NIM).

Local Hold-up Distribution

The instantaneous distribution of the solid particles in the mid-depth plane of the BC is illustrated in Fig. 4.9. Additionally, the figure shows the time-averaged hold-up of the solid phase, whereby the averaging started after 10 s and ended simultaneously with the simulations after 180 s . As can be seen from Fig. 4.9, high solid hold-ups were predicted for regions near the column bottom and near the column walls. Moreover, the figure also indicates a depletion of solid particles at the lowest column quarter and an accumulation in the topmost quarter. A similar vertical distribution of the solid hold-up was also obtained by [Ahmadi and Zhang \(2012\)](#) in their simulations with neutrally buoyant solid particles.

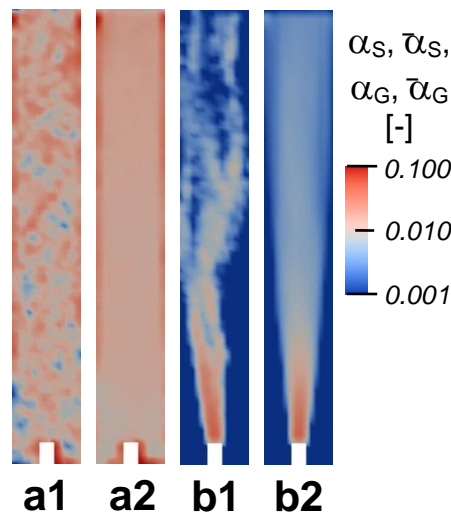


Figure 4.9: The (1) instantaneous hold-ups after 100 s and the (2) time-averaged hold-ups after 180 s in the mid-depth plane for (a) solid phase and (b) gas phase of case 2 (NIM).

The gas phase motion, illustrated in Figs. 4.7 and 4.9, showed characteristics close to the ones obtained for gas-liquid two-phase flow (see e.g. [Gruber et al., 2013](#)): After a short transient, the bubble plume started to oscillate from one column side to the other. As expected, the time-averaged gas hold-up was symmetric, since fluctuations of the gas phase were cancelled out. Furthermore, with increasing column height the bubble plume spread laterally, which caused a decrease of the gas phase hold-up in the BC's center. Regardless of the applied interaction model for the dispersed phases, no bubbles were found at column heights below the sparger orifice.

A comparison of the cross-sectional hold-up profiles for the gas phase is shown in Fig. 4.10 in a BC height of 0.75 m . In this figure, simulation of gas-liquid two-phase flow (GLF, case 1) serves as a reference. Compared to all gas hold-up profiles in this figure, the reference case

had the smallest gas hold-up. The gas-liquid-solid simulation without application of solid particle-bubble interactions (NIM, case 2) predicted a slightly higher hold-up for this height. However, the consideration of particle-induced viscosity (case 3) showed a significant increase of the gas hold-up. On the contrary, the solid hold-up profiles for both cases were very similar to each other, with high solid fractions near the column walls.

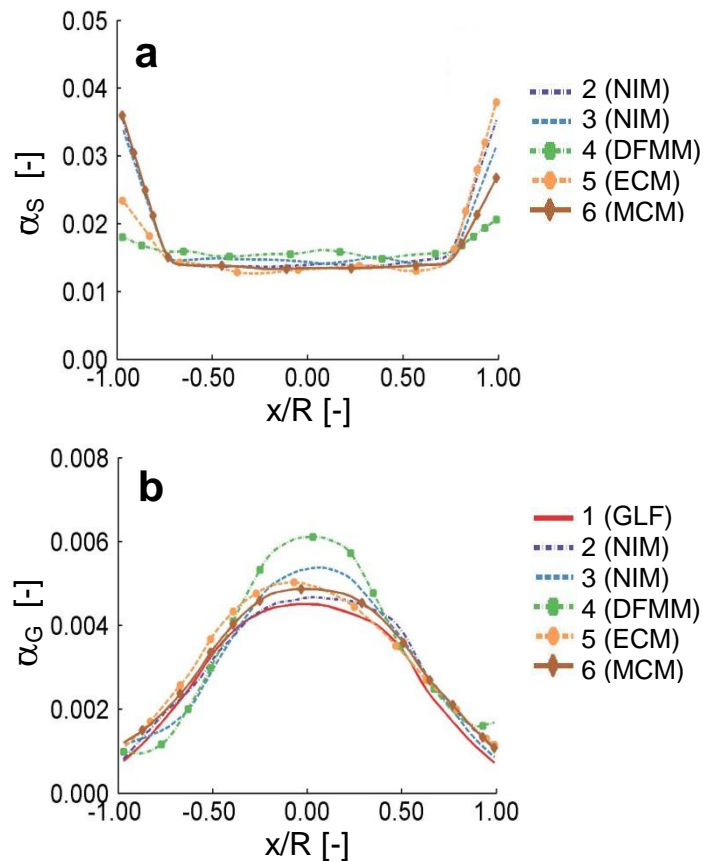


Figure 4.10: The time-averaged cross-sectional hold-up profiles after 180 s for (a) solid phase and (b) gas phase at a height of 0.75 m for various cases.

Of all performed simulations, the one in which the drag force modification model (DFMM, case 4) was incorporated predicted the highest gas hold-up for the height of 0.75 m. Additionally, the solid hold-up profile depicted the most uniform cross-sectional trend. In the study of Sommerfeld and Bourloutski (2002), the application of the DFMM caused an enhanced dragging of the solid particles through the bubbles, resulting in a more homogeneous distribution of the particles than compared to the simulation without interaction model. The profiles of the elastic collision model (ECM, case 5) and the multistage collision model (MCM, case 6) showed similar profiles for the gas hold-ups, as well as for the solid hold-ups, whereby in the latter the trend was laterally reversed. These similar predictions of

the hold-up profiles for cases 5 and 6 indicated that most of the collisions in case 6 were elastic collisions. Interestingly, except for the DFMM model, the cross-sectional hold-up profiles for the solid phase revealed contrary trends to the profiles of the gas phase: The bubbles were mainly located in the middle of the BC, while the solid particles were concentrated in the wall-near regions that showed high downward-speeds (see Fig. 4.12).

Velocity Distribution

Next, the velocities of the dispersed phases in the three phase system are qualitatively discussed. As with the previous chapter, case 2 is discussed as representative for all simulations, since similar qualitative effects were observed. Fig. 4.11 illustrates the vertical velocity component of each particle after 100 s. As can be seen in this figure, the velocities of the bubbles were significantly higher than the speed of suspended particles. Additionally, all bubbles and all solid particles, which were enclosed by the bubble plume, showed a positive vertical velocity, i.e. tendency to rise towards the top of the column. In contrary, most of the solid particles outside the bubble plume flowed downwards. These qualitative characteristics were also reported by [Ahmadi and Zhang \(2005\)](#). However, the observation described by Ahmadi and Zhang that solid particles accumulate in regions of high liquid velocities, was not confirmed in the simulations. Especially in the lowermost quarter of the BC where the maximum liquid velocities appeared, the solid phase was diluted, as can be easily seen by the comparison of Figs. 4.7 and 4.12.

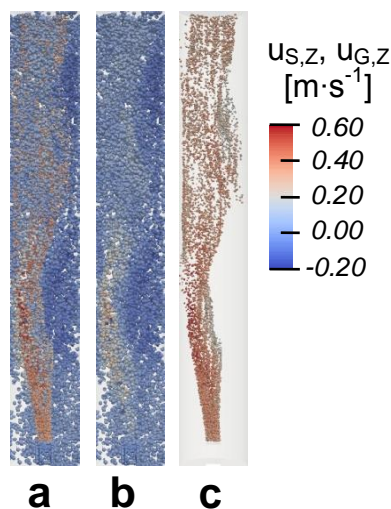


Figure 4.11: The instantaneous vertical velocity components of (a) all particles, (b) the solid particles and (c) the bubbles after 100 s for case 2 (NIM). For illustration purposes, only the rear half of the column is displayed and all particles are magnified by a factor of three.

The time-averaged vertical velocity profiles for the mid-depth plane of the BC, shown in Fig. 4.12, are considered next. Again, the averaging process started after 10 s and ended after 180 s . As discussed above, the velocity of the gas bubbles was significantly higher than the velocities of the two other phases. Near the walls, a vertical down-flow of liquid and solid particles developed, as it should be due to continuity reasons. Interestingly, the liquid phase velocity in the lowest third of the BC was higher than the velocity of the solid particles, which means that the particles in this region were indirectly agitated by the bubbles. Furthermore, the particles were dragged by the fluid, and bubble-particle interactions did not contribute significantly to momentum transfer to the particles. Note that no solid particle-bubble interaction model had been used in Fig. 4.12, so the latter fact was an obvious result of the simulation model. As described in the next paragraph, the incorporation of any of the above mentioned interaction models had no significant impact on the velocities of the solid particles in this region.

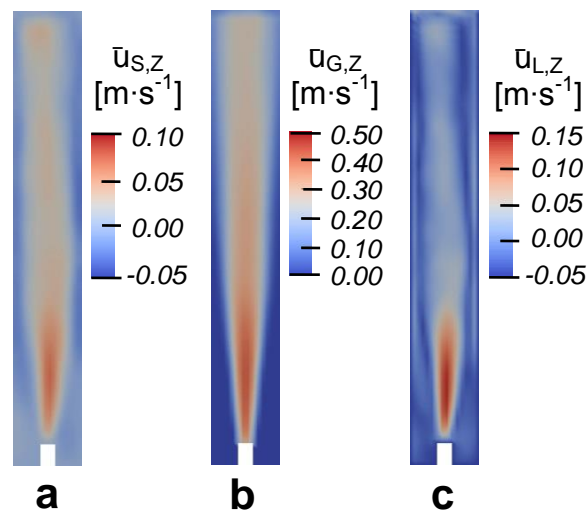


Figure 4.12: The time-averaged vertical velocity components for (a) the solid phase, (b) the gas phase and (c) the liquid phase after 180 s in the mid-depth plane of the BC (case 2, NIM).

Next, velocity profiles in two different heights of the BC are considered, in order to quantify the effect of different bubble-particle interaction models. The profiles were obtained through time-averaging of the vertical velocity components of the respective phase at heights of 0.15 m and 0.75 m , as shown in Fig. 4.13(a). Compared to the experimental measurements of Gan (2013), the vertical velocities of the solid particles at the BC's center were clearly underpredicted by all simulations. Consequently, the down-flow velocities of the particles near the column wall were also not accurately predicted. The numerically obtained velocity

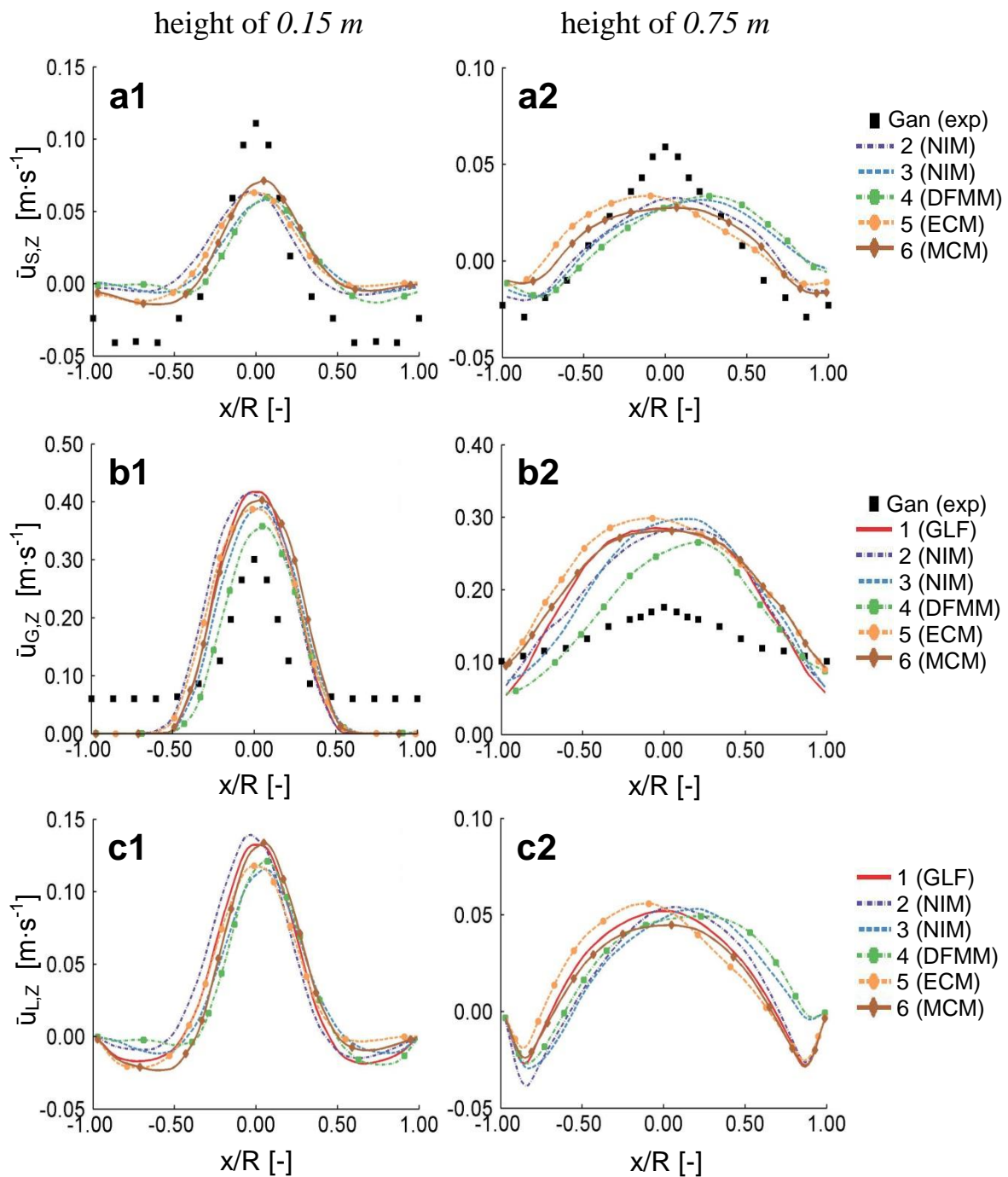


Figure 4.13: The time-averaged cross-sectional profiles of the vertical velocity component of (a) the solid phase, (b) the gas phase and (c) the liquid phase after at heights of (1) 0.15 m and (2) 0.75 m for various cases.

profiles looked very similar for all considered models. The most significant deviations occurred at the height of 0.75 m and for cases 3 and 4.

The time-averaged velocities of the bubbles are shown in Fig. 4.13(b). For both heights, the simulations significantly overpredicted the experimentally determined velocities for the center of the column. For the height of 0.15 m , nearly all simulations showed the same velocity profiles as the two-phase reference case (case 1). The only exception was the case with the DFMM incorporated (case 4), which yielded the predictions closest to the experimental results. However, still significant underpredictions of the bubble velocities near the walls were observed. The reason for this was that in all simulations no bubbles entered the region near the wall. This in turn suggests that the bubble plume in Gan's experiments quickly dispersed in the horizontal direction. Moreover, this fact also explains the flatter profile at 0.75 m , Gan observed in his experiment. For the height of 0.75 m , case 4 again showed the lowest and flattest velocity profile. A comparison of the cases 2 and 3 reveals that the particle induced viscosities had only a minor impact on the bubble velocities. Furthermore, the near wall bubble velocities of the ECM (case 5) and the MCM (case 6) were the highest of all simulations.

Finally, the time-averaged vertical liquid velocities are shown in Fig. 4.13(c). A comparison of the gas-liquid reference case (case 1) with the other simulations revealed only small changes of the liquid velocities. Accordingly, no significant reduction of the liquid velocity due to the solid phase was noticed, which is in contrast to the findings of [Sommerfeld and Bourloutski \(2002\)](#). However, this can be explained by the low solids hold-up of $1.6\text{ vol-}\%$ in this work, compared to $10\text{ vol-}\%$ in the studies of Sommerfeld and Bourloutski.

4.4 Summary and Conclusions

In this study, three-phase gas-liquid-solid flows were modeled by using an event-driven three-dimensional Euler-Lagrange (EL) approach: While the liquid phase was described in the Eulerian way, the dispersed phases were treated as discrete particles. Thereby, the main focus was put on the interactions between the bubbles and the solid particles. While bubble-bubble and solid particle-particle interactions were always considered to be inelastic, various models were tested to model solid particle-bubble interactions.

Specifically, the impact of no interaction model (NIM), of a drag force modification model (DFMM, described in [Mitra-Majumdar et al., 1997](#)), of an elastic collision model (ECM) and of a multistage collision model (MCM, described in [Ralston et al., 1999](#)) on the internal flow properties of a three-phase bubble column (BC) were investigated. Furthermore, since up to 42,000 particles were handled during the simulations, algorithm-based speed-up techniques were presented in this study, in order to accelerate the Lagrangian tracking of the dispersed phases.

The setup of the simulations was based on the experiments of [Gan \(2013\)](#), who applied a labor-scale cylindrical BC of 0.152 m in diameter and of 1.050 m in height. A constant air stream of $0.8 \text{ dm}^3 \cdot \text{min}^{-1}$ was segmented by a sparger into bubbles with diameters between 0.7 mm and 2.3 mm. For the solid phase, Gan used 20,000 monosized acrylic beads of 3.0 mm in diameter which had the same density as the salt-water solution. The verification of the terminal bubble rise velocity showed very good agreements with the analytical solution and also the validation of the trajectories of two colliding solid particles displayed a good match with the experimentally observed particles' paths.

The simulation results revealed that the solid particles were indirectly agitated by the ascending bubbles and were transported through the entire BC. Furthermore, the simulations predicted that solid particles were extracted from the lowest quarter of the BC and accumulate in its upper region. A slightly higher solids hold-up was also predicted for the bottom region, and the region near the walls. In the simulations, the time-averaged velocities of the bubbles were significant higher than the ones of the two other phases. Moreover, the vertical liquid phase velocity in the lowest third of the BC was highest and experienced a local maximum in the vertical direction at some distance from the sparger. This was due to the fact that the

bubble concentration was highest in this region and the liquid was dragged by the ascending bubbles. The velocities of the two other phases were more evenly distributed over the entire column height and the maximum in the vertical direction was less pronounced.

In comparison to the two-phase gas-liquid (GLF) reference simulation (case 1), the three-phase gas-liquid-solid flow simulations yielded a higher local gas hold-up at a height of 0.75 m . When considering particle induced viscosity (case 3), only a minor impact on the bubble velocity distribution and on the solid hold-up distribution was observed. However, a significant impact on the predicted gas hold-up was noticeable at a height of 0.75 m . The simulation with the DFMM incorporated (case 4) revealed a more uniform cross-sectional solid hold-up profile and significantly lower bubble velocities, compared to all other cases. The ECM (case 5) and the MCM (case 6) exhibited very similar numerical predictions for the solid and gas velocities, as well as for the solid and gas hold-up distributions. This fact indicated that most collisions within the case with MCM were elastic collisions. Of all tested interaction models, the DFMM seemed to predict the velocities of the dispersed phases slightly better.

However, compared to experimental measurements of [Gan \(2013\)](#), the velocities at the BC's center were underpredicted for the solid particles and overpredicted for the bubbles in all simulations. This suggests that none of the implemented collisions models was able to accurately reflect the true physics in a three-phase BC. Since the effect of various collision models have been carefully screened, one can speculate that effects due to (i) the attachment of gas bubbles on the particle surface (note that the bubbles have a smaller diameter than the solid particles), and (ii) wake effects lead to additional momentum transfer between the gas and the solid phase. Unfortunately, these effects cannot be easily introduced into the event-driven simulation framework that was used in the current study. For example, modeling enduring solid particle-bubble contacts or even the formation of larger particle-bubble clusters is simply not possible with this event-driven approach. Thus, further work has to be undertaken, possibly even using a different simulation approach, to enhance the predictive capabilities of EL simulations to model gas-liquid-solid flows.

Notation

Latin Letters

A	cross-section area, (m^2)
C	model constant, (–)
d	diameter, (m)
e	coefficient of restitution, (–)
$E\ddot{o}$	Eötvös number, (–)
\mathbf{F}	force vector, (N)
\mathbf{g}	gravitational acceleration vector, ($\text{m}\cdot\text{s}^{-2}$)
\mathbf{I}	unity tensor, (–)
m	mass, (kg)
p	pressure, (Pa)
r	radius, (m)
Re	Reynolds number, (–)
\mathbf{S}	characteristic rate of strain tensor, (s^{-1})
St	Stokes number, (–)
t	time, (s)
\mathbf{u}	velocity, ($\text{m}\cdot\text{s}^{-1}$)
\mathbf{x}	position vector, (m)

Greek Letters

α	volume fraction, (–)
Δ	filter length, (m)
μ	viscosity, ($\text{Pa}\cdot\text{s}$)
ρ	density, ($\text{kg}\cdot\text{m}^{-3}$)
σ	surface tension, ($\text{N}\cdot\text{m}^{-1}$)
$\boldsymbol{\tau}$	stress tensor, ($\text{N}\cdot\text{m}^{-2}$)
v	volume, (m^3)
Φ	volume specific interphase force term vector, ($\text{N}\cdot\text{m}^{-3}$)

Subscripts and Superscripts

B	buoyancy
$coll$	collision
D	drag
eff	effective
G	gas phase, bubble
ind	individual
I	induced
key	key value for storage in the collision table
$lagr$	Lagrange
L	continuous phase, liquid, lift

<i>n</i>	normal
<i>nbl</i>	neighbor cell list
<i>P</i>	dispersed phase, solid particle or bubble
<i>S</i>	solid phase, solid particle, Smagorinsky
<i>t</i>	tangential
<i>term</i>	terminal
<i>T</i>	turbulent
<i>VM</i>	virtual mass
*	modified

References

- Ahmadi, G., Zhang, X., 2005. *Three-Phase Liquid-Gas-Solid Flows in a Bubble Column*. Proceedings of the ASME 2005, Houston, USA, 761–765.
- Anil, M., Agarwal, V.K., Alam, M.S., Wasewar, K.L., 2007. *CFD Modeling of Three-phase Bubble Column: I. Study of Flow Pattern*. Chem. Biochem. Eng. Q. 21(3), 197–205.
- Darcovich, K., 1995. *A hydrodynamic simulation of mineral flotation. I: The numerical model*. Powder technol. 83(3), 211–224.
- Darmana, D., 2006. *On the multiscale modeling of hydrodynamics, mass transfer and chemical reactions in bubble columns*. PhD Thesis, Universiteit Twente, Enschede, The Netherlands.
- Gan, Z.W., 2013. *Hold-up and velocity profiles of monosized spherical solids in a three-phase bubble column*. Chem. Eng. Sci. 94, 291–301.
- Gruber, M.C., Radl, S., Khinast, J.G., 2013. *Coalescence and Break-Up in Bubble Columns: Euler-Lagrange Simulations Using a Stochastic Approach*. Chem. Ing. Tech. 85(7), 1118–1130.
- Hoomans, B.P.B., Kuipers, J.A.M., Briels, W.J., van Swaaij, W.P.M., 1996. *Discrete particle simulation of bubble and slug formation in a two-dimensional gas-fluidised bed: A hard-sphere approach*. Chem. Eng. Sci. 51(1), 99–118.
- Hu, G.S., 2005. *Towards Large Eddy Simulation of Dispersed Gas-Liquid Two-Phase Turbulent Flows*. PhD Thesis, West Virginia University, Morgantown.
- Jia, X., Wen, J., Zhou, H., Feng, W., Yuan, Q., 2007. *Local hydrodynamics modeling of a gas-liquid-solid three-phase bubble column*. AIChE J. 53(9), 2221–2231.
- Jianping, W., Shonglin, X., 1998. *Local hydrodynamics in a gas-liquid-solid three-phase bubble column reactor*. Chem. Eng. J. 70(1), 81–84.
- Karimi, M., 2014. *CFD Analysis of Solid-Liquid-Gas Interactions in Flotation Vessels*. PhD Thesis, Stellenbosch University, Matieland, South Africa.
- Kantarci, N., Borak, F., Ulgen, K.O., 2005. *Bubble column reactors*. Process Biochem. 40(7), 2263–2283.
- Koh, P.T.L., Schwarz, M.P., 2007. *CFD model of a self-aerating flotation cell*. Int. J. Miner. Process. 85(1), 16–24.
- Koh, P.T.L., Schwarz, M.P., 2008. *Modelling attachment rates of multi-sized bubbles with particles in a flotation cell*. Miner. Eng. 21(12), 989–993.
- Lahiri, S.K., Ghanta, K.C., 2010. *Slurry Flow Modelling by CFD*. Chem. Ind. Chem. Eng. Q 16(4), 295–308.

- Michele, V., Hempel, D.C., 2002. *Liquid flow and phase hold-up-measurement and CFD modeling for two-and three-phase bubble columns*. Chem. Eng. Sci. 57(11), 1899–1908.
- Mitra-Majumdar, D., Farouk, B., Shah, Y.T., 1997. *Hydrodynamic modeling of three-phase flows through a vertical column*. Chem. Eng. Sci. 52(24), 4485–4497.
- Padial, N.T., VanderHeyden, W.B., Rauenzahn, R.M., Yarbrow, S.L., 2000. *Three-dimensional simulation of a three-phase draft-tube bubble column*. Chem. Eng. Sci. 55(16), 3261–3273.
- Pozorski, J., Minier, J.P., 1998. *On the Lagrangian turbulent dispersion models based on the Langevin equation*. Int. J. Multiphase Flow 24(6), 913–945.
- Rabha, S., Schubert, M., Hampel, U., 2013. *Hydrodynamic Studies in Slurry Bubble Columns: Experimental and Numerical Study*. Chem. Ing. Tech. 85(7), 1092–1098.
- Rados, N., Al-Dahhan, M.H., Dudukovic, M.P., 2005. *Dynamic Modeling of Slurry Bubble Column Reactors*. Ind. Eng. Chem. Res. 44(16), 6086–6094.
- Ralston, J., Dukhin, S.S., Mishchuk, N.A., 1999. *Inertial hydrodynamic particle-bubble interaction in flotation*. Int. J. Miner. Process. 56(1-4), 207–256.
- Rampure, M.R., Buwa, V.V., Ranade, V.V., 2003. *Modelling of Gas-Liquid/Gas-Liquid-Solid Flows in Bubble Columns: Experiments and CFD Simulations*. Can. J. Chem. Eng. 81(3-4), 692–706.
- Sato, Y., Sekoguchi, K., 1975. *Liquid velocity distribution in two-phase bubble flow*. Int. J. Multiphas. Flow 2(1), 79–95.
- Silva, J.L, Mori, E.D., Soccol, R., d'Avila, M.A., Mori, M., 2013. *Interphase Momentum Study in a Slurry Bubble Column*. Chem. Eng. Trans. 32, 1507–1512.
- Smagorinsky, J., 1963. *General Circulation Experiments with the Primitive Equations*. Mon. Wea. Rev. 91(3), 99–164.
- Sommerfeld, M., Kohnen, G., Rüger, M., 1993. *Some open questions and inconsistencies of Lagrangian particle dispersion models*. 9th symposium on turbulent shear flows, Kyoto, Japan, 15–1.
- Sommerfeld, M., 2001. *Validation of a Stochastic Lagrangian Modelling Approach for Inter-Particle Collisions in Homogeneous Isotropic Turbulence*. Int. J. Multiphase Flow 27(10), 1829–1858.
- Sommerfeld, M., Bourloutski, E., 2002. *Transient RANS/Lagrange calculations of two- and three-phase flows in bubble columns*. Rodi, W., Fuero, N., (Eds.), Engineering Turbulence Modelling and Measurements 5, Elsevier Science, 969–978.
- Sommerfeld, M., Bourloutski, E., Bröder, D., 2003. *Euler/Lagrange Calculations of Bubbly Flows with Consideration of Bubble Coalescence*. Can. J. Chem. Eng. 81(3), 508–518.
- Ström, H., Bondelind, M., Sasic, S., 2013. *A novel hybrid scheme for making feasible numerical investigations of industrial three-phase flows with aggregation*. Ind. Eng. Chem. Res. 52(29), 10022–10027.
- Wang, T., Wang, J., Jin, Y., 2007. *Slurry Reactors for Gas-to-Liquid Processes: A Review*. Ind. Eng. Chem. Res. 46(18), 5824–5847.

Wang, L.K., Shamma, N.K., Selke, W.A., Aulenbach, D.B., (Eds.), 2010. *Flotation Technology*. Humana Press, New York, USA.

Wasewar, K.L., Anil, M., Agarwal, V.K., 2008. *CFD Modeling of Three-phase Bubble Column: 2. Effect of Design Parameters*. Chem. Biochem. Eng. Q. 22(2), 143–150.

Zeilstra, C., 2007. *Granular Dynamics in Vibrated Beds*. PhD Thesis, University of Twente, Enschede.

Zhang, J., Fan, L.S., Zhu, C., Pfeffer, R., Qi, D., 1999. *Dynamic behavior of collision of elastic spheres in viscous fluids*. Powder Techn. 106, 98–109.

Zhang, X., Ahmadi, G., 2005. *Eulerian-Lagrangian simulations of liquid-gas-solid flows in three-phase slurry reactors*. Chem. Eng. Sci. 60(18), 5089–5104.

Zhang, X., Ahmadi, G., 2011. *Particle Effects on Gas-Liquid-Solid Flows*. Proceedings of the ASME 2011, Denver, USA, 601–608.

Zhang, X., Ahmadi, G., 2012. *Numerical Simulations of Liquid-Gas-Solid Three-Phase Flows in Microgravity*. The Journal of Computational Multiphase Flows 4(1), 41–64.

Zhang, X., Ahmadi, G., 2013. *Effects of Neutrally Buoyant Particles on Gas-Liquid-Solid Flows*. Proceedings of the ASME 2013, Incline Village, USA, 1–7.

CHAPTER

5

*“Learn from yesterday, live for today, hope for tomorrow.
The important thing is to not stop questioning.”*
– Albert Einstein (1879-1955)

Conclusions and Outlook

5.1 Summary and Conclusions

In this study, a computational fluid dynamics (CFD) algorithm was developed for the numerical modeling of three-dimensional (slurry) bubble columns reactors (BCs), which are operated at the homogeneous or heterogeneous flow regime. Thereby, the algorithm was based on the open-source software package OpenFOAM® and pursued a four-way coupled event-driven Euler-Lagrange (EL) approach. By means of the algorithm, the influence of bubble break-up and coalescence (B&C) on two-phase gas-liquid flows was investigated in the chapters 2 and 3. In chapter 4, the algorithm was used to examine the influence of various interaction models for the dispersed phases on the flow properties of a three-phase gas-liquid-solid flow.

The algorithm was conscientiously validated and verified, wherefore the following cases were used as setup:

- Validations of two-phase gas-liquid flow revealed very good agreements for the liquid hydrodynamics (see Figs. 2.8 and 3.9; see also [Deen et al., 2001](#)) and the gas hold-up

(see chapter 2.3.3; see also [Bai, 2010](#)). Further, the validation of the through B&C received bubble size distributions (BSDs) showed good agreements, even though no large bubbles appeared in the forecasted BSDs (see Figs. 2.2, 2.5 and 3.10; see also [Hansen, 2009](#)).

- Moreover, a validation of the dispersed phases' velocities in three-phase gas-liquid-solid flow displayed that the velocities for the BC's center were underpredicted for the solid particles and overpredicted for the bubbles (see Fig. 4.13; see also [Gan, 2013](#)). Finally, the validation of the numerically obtained trajectories of two colliding solid particles showed good agreements (see Fig. 4.6; see also [Zhang et al., 1999](#)).
- Also, verifications of the incorporated models, with the analytically derived solutions, showed excellent agreements for the liquid component mixing (see Fig. 3.6; see also [Darmana, 2006](#)), the gas-liquid interphase mass transfer (see Fig. 3.7; see also [Darmana, 2006](#)), the shrinkage of a single bubble due to gas-liquid interphase mass transfer (see Fig. 3.8; see also [Zhang et al., 2009](#)) and the terminal rise velocity of a single bubble (see Fig. 4.5; see also [Darmana, 2006](#)).

The following conclusions were derived in this study:

- In chapter 2, the main benefit of B&C models resulted from the better prediction of the local interfacial areas, especially in the lower half of the BC (see chapters 2.3.2 and 2.3.3). As the Figs. 2.6 and 2.7 revealed, coalescence occurred mainly in regions directly above the sparger, leading to a rapid increase of the bubble sizes, while bubble break-up took place over the entire column height. This behavior consequently resulted in a maximum value of the Sauter mean diameter that was followed by a subsequent drop of the diameter over the remaining column height.
- Further, the Sauter mean diameters of the mono- and polydisperse BSDs differed by less than ten percent. Since similar forecasts of the overall gas hold-up (see Fig. 2.7) and the liquid hydrodynamics (see Fig. 2.8) were obtained with both shapes of distribution, it was concluded that the use of the Sauter mean diameter (if known *a priori*) would be sufficient for correct predictions of the flow properties.
- In chapter 3, the results for CO_2 chemisorption in $NaOH$ solutions showed a critical impact of bubble B&C on the mass transfer (see Fig. 3.11), the liquid phase mixing as well as the reaction rates (see Figs. 3.15 and 3.16) for systems with low to moderately large pH.

- At high pH values, bubble shrinkage became the dominating phenomenon, as illustrated in Fig. 3.21. Since bubble shrinkage led to small bubbles, low gas hold-up and little liquid phase agitation were observed in the upper part of the reactor (see Fig. 3.22). Consequently, with increasing pH the relevance of B&C decreased gradually, as shown in Fig. 3.21.
- In chapter 4, the simulation results for three-phase flow revealed that the solid particles were indirectly agitated by ascending bubbles. During the simulations, the particles were transported through the entire BC, as illustrated in Fig. 4.8.
- Furthermore, the simulations predicted an extraction of the solid particles from the lowest quarter of the BC and as a result, an accumulation in the upper region. A higher solid hold-up was also predicted for the bottom region and the region near the walls, as depicted in the Figs. 4.7 and 4.9.
- Finally, the effect of the particles on the suspension's viscosity had a significant impact on the local gas hold-up distribution: While the drag force modification model led to uniform solid hold-ups and lower bubble velocities, the elastic collision model and the multistage collision model showed similar flow predictions. This fact indicated that most collisions within the case with multistage collision model were elastic collisions.

5.2 Outlook

It can be expected that with in parallel with the progress in the computer technology, the EL approach will gain in importance for the modeling of multiphase flow. For the modeling of industrial full-scale (slurry) BCs, which contain up to billions of bubbles and even more solid particles in the suspension, several issues have to be solved in future works, in particular for the homebrewed algorithm presented in this study:

- None of the used kernel functions (Coulaloglou and Tavlarides, 1977; Lee et al., 1987a, 1987b) in this study for bubble B&C could reproduce the experimentally obtained BSD from Hansen (2009), wherefore more sophisticated kernel functions should be verified. Collections of B&C kernels can be found in e.g. Lasheras et al. (2002), Liao and Lucas (2009, 2010) and Martinez-Bazan et al. (2010). Additionally, future studies have to evaluate the influence of various sub-models (e.g. drag, lift, energy-dissipation rate) on the B&C models and hence on the BSD.
- Due to the injection and removal of the dispersed particles during the simulation from the computational domain, numerical instabilities appear during the solution step of the hydrodynamic equations for the liquid, causing strong pressure fluctuations. These instabilities can be avoided through pressure cells (Darmana, 2006) or through the introduction of a mean liquid volume fraction in Eq. (2.30). However, if the gas flow rate becomes too high, the instabilities arise again, wherefore an alternative approach has to be found, e.g. a new scheme for the injection and bursting of the bubbles.
- Industrial BCs are mainly operated in the heterogeneous flow regime, which is characterized by a dense bubble flow and hence reduced spacing between the bubbles. Since bubbles are treated as spheres with rigid surfaces in the EL approach, coalescences lead to overlaps of the bubbles. For dense flows, the bubble shifting technique presented in chapter 2.2.5 becomes computationally intensive. A future approach would require a more flexible treatment of the bubble shapes. Further models for dense bubble flow should also account for additional bubble interactions, e.g. effect of bubble wakes, where big bubbles drag small bubbles in their wake.
- The validation of the three-phase gas-liquid-solid flow predictions with the experimental results of Gan (2013) revealed also differences in the radial distribution

profile of the bubbles at low height above the sparger: While bubbles covered the entire cross-section during the experiments, no bubbles were predicted for wall-near regions during the simulations. Therefore, future experiments should apply a more suitable sparger type that leads to a more reproducible setup case for numerical studies.

- For the modeling of three-phase gas-liquid-solid flows, the time-driven (soft-sphere) approach seems to be better suited than the event-driven (hard-sphere) approach, since effects, e.g. the sliding of a solid particle around a bubble, the adhesion of a solid particle on the bubble surface or *vice versa*, are already incorporated in this approach and do not have to be modeled artificially (see e.g. [Crowe, 2006](#)).
- Due to contributions of users and an extended library, the open-source project OpenFOAM® has become a powerful tool for modeling of all kinds of multiphase flows. Future cooperation with the OpenFOAM foundation would help to ensure a sustainable and reliable development of economic CFD software.

References

- Bai, W., 2010. *Experimental and Numerical Investigation of Bubble Column Reactors*. PhD Thesis, Eindhoven University of Technology, Eindhoven.
- Coulaloglou, C.A., Tavlarides, L.L., 1977. *Description of interaction processes in agitated liquid-liquid dispersions*. Chem. Eng. Sci. 32(11), 1289–1297.
- Crowe, C.T., (Ed.), 2006. *Multiphase flow handbook*. CRC press, Boca Raton, Florida, USA.
- Darmana, D., 2006. *On the multiscale modeling of hydrodynamics, mass transfer and chemical reactions in bubble columns*. PhD Thesis, Universiteit Twente, Enschede, The Netherlands.
- Deen, N.G., Solberg, T., Hjertager, B.H., 2001. *Large eddy simulation of the Gas-Liquid flow in a square cross-sectioned bubble column*. Chem. Eng. Sci. 56(21), 6341–6349.
- Gan, Z.W., 2013. *Hold-up and velocity profiles of monosized spherical solids in a three-phase bubble column*. Chem. Eng. Sci. 94, 291–301.
- Hansen, R., 2009. *Computational and Experimental Study of Bubble Size in Bubble Columns*. PhD Thesis, Aalborg University, Esbjerg.
- Lasheras, J.C., Eastwood, C., Martinez-Bazan, C., Montanes, J.L., 2002. *A review of statistical models for the break-up of an immiscible fluid immersed into a fully developed turbulent flow*. Int. J. Multiphase Flow 28(2), 247–278.
- Lee, C.H., Erickson, L.E., Glasgow, L.A., 1987a. *Bubble breakup and coalescence in turbulent gas-liquid dispersions*. Chem. Eng. Commun. 59(1), 65–84.
- Lee, C.H., Erickson, L.E., Glasgow, L.A., 1987b. *Dynamics of bubble size distribution in turbulent gas-liquid dispersions*. Chem. Eng. Commun. 61(1), 181–195.
- Liao, Y., Lucas, D., 2009. *A literature review of theoretical models for drop and bubble breakup in turbulent dispersions*. Chem. Eng. Sci. 64(15), 3389–3406.
- Liao, Y., Lucas, D., 2010. *A literature review on mechanisms and models for the coalescence process of fluid particles*. Chem. Eng. Sci. 65(10), 2851–2864.
- Martinez-Bazan, C., Rodriguez-Rodriguez, J., Deane, G.B., Montanes, J.L., Lasheras, J.C., 2010. *Considerations on bubble fragmentation models*. J. Liquid Mech. 661, 159–177.
- Zhang, J., Fan, L.S., Zhu, C., Pfeffer, R., Qi, D., 1999. *Dynamic behavior of collision of elastic spheres in viscous fluids*. Powder Techn. 106, 98–109.
- Zhang, D., Deen, N.G., Kuipers, J.A.M., 2009. *Euler-Euler Modeling of Flow, Mass Transfer, and Chemical Reaction in a Bubble Column*. Ind. Eng. Chem. Res. 48(1), 47–57.

List of Publications

Articles in Refereed Journals

Gruber, M.C., Radl, S., Khinast, J.G., 2015. *Rigorous Modeling of CO₂ Absorption and Chemisorption: The Influence of Bubble Coalescence and Breakage*. Submitted to Chem. Eng. Sci.

Gruber, M.C., Radl, S., Khinast, J.G., 2015. *Effect of Bubble-Particle Interaction Models on Flow Predictions in Three-Phase Bubble Columns*. Submitted to Chem. Eng. Sci.

Gruber, M.C., Radl, S., Khinast, J.G., 2013. *Coalescence and Break-Up in Bubble Columns: Euler-Lagrange Simulations Using a Stochastic Approach*. Chem. Ing. Tech. 85, 1118–1130.

Proceedings and Conference Presentations

Gruber, M.C., Khinast, J.G., *Stochastic Break-up Model for Euler-Lagrangian Simulations*. 7th Minisymposium der Verfahrenstechnik, Graz, Austria, June 30th 2011.

Gruber, M.C., Khinast, J.G., *Stochastic Breakup Model for Euler-Lagrangian Simulations*. Jahrestreffen der Fachausschüsse Computational Fluid Dynamics und Mischvorgänge, Dortmund, Germany, February 21st 2011.

Gruber, M.C., Radl, S., Khinast, J.G., *Bubble column slurry reactors towards detailed LES of these gas-solid-liquid systems*. ProcessNet-Jahrestagung 2010 und 28th Jahrestagung der Biotechnologen, Aachen, Germany, October 21st 2010.

Gruber, M.C., Radl, S., Khinast, J.G., *Bubble column reactors-detailed LES of the gas-solid-liquid system*. 19th International Congress of Chemical and Process Engineering (CHISA), Prague, Czech Republic, August 29th 2010.

Gruber, M.C., Radl, S., Eitzlmayr, A., Suzzi, D., Khinast, J.G., *Comprehensive Modeling of Reactions in Multiphase Flows*. 6th Minisymposium der Verfahrenstechnik, Tulln, Austria, June 25th 2010.

Gruber, M.C., Eitzlmayr, A., Radl, S., Suzzi, D., Khinast, J.G., *Modeling Fast Reactions and Particle Flow-Applications of OpenFOAM in the Pharmaceutical Industry*. 5th OpenFOAM Workshop, Gothenburg, Sweden, June 21th 2010.

Gruber, M.C., Ziger, P., Eiselt, P., Jäger, H., *Gleichstrom-Niederdruckentladungen unter dem Einfluss von Magnetfeldern*. 56th Jahrestagung der österreichischen Physikalischen Gesellschaft, Graz, Austria, September 28th 2006.

About the Author

Michael Christian Gruber was born on March 18th 1977, in Schörfling, Austria. After graduating from the secondary technical school for chemical technology (HTL) in Wels in 1997, he began a course of study in technical physics at the University of Technology Graz. The author focused on subject experimental physics and drew up his master thesis about “The influence of magnetic fields on low-pressure gas-discharges”. In 2006, after a one-year interruption due to the fulfillment of the civilian service, he completed his studies and began to work for the pharmaceutical company Roche Diagnostics Graz GmbH. In the department of research and development, the author worked as technician in measurement technology on building a blood sample analyzer for blood gas and electrolytes. In 2009, he began to work as project assistant at the Institute of Process and Particle Engineering (IPPT) at the University of Technology Graz. At the same time, he started his doctoral thesis on “Hydrodynamics, mass transfer and chemical reactions in bubble columns”, supervised by Prof. Khinast. In 2011, the author continued as university assistant his employment on the institute for two further years.